A Lagrangian vortex method for vortex evolution

Moussa, Charbel

Award date:
2007

Awarding institution:
University of Bath

A LAGRANGIAN VORTEX METHOD FOR VORTEX EVOLUTION

Submitted by Charbel Moussa
for the degree of
Doctor of Philosophy
of the University of Bath
April 2007

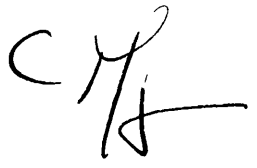

ProQuest LLC
789 East Eisenhower Parkway
P.O. Box 1346
Ann Arbor, MI 48106-1346

Ask, and it shall be given you; seek, and ye shall find; knock, and it shall be opened unto you. For every one that asketh receiveth; and he that seeketh findeth; and to him that knocketh it shall be opened.

(Matthew 7:7-8)

Abstract

In this thesis, a novel Lagrangian vortex method that circumvents the limitations of the classical schemes is introduced, validated and applied to the practical problem of computing the dynamics of a class of vortex instabilities. The method enjoys several advantages, especially its ability to reduce computational time and compute viscous effects. The technique meshes the control points that represent the vorticity field, and approximates the streamfunction and its derivatives by a second order truncated Taylor series at each nodal point. The equations are then solved directly at the nodes in a least-squares sense, using a standard linear solver for large sparse systems. Once the streamfunction and its derivatives are found, the node motion is computed using a low-storage Runge-Kutta scheme. The method computes viscous effects by fitting a polynomial function about each node, which is then solved in a least-squares sense. To maintain the quality of the mesh, the computational domain is remeshed every few time steps.

The implementation of the code is checked via the Method of Manufactured Solutions, and the numerical approach is validated for inviscid and viscous flows. In all cases, the computed results are in good agreement either with theoretical solutions or results of previous studies. These tests prove the robustness and reliability of the new method.

The evolution of perturbed Lamb-Oseen vortices is studied using the current scheme. It is found that the unshielded monopoles disturbed with various amplitudes at different Reynolds numbers either relax to axisymmetry or form high-order multipoles, such as tripoles, triangles and square vortices. The results show that for every Reynolds number there exists a critical amplitude that separates the attractors to which the perturbed Lamb-Oseen vortex decays, and when Reynolds number increases the threshold value decreases.

Once formed, the tripole is stable and decays to axisymmetry due to viscous effects, unlike the triangle which does not retain its shape and experiences vortex merging that turns it into a tripole. On the other hand, the square vortex is found to be very unstable and to evolve shortly after its formation into a tripole through vortex merging.

Prologue

A warrior of light knows that he has much to be grateful for.

He was helped in his struggle by the angels; celestial forces placed each thing in its place, thus allowing him to give of his best.

His companions say: 'He's so lucky!' And the warrior does sometimes achieve things far beyond his capabilities.

That is why, at sunset, he kneels and gives thanks for the Protective Cloak surrounding him.

His gratitude, however, is not limited to the spiritual world; he never forgets his friends, for their blood mingled with his on the battlefield.

A warrior does not need to be reminded of the help given him by others; he is the first to remember and he makes sure to share with them any rewards he receives.

Manual of the Warrior of Light, Paulo Coelho, 2002

Thanks

I would like to thank all who supported me throughout this journey and made its completion possible, especially:

- My Father who art in Heaven, for his infinite blessings and grace.
- My family, especially my mother Claudette, for everything; without them I would not be here today.
- Jeanine Aoun, for all her love, sacrifices, support, patience and understanding.
- Dr. Michael Carley, my supervisor, for providing the financial support and for his ideas, guidance, advice and encouragement at various crucial stages of this project.
- Fr. Bill McLoughlin, for all his support and help during my years in Bath, and all my friends in Cathsoc.
- Dr. James Whitehead, for our trip to Cuba, our whiskey and cigar evenings and his comments on this thesis.
- Prof GertJan van Heijst of Eindhoven University of Technology, for his interest in my work and his comments on Chapter 7 of the thesis.
- Dr. Lorena Barba of Bristol University, for her permission to use her results.
- Anna Tai, for the coffee breaks that were crucial to keep me going.
- Fadi Mitri, for our travels and discussions about life, religion, engineering and international affairs.
- Kamal Khoury, for the hours-long analyses of Lebanese politics.
- Dr. Andrew Rees, for his interest in my work, his challenging questions that kept me looking for answers and his interesting stories.
- Prof. Ismet Gursul, for his continuous support and encouragement.
- My officemates, Bernardo Garcia-Carreras, Dave Marles, Dr. Eleni Vardaki, Dr. Gordon Taylor, Nathan Williams, Nicholas Gresham, Dr Panagiota Pantazopoulou, Dr. Panagnotis Margaris, Paul Lewis, Ping Jiang, Pinunta Rojratsirikul, Dr. Sam Heathcote and Dr. Zhi-jin Wang, for all the fun, humour and pleasant company.
- The inter-library loan staff at the university of Bath, for dealing promptly with my requests.
- Everyone in the International Office, for their help and friendship.

Contents

List of Figures

List of Tables

Chapter 1

Introduction

Vortices are the sinews and muscles of fluid motion.

Dietrich Küchemann, 1965

'Vortex' is the term used to describe a spinning mass of fluid around its central axis. Vortices are fundamental motion in fluid dynamics that can be present in the smallest scale of turbulence or large scale natural phenomena. They take the form of hurricanes in oceans, tornadoes over land and wake behind aeroplanes. On a much smaller scale, a vortex is usually formed by spinning a spoon in a cup of tea, or by water going down a drain, as in a sink or a toilet.

Vortices have their own dynamics that greatly affect fluid motion. Their evolution can be subject to complex interactions, which may lead to their merging or breakdown. In an aeronautical context, the formation, evolution and disappearance of vortices can have a dramatic impact on the performance of aircraft and flight stability and control. For example, wing tip vortices decrease the lift and increase the induced drag, affecting fuel consumption. Moreover, these vortices pose severe hazards to aircraft flying close to other aircraft, especially at take off and landing, and can cause serious accidents. Vortex breakdown over the wings can lead to flow separation, which causes loss of lift and stall. Therefore, understanding vortex dynamics is a priority for aerodynamicists, and a prerequisite for any aeronautical design.

Extensive laboratory and numerical experiments have been conducted on the subject of vorticity. Nowadays scientists profit from the advance in numerical models and development of powerful computers to investigate and analyse all aspects of vortex dynamics, especially those not easy to study in the laboratory. These investigations are made possible thanks to the contributions of great scientists who have worked on the field of vortex dynamics for decades. The next section will be a journey over the early development of this field and the works of its fathers.

1.1 Origins of vortex dynamics

Vortex dynamics is a subfield of fluid mechanics. The study of fluid mechanics, which is the science and art of understanding fluid motion, can be traced back to Archimedes

(287–212BC), a Greek scientist who was attracted by fluid equilibrium and discovered the principle of buoyancy. He studied floating bodies and introduced some basic ideas in fluid statics [1]. The motion of water and air fascinated Leonardo da Vinci (1452–1519), an Italian polymath, who observed, studied and drew several sketches of running water and flying machines [2]. He drew analogies between rivers and blood vessels as he believed water to be the blood of the world, and investigated the nature of its behaviour in the body of the Earth. He was especially attracted by its turbulent and spiral motion, which he compared to the curls of hair. He noted that "the motion of the surface of water resembles the behaviour of hair, which has two motions, of which one depends on the weight of the strands, the other on the line of its revolving; thus water makes revolving eddies, one part of which depends upon the impetus of the principle [sic] current, and the other depends on the incident and reflected motions" [3]. This observation can be considered the first of vortex motion in fluid dynamics. Vorticity can be clearly seen in Figure 1.1, which shows Leonardo da Vinci's drawings of water passing obstacles and falling from an orifice.

Figure 1.1: Leonardo da Vinci's drawing showing vortical flows as water passes obstacles and falls from an orifice [2].

However, the first detailed mathematical analysis of fluid flows came more than two centuries after da Vinci's observations, when the Swiss scientist Leonhard Euler (1707–1783) derived a set of differential equations, now named after him, that relate the velocity, pressure and density of a moving fluid [4, p.3]. He represented the flow field as a continuous collection of infinitesimally small fluid elements with spatially varying three-dimensional pressure and velocity fields. Then, Euler applied conservation of mass and Newton's second law, force equals mass times acceleration, and was able to obtain two coupled, nonlinear partial differential equations, the Euler equations, which represent the conservation of mass, momentum and energy in a fluid.

The derivation of these equations was an intellectual breakthrough in theoretical fluid dynamics, as for the first time vortex motion could be studied. Solving the Euler equations for a given problem permits the investigation of the creation and evolution of vorticity. However, these equations are not a realistic representation of flow fields, as Euler neglected the effect of friction on the motion of the fluid elements. Therefore, viscous effects are not modelled.

It was another decade before the Euler equations were modified to take into account the effect of viscosity. The independent work of the French engineer Claude-Louis Navier (1785–1836) in 1822 and of the Irish mathematician George Gabriel Stokes (1819–1903) in 1845 resulted in a system of nonlinear partial differential equations that describe the motion of viscous flows. The Navier-Stokes equations are time dependent, and like the Euler equations, they conserve mass, momentum and energy. They model the changes in momentum in infinitesimal volumes of fluid as the sum of dissipative viscous forces, changes in pressure, gravity, and other internal forces in the fluid. Since their introduction, they directly became the governing equations in the mathematical description of fluid flows. As differential equations, they could, in principle, be solved for a given problem with the help of calculus. However, in practice, these equations are extremely difficult to solve, and to this day, no one has yet obtained a general analytical solution of them. The challenge posed by the Navier-Stokes equations motivated the Clay Mathematics Institute to offer in 2000 a prize of 1 million dollars to whoever makes "substantial progress toward a mathematical theory which will unlock the secrets hidden in the Navier-Stokes equations" [5]. No one has claimed it yet.

The solution of the Navier-Stokes equations is not the particle positions, but rather their pressures and velocities, which are subsequently used to compute the fluid motion. Only in simple cases of steady state, non-turbulent, highly viscous flows are exact solutions of these equations known. In the past, scientists resorted to approximations and simplifications in order to solve the equations. Nowadays, computer programs are used to solve them via various numerical techniques, such as finite difference and spectral methods. This area of study is called Computational Fluid Dynamics (CFD), and will be discussed in the next section.

Later on, the motion of vorticity in a perfect fluid, which is inviscid, was studied by the German physician and physicist Hermann von Helmholtz (1821–1894). He published his results in 1858 in a paper entitled "On integrals of the hydrodynamical equations which express vortex motion" [6]. He showed that vorticity moves with the flow, and stated his three laws of vortex motion, which will be explained in the next chapter §2.2. Helmholtz' theorems were soon followed by Lord Kelvin's work "On vortex motion" [7], in which he introduced the notion of circulation and proved that in an inviscid fluid circulation around a closed curve would be conserved. Helmholtz and Kelvin's concepts are the cornerstone of the study of vortical flows.

At the beginning of the 20th century when the Wright brothers invented the first practical aircraft, the study of aerodynamics became acute. Scientists needed to compute frictional shear forces of a real fluid on a body immersed in it in order to calculate the lift and drag on the machine. This motivated the German physicist Ludwig

Prandtl (1875–1953) to work on fluid mechanics even though he completed a Ph.D. in solid mechanics. This decision was behind many breakthroughs in aerodynamics. In 1904 Prandtl described for the first time the boundary layer in a groundbreaking paper, "Fluid flow in very little friction" [8]. He explained its importance for drag and its contribution to flow separation, introducing therefore the concept of stall. He invented lifting-line theory and thin-aerofoil theory, which led to the recognition of the importance of wing tip vortices on induced drag [9]. Prandtl was among the first to study turbulent flow, which he found chaotic and very complicated [10]. However, in 1984 McWilliams' observations revealed that turbulence is more structured than Prandtl thought, and leads to the formation of vortices [11]. This discovery raised hope that studying vortex dynamics might help understand turbulent flows, a still unresolved problem of classical physics.

Vortex dynamics continues today as a field of active research, helped by continuous development in the area of computational fluid dynamics.

1.2 Computational fluid dynamics

Rapid advances in computer speeds and progress in numerical methods have made the simulation of some engineering problems possible; as a result many mathematical models have been developed. Those describing flow fields are commonly known as Computational Fluid Dynamics (CFD) techniques, which compute the flow by solving different mathematical equations, coupled with equations of state or other energy equations.

Computational fluid dynamics enables scientists to investigate a wide range of problems such as vortex formation, heat and mass transfer, chemical reactions and fluid-structure interaction through computer modelling. This technique is becoming very popular due to its three main advantages: insight, foresight and efficiency. CFD enables the study of complex phenomena that are difficult to model experimentally, such as nuclear reactions. Moreover, it predicts the performance and outcome of a specific system, allowing flexibility in testing many variations to achieve an optimal result. This is done at reasonable cost since numerical studies are usually much cheaper to run than experimental investigations. These advantages optimise the design and development cycle of a product, and help cost reduction.

New CFD models are developed either by improving numerical methods or mesh generation techniques. Over the last century, efficient flow solvers and grid generation algorithms have been developed, and computer architecture and networking speeds have improved tremendously [12]. This has provided powerful tools for simulating vortical flows, a privilege not available to the great scientists who founded vortex dynamics. Nowadays, CFD models are widely used to complement experimental results, and investigate complex engineering problems that are difficult to study experimentally.

The area of numerical methods has experienced an intense research activity, driven by the aerospace industry for its requirements for accurate solutions with minimum

computational cost [13]. Potential flow problems were the first to be studied, but with improvements in solution strategies and computational resources, attention was drawn to more complicated systems. These advances made the simulation of flow fields described by Euler and Navier-Stokes equations possible. Numerical approaches are being continuously developed to increase the accuracy of computed solutions. Early methods were based upon finite difference or finite volume techniques. Later on, Lagrangian vortex methods were introduced to offer an alternative for high-resolution simulation of incompressible flows.

1.3 Aims of the current work

Lagrangian vortex methods are a group of various schemes that share the same fundamental principles. They discretise the flow into vorticity fields, then calculate the induced local velocities to convect the vorticity. They are very popular and attractive to scientists due to their simplicity. Their advantages lie especially in the use of computational elements only for non-zero vorticity regions. However, they require a large number of points, which implies a high computational cost. Moreover, classical Lagrangian vortex methods are unable to accurately compute viscous flows unless special treatments are applied. These difficulties have motivated the continuous development of new Lagrangian approaches in order to bypass them. The field is still maturing, and an agreement between scientists on the best method to use has not been reached yet. Every scheme has its desirable characteristics and advantages.

Classical vortex methods usually represent the vorticity by point vortices, blobs or vortex filaments, which require a large number of elements and special distributions to give a smooth variation of vorticity. On the other hand, the computation of the induced velocity is achieved by evaluating a Biot-Savart integral on a point-to-point interaction basis, leading to $O(N^2)$ computational effort, where N is the number of points in the domain.

The aims of the current work are to introduce, validate and assess a novel Lagrangian vortex method that circumvents the limitations of the classical schemes. The technique, based on Delaunay triangulation, represents the computational field by a set of points connected by a triangular mesh, and approximates the vorticity on each node. This approach, which was introduced in the 1990s, has been applied in a variety of problems and proved to be robust [14–17]. To calculate the local induced velocities, instead of using the integral approach, a technique that does not seem to have been used yet in Lagrangian schemes is applied: the partial differential equation for streamfunction is directly solved on the node.

Several tests are performed to check the implementation of the code and validity of the method. Then the computational scheme is used to study the dynamics of a class of vortex instabilities.

1.4 Road map of the thesis

In chapter 2 some fundamental principles of fluid dynamics that will be used later on in the thesis are introduced. Chapter 3 is a brief review of vortex methods. The different forms of vorticity discretisation are presented with a discussion of the advantages and limitations of each one. Then, the different Lagrangian schemes for viscous diffusion are introduced and explained briefly. A review of triangulated vortex methods is given at the end of the chapter. Chapter 4 is an extensive review of previous work investigating the emergence of multipoles from vortex instability. The discussion covers the emergence of tripoles, triangles and square vortices in experimental and numerical studies. In chapter 5 the derivation of the new vortex method, the computation of local velocities, the implementation of viscous effects and the practicalities of remeshing are explained. The method is validated in chapter 6 using internal and external checks. The method of manufactured solutions is used to test the implementations of the code, and potential flows past a cylinder and over an ellipse are simulated. To assess the performance of the method for viscous calculations, the evolution of an isolated Lamb-Oseen vortex, pairs of wing tip vortices with and without ground effect and a four-vortex wake model were investigated. The results proved that the method is robust and reliable. In chapter 7 results of the parametric study of the evolution of perturbed Gaussian distributions with a variety of initial conditions are presented. Finally conclusions and future work are given in chapter 8.

Chapter 2

Some fundamental principles

> *In the whole history of science from Greek philosophy to modern physics there have been constant attempts to reduce the apparent complexity of natural phenomena to some simple fundamental ideas and relations. This is the underlying principle of all natural philosophy ... Most of the fundamental ideas of science are essentially simple, and may, as a rule, be expressed in a language comprehensible to everyone.*
>
> *The Evolution of Physics*, Albert Einstein, 1938

In this chapter, some fundamental principles of fluid mechanics used in this thesis are introduced and explained.

2.1 Streamfunction

In fluid mechanics, the streamfunction $\bar{\psi}(x, y)$ is a mathematical parameter for two-dimensional fluids of various kinds, with a distinct physical meaning; the difference between the streamfunction values at any two points in the flow is the mass flow rate between those points. The streamfunction was introduced by the Italian-French mathematician Joseph-Louis Lagrange in 1781. Lines of constant $\bar{\psi}$ are called streamlines and used to visualise the movement of steady flow, since in such flow they are everywhere parallel to the local velocity vectors. Thus, streamlines can be interpreted virtually as solid boundaries [18, p.80] since no flow can cross them.

The usefulness of the streamfunction arises from the fact that the velocity components, u and v, of any fluid particle $\mathbf{p}$ are the partial derivatives of $\bar{\psi}$. Let's consider a flow passing between two points $\mathbf{p_1}$ and $\mathbf{p_2}$ separated by a distance ∂n with an average velocity $\mathbf{U}_{\text{av}}$ perpendicular to the line $\mathbf{p_1 p_2}$. The mass flow rate $\partial\bar{\psi}$ is defined as:

$$\partial\bar{\psi} = \rho \mathbf{U}_{\text{av}} \partial n, \tag{2.1}$$

where ρ is the density of the fluid. Rearranging Equation (2.1) leads to:

$$\mathbf{U}_{\text{av}} = \frac{1}{\rho}\frac{\partial\bar{\psi}}{\partial n}. \tag{2.2}$$

So the flow velocity can be obtained by differentiating $\bar{\psi}$ in the direction normal to $\mathbf{U}_{\text{av}}$. Adopting a sign convention such that positive is in the direction of increasing x and y, for a two-dimensional plane flow the horizontal and vertical components of the velocity are expressed as:

$$u = \frac{1}{\rho}\frac{\partial \bar{\psi}}{\partial y},$$
$$v = \frac{-1}{\rho}\frac{\partial \bar{\psi}}{\partial x},$$

where x and y are the Cartesian coordinates of $\mathbf{p}$. For an axisymmetric flow the velocities are calculated as:

$$u = \frac{1}{\rho r}\frac{\partial \bar{\psi}}{\partial r},$$
$$v = \frac{-1}{\rho r}\frac{\partial \bar{\psi}}{\partial z},$$

where r and z in this case are the radial and axial coordinates respectively and v and u are the corresponding velocities in each direction.

The above definitions apply to both compressible and incompressible flows. Solving for incompressible flow where $\rho = \text{constant}$, Equation (2.2) is rearranged as:

$$\mathbf{U}_{\text{av}} = \frac{\partial(\bar{\psi}/\rho)}{\partial n}, \tag{2.3}$$

and a new streamfunction is defined as $\psi = \bar{\psi}/\rho$, so Equation 2.3 becomes:

$$\mathbf{U}_{\text{av}} = \frac{\partial \psi}{\partial n}. \tag{2.4}$$

As a result, the velocity components in a plane flow are now expressed as:

$$u = \psi_y, \tag{2.5a}$$
$$v = -\psi_x, \tag{2.5b}$$

and in an axisymmetric flow as:

$$u = \psi_r/r, \tag{2.6a}$$
$$v = -\psi_z/r, \tag{2.6b}$$

where subscripts denote differentiation. The incompressible streamfunction ψ has similar characteristics to its general counterpart $\bar{\psi}$ with one difference, where $\partial\psi = \partial(\bar{\psi}/\rho)$ is now the flux, or volumetric flow rate, between two streamlines.

The above formulations of the streamfunction ψ satisfy the continuity equation for two-dimensional incompressible fluid, which is in Cartesian and polar coordinates respectively:

$$\frac{\partial u}{\partial x} + \frac{\partial v}{\partial y} = 0, \tag{2.7a}$$
$$\frac{\partial u}{\partial z} + \frac{\partial v}{\partial r} + \frac{v}{r} = 0. \tag{2.7b}$$

2.2 Vorticity transport equation

In fluid dynamics, the curl of the velocity field $\mathbf{U}(\mathbf{z}, t)$, where $\mathbf{z} = (x, y)$ is the position vector of a fluid element, is called vorticity $\omega(\mathbf{z}, t)$:

$$\omega(\mathbf{z}, t) = \nabla \times \mathbf{U}(\mathbf{z}, t). \tag{2.8}$$

So ω is a vector quantity whose direction is along the axis of the flow rotation, thus in two-dimensions, ω is perpendicular to the x–y plane. A fluid with vorticity is called vortex flow and has closed streamlines about a given point, but when $\nabla \times \mathbf{U} = 0$ the flow is irrotational.

The significance of vorticity for studying fluid motion arises from the fact that velocity can be calculated as an integral over the vorticity field. The motion of any fluid is described by the Navier-Stokes equations, which are a set of differential equations that represent the conservation of mass, momentum and energy. For a two-dimensional incompressible flow, these equations are:

$$\nabla \cdot \mathbf{U} = 0, \tag{2.9a}$$

$$\frac{\mathrm{D}\mathbf{U}}{\mathrm{D}t} = f - \frac{1}{\rho}\nabla P + \nu \nabla^2 \mathbf{U}, \tag{2.9b}$$

where f is the body force vector, P the pressure, ν the kinematic viscosity and $\mathrm{D}/\mathrm{D}t$ the material derivative, which in a plane flow is:

$$\frac{\mathrm{D}}{\mathrm{D}t} = \frac{\partial}{\partial t} + u\frac{\partial}{\partial x} + v\frac{\partial}{\partial y}. \tag{2.10}$$

Considering a two-dimensional incompressible fluid with no body forces, $f = 0$, the curl of the momentum equation:

$$\frac{\partial \mathbf{U}}{\partial t} + \mathbf{U} \cdot \nabla \mathbf{U} = -\frac{1}{\rho}\nabla P + \nu \nabla^2 \mathbf{U}, \tag{2.11}$$

is the vorticity transport equation, which is the governing equation of vortex method:

$$\frac{\partial \omega}{\partial t} + \mathbf{U} \cdot \nabla \omega = \omega \cdot \nabla \mathbf{U} + \nu \nabla^2 \omega. \tag{2.12}$$

The first term represents the temporal evolution of the vorticity, the second is the advection term, the third the stretching term and the fourth, which is the Laplace operator, the viscous effects.

For inviscid fluids, $\nu = 0$, under the action of conservative body forces, the vortex motion is described by Helmholtz's vortex theorem, which was published in 1858 by the German scientist Hermann von Helmholtz [6] and state the following:

1. Fluid elements initially with zero vorticity remain with zero vorticity.

2. Vortex lines move with the fluid.

3. The strength of a vortex filament is constant along its length and does not vary with time

In the case of no body forces, vorticity is conserved in the flow and Equation (2.12) becomes the well-known Helmholtz equation [19, p.14]:

$$\frac{\mathrm{D}\omega}{\mathrm{D}t} = 0. \tag{2.13}$$

To simulate vortex flows, a Lagrangian approach can be used to follow the fluid elements carrying non-zero vorticity ω by computing their velocities. Since u and v are expressed in terms of the streamfunction, a common method to do this is by using ψ, which is a solution of:

$$\nabla^2\psi = -\omega. \tag{2.14}$$

The Poisson equation (2.14) can be solved through evaluation of the Biot-Savart integral, then differentiation with respect to the coordinates in order to find the velocities. For plane flow, Equation (2.14) becomes:

$$\psi_{xx} + \psi_{yy} = -\omega, \tag{2.15}$$

and the integral is:

$$\psi = \iint G(\mathbf{z} - \mathbf{z}')\omega(\mathbf{z}')\mathrm{d}x'\mathrm{d}y', \tag{2.16}$$

where $G(\mathbf{z}) = -\log|\mathbf{z}|/2\pi$ is the Green's function. For axisymmetric flow, Equation (2.14) is:

$$\psi_{zz} + \psi_{rr} - \psi_r/r = -r\omega, \tag{2.17}$$

and the integral to evaluate is:

$$\psi = \frac{1}{2\pi}\iint \omega(z', r')(r + \varrho)(K(\lambda) - E(\lambda))\mathrm{d}r'\mathrm{d}z', \tag{2.18}$$

where $K(\lambda)$ and $E(\lambda)$ are complete elliptic integrals of first and second kind and

$$\begin{aligned} r^2 &= (x - x')^2 + (y - y')^2, \\ \varrho^2 &= (x + x')^2 + (y - y')^2, \\ \lambda &= \frac{\varrho - r}{\varrho + r}. \end{aligned}$$

2.3 Circulation

The circulation, denoted by Γ, is the line integral of velocity around a closed curve C in a flow field, so its kinematic property depends only on the velocity and the choice of C. It does not necessarily mean that the flow is rotating within the curve, but rather that the line integral is finite. The circulation is defined by:

$$\Gamma = \oint_C \mathbf{U} \cdot \mathrm{d}n, \tag{2.19}$$

where $\mathrm{d}n$ is a tangent unit vector on the curve. Γ was introduced by Lord Kelvin [7], and used independently by Frederick Lanchester in England, Wilhelm Kutta in Germany and Nikolai Joukowski in Russia during their research on the theory of aerodynamic lift [20, p.135]. In this thesis, the circulation is considered positive when it is counterclockwise, matching the mathematical sign convention of the line integral.

In vortex flows, Γ is called the strength of vorticity and can be related to it by Stokes' theorem, which states that any line integral of $\mathbf{U}$ over C is equal to the integration of $\nabla \times \mathbf{U}$ over any open surface S bounded by C [20, p.88]:

$$\Gamma = \oint_C \mathbf{U} \cdot \mathrm{d}n = \iint_S (\nabla \times \mathbf{U}) \cdot \mathrm{d}S, \tag{2.20}$$

where $\mathrm{d}S$ is the infinitesimal area enclosed within C. The above definition leads to the immediate result that if the flow within C is irrotational then $\Gamma = 0$.

2.4 Reynolds number

The Reynolds number, Re, is the ratio of inertia forces to viscous forces in a flow. It was introduced by the British scientist Osborne Reynolds in 1883 [21], and since then has become a powerful dimensionless parameter in fluid dynamics, used to identify different flow regimes, such as laminar and turbulent. Moreover, it is utilised along with other dimensionless combinations in order to provide a criterion for determining dynamic similitude in experiments and simulations. A model is said to be dynamically similar to the real application if it has the same values of the relevant dimensionless numbers, such as the Reynolds number. Re is typically defined as follows:

$$\mathrm{Re} = \frac{\rho \mathbf{U} L}{\mu} = \frac{\mathbf{U} L}{\nu}, \tag{2.21}$$

where $\mathbf{U}$ is the mean velocity, L the characteristic length and $\mu = \nu\rho$ the dynamic viscosity. For vortex flows, the Reynolds number is usually defined in terms of vortex circulation Γ:

$$\mathrm{Re} = \Gamma/\nu. \tag{2.22}$$

In turbulent flows, which are dominated by inertia forces and produce random eddies and vortices, the Reynolds number plays an important role since it defines the size of the smallest eddies, so as it increases the range of the visible scales increases. At large Re the viscous forces are weak and unable to dissipate the energy of the eddies, so smaller scales are produced until viscosity becomes of the order of the inertia forces so dissipation can take place. Therefore, Re determines also the rate of the energy dissipation.

2.5 The Lamb-Oseen vortex

The Lamb-Oseen vortex is the simplest viscous vortex in two-dimensional flows [19, p.253]. It is an exact solution of the Navier-Stokes equations, which has circular

streamlines symmetric around its axis. Its vorticity is a function of radial distance r and time t, since the vortex decays due to viscosity, and starts as an impulsive source of circulation Γ_0:

$$\omega(r,0) = \Gamma_0 \delta(x)\delta(y), \tag{2.23}$$

which leads to the exact solution:

$$\omega(r,t) = \frac{\Gamma_0}{4\pi\nu t} e^{-r^2/4\nu t}. \tag{2.24}$$

The tangential velocity of the vortex is mathematically defined as:

$$\mathrm{U}_\theta(r,t) = \frac{\Gamma_0}{2\pi r}(1 - e^{-r^2/4\nu t}). \tag{2.25}$$

Equation (2.24) clearly shows that the maximum vorticity occurs at the origin of the vortex.

2.6 Mesh types

In computational fluid dynamics, flow fields are discretised by computational elements that represent the characteristics of the flow. The discretised domain is commonly known as a mesh. Meshes may be structured or unstructured. A structured mesh is formed by well ordered volume elements, such as squares or rectangles, where a simple scheme is used to label the nodes and identify their neighbours. In unstructured meshes the control points can be joined in different ways, such as triangles or a quadrilateral form. A simple example of structured and unstructured meshes of a square domain is presented in Figure 2.1.

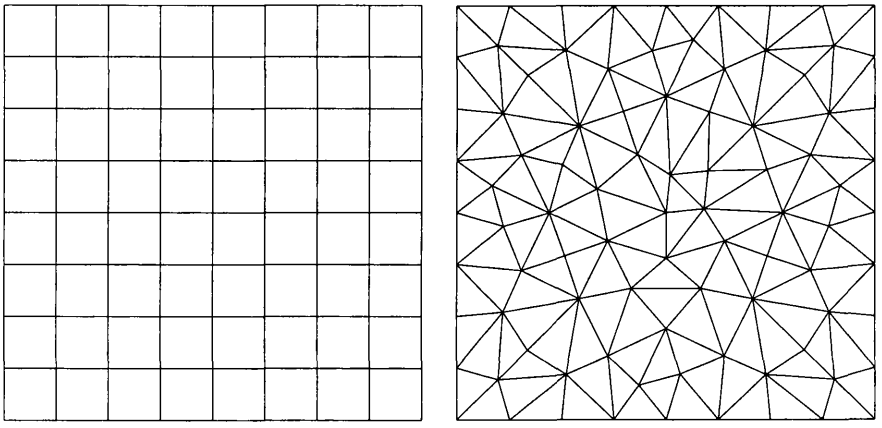

a b

Figure 2.1: Simple square meshes; a: structured Cartesian; b: unstructured triangulated.

In the early days, one-dimensional calculations were carried out on body-fitted and structured grids. Later on, models were extended to multiple dimensions to simulate realistic designs. This extension was fairly easy due to the defined structure of the mesh [12]. However, generating structured grids for complex geometrical shapes can be a serious and time consuming challenge. One technique to solve this problem was the use of multi-block structured grids [22]. The body and the far field are constructed by simple rectangular blocks, then structured grids are generated within each block. For complex problems this can be a difficult task, noting that the blocking and the grid generation process must be continually refined. Another approach uses overlapping grids, where structured grids generated about different parts of the complex geometry overlap [12].

The desire to overcome the difficulty of computing flows over complex configurations has spurred research into unstructured grids where control points can be joined in different ways. Unstructured meshes have the advantage of conforming to nearly any desired geometry. This generality, however, comes with a price; the grid generation process is not completely automatic and requires user interaction. Moreover, unstructured meshes require more information to be stored and recovered than structured grids [12].

Different algorithms exist for generating unstructured grid, especially two dimensional ones based on Delaunay triangulation [23], which is explained in §2.7. The algorithms allow the manipulation of the meshes by adding or removing points. Different bodies, such as NACA 0012, 3-element and 4-element aerofoil configurations were introduced into the mesh to show the capability of the triangulation to generate good quality grids around solid boundaries [23]. The suitability of the unstructured triangular mesh for inviscid and viscous calculations was proven by Anderson and Bonhaus [24, 25] who computed flows over aerofoils and compared the results with published data.

Nowadays, unstructured meshes, composed of triangles in two dimensions and tetrahedra in three dimensions, are very attractive because of the relatively short time required for mesh generation, and better resolution when compared with structured grids.

2.7 Delaunay triangulation

There exist many ways to connect a given set of N points into a mesh of triangles. Bad triangulations lead to thin triangles with long edges, whereas in good triangulations the edges are short and very few triangles are thin, as shown in Figure 2.2.

Finding the best triangulation for a set of N points can be computationally expensive. However, in 1934 Boris Delaunay, a Russian mathematician, introduced an affordable technique, called after him, Delaunay triangulation [26], which triangulates the points by minimising the standard deviations of the angles of the triangles, using $60°$ as the mean. Thus, Delaunay triangulation is the most equiangular triangulation and, as a result, minimises the number of long thin triangles. It is defined in terms of

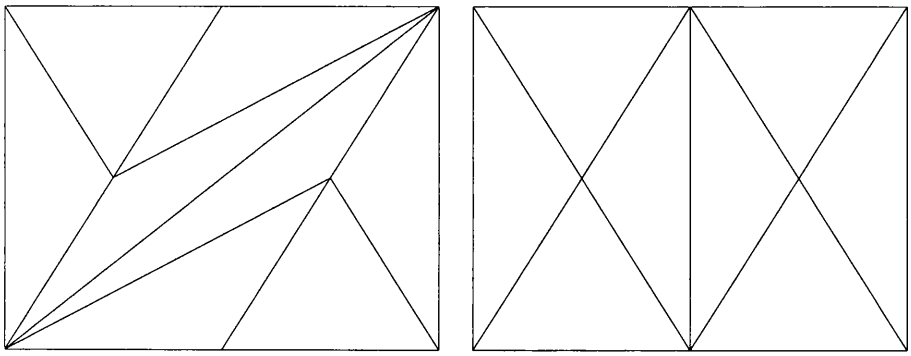

Figure 2.2: Simple example of bad and good triangulation.

the Voronoi diagram, that divides the set of N points into N convex polygons such that each polygon contains only one point, and the vertices of a given polygon are closer to the central point than to any other one. A Voronoi diagram for a set of 10 points is shown in Figure 2.3.

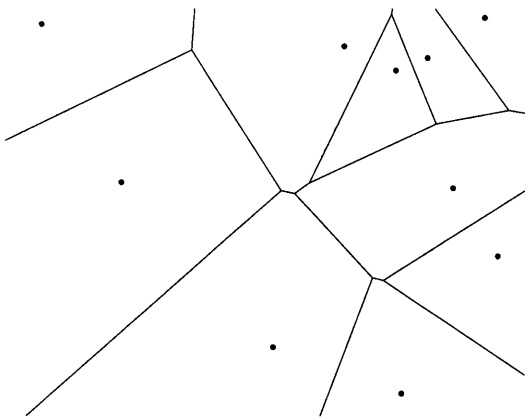

Figure 2.3: Voronoi diagram associated with 10 points.

Delaunay triangles are obtained by drawing lines between any two points whose polygons share an edge [14]. Figure 2.4 provides a simple example. Generally, the circumcircle of every triangle does not contain any other data point and the triangulation is unique. However, in the exceptional case where a polygon has a zero length edge, four points form a rectangle and lie on a circle, so clearly they can be triangulated in many different ways. Such a case requires prudent manipulation.

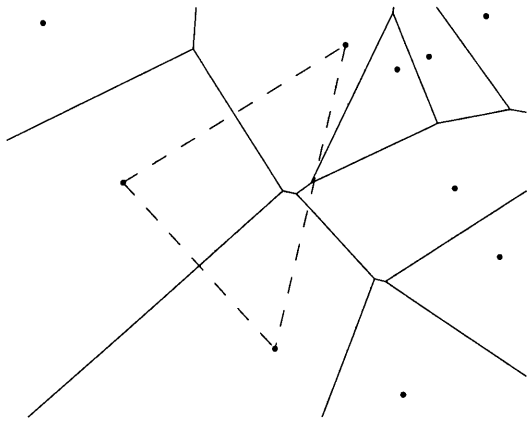

Figure 2.4: Delaunay triangulation of three points.

Chapter 3

Lagrangian vortex methods

if one talks about numerical methods ... one is just making a list of tools that are useful to know, and none of them is always better than the others whatever the problem is, each method has advantages and defects and a good numerical analyst should learn what they are in order to choose the most efficient method for the problem that he/she considers at a given time (but some postulate that their method is better than the others).

Weak convergence models for relating various scales, Luc Tartar, 2001

3.1 Introduction

Since the work of Helmholtz in 1858 [6], the study of vorticity and vortex motion has been an area of intensive research by engineers, physicists and mathematicians. Numerical investigations of vortex dynamics have been made possible by progress in numerical methods, coupled with developments of computing resources.

Vortex methods are numerical tools used for simulating incompressible vortex flows. Historically, the unsuccessful attempt of Richardson [27] to predict weather numerically by integrating the finite-difference form of the meteorological equations revealed the need for the development of new numerical techniques. It was Rosenhead's success in 1931 [28] in calculating Kevin-Helmholtz instabilities by hand using a point vortex model that demonstrated the powerful nature of vortex methods. Since then, these methods have been developed in order to study the evolution of vorticity in two and three dimensional flows. Their applications include, among many others, simulation of unsteady flows, turbulent combustion, unstable boundary layers, flows around bodies, development of wake vortices and wake-induced phenomena.

Vorticity can be studied through Eulerian or Lagrangian numerical methods, each named after the reference frame they use to track fluid motion. Eulerian methods are grid-based and follow the fluid as its moves in time through specific nodal points. On the other hand, Lagrangian methods are grid-free and track fluid motion by following fluid particles as they move through space and time. Since grid-generation is usu-

ally a computationally expensive process, Lagrangian vortex methods have been more popular than Eulerian methods.

Lagrangian vortex methods have three fundamental characteristics; first, the formulation of the Navier-Stokes or Euler equations in terms of vorticity, second, the use of one of Helmholtz' theorems [19, p.10], which states the correspondence of vorticity elements with material fluid elements, so the computational nodes are Lagrangian and convect with the local velocities, and third, the computation of the flow velocity U by integrating over the vorticity field. These features implicate the discretisation of the flow into regions of vorticity that are tracked in a Lagrangian reference frame, then, the computation of the induced velocity on each computational point. Two main techniques are used to accomplish this; evaluating the Biot-Savart integral or solving the partial differential equation for streamfunction.

The simplicity and computational efficiency of Lagrangian vortex methods have made them popular among scientists, and nowadays there exists a vast literature on this subject. Representing a continuous vorticity distribution by a finite number of elements has always been a source of inaccuracy, which motivated the development of different schemes to accomplish this task. Various models have been suggested to represent the vorticity field, the most common being point vortex elements, vorticity blobs or isolated line vortices. Comprehensive reviews of the development and applications of Lagrangian vortex methods in two and three dimensions can be found in the works of Leonard, Sarpkaya, Cottet and Koumoutsakos and Stock [29–33].

In this chapter, after presenting the different formulations of classical vortex methods, the advantages and limitations of these methods and the numerical approaches introduced to address these limitations are discussed. Then the numerical schemes used to simulate viscous effects are briefly explained before reviewing previous work on triangulated vortex methods, the group that the approach presented in Chapter 5 can be associated with.

3.2 Point vortex method

The first to use a vortex method for flow simulation was Rosenhead [28] who approximated a two-dimensional vortex sheet with a system of point vortices and followed their movement in time. In this approach, that came to be known as the point vortex method, the vorticity field ω is described by:

$$\omega(\mathbf{z}, t) = \sum_{i=1}^{N} \Gamma_i \delta(\mathbf{z} - \mathbf{z}_i(t)), \tag{3.1}$$

where $\delta(\mathbf{z})$ is the two-dimensional Dirac delta function, $\delta(\mathbf{z} - \mathbf{z}_i)=0$ if $\mathbf{z} \neq \mathbf{z}_i$. The velocity field is then computed as the solution of:

$$\nabla^2 \mathbf{U} = -\nabla \times \omega, \tag{3.2}$$

and in the presence of a solid surface in the flow, the boundary condition is:

$$\mathbf{U} \cdot \mathbf{n} = 0, \tag{3.3}$$

where $\mathbf{n}$ is the normal vector of the surface. Introducing the Biot-Savart integral, the velocity in terms of the vorticity is calculated as:

$$\mathbf{U}(\mathbf{z},t) = -\frac{1}{2\pi}\int \frac{(\mathbf{z}-\mathbf{z}_i)\times\omega(\mathbf{z}_i,t)}{(\mathbf{z}-\mathbf{z}_i)^2}\mathrm{d}\mathbf{z}_i, \tag{3.4}$$

or in terms of the circulation as:

$$\mathbf{U}(\mathbf{z}_i,t) = -\frac{1}{2\pi}\sum_{j=1,j\neq i}^{N}\frac{(\mathbf{z}_i-\mathbf{z}_j)\times\Gamma_j}{(\mathbf{z}_i-\mathbf{z}_j)^2}. \tag{3.5}$$

Even though this formulation solves the inviscid vorticity transport equation (2.13), it suffers from the singularity of the point vortices, and so can not represent accurately the vorticity field. Attempts to improve the accuracy of the point vortex method by increasing the number of elements and decreasing the time step [34] led to poor results as the vortices reached a chaotic state of motion.

3.3 Vortex blob method

The most common discretisation for the vorticity region in two-dimensional domains is that developed by Chorin in 1973 [35] where the vorticity around each computational element is modelled as a blob with a Gaussian distribution and a core size σ. Thus, in this method, the vorticity field is described by:

$$\omega(\mathbf{z},t) = \sum_{i=1}^{N}\Gamma_i\gamma_i(\mathbf{z}-\mathbf{z}_i(t)), \tag{3.6}$$

where $\gamma_i(\mathbf{z})$, commonly known as the cutoff function, is the vorticity distribution within the blob located at $\mathbf{z}_i$, and usually defined as:

$$\gamma_i = \frac{1}{\pi\sigma^2}e^{-|\mathbf{z}|^2/\sigma^2}. \tag{3.7}$$

The vortex blobs are assumed to convect without deformation with the local velocity induced by the vorticity field, which in this case can be calculated by:

$$\mathbf{U}(\mathbf{z},t) = \int \nabla\times G(\mathbf{z}-\mathbf{z}_i)\omega(\mathbf{z}_i,t)\mathrm{d}\mathbf{z}_i, \tag{3.8}$$

where $G(\mathbf{z})$ is the Green's function described in §2.2.

The convergence of the vortex blob method to an exact solution of the Euler equations has been proven for two-dimensional inviscid flows in the absence of solid boundaries [36]. But the method has its limitations. The main parameter that governs the accuracy of the discretisation is the overlap ratio h/σ, where h is the spacing between the blobs. So to obtain realistic, smooth and highly accurate vorticity distributions,

the blobs must overlap, $h/\sigma<1$, and that arrangement must be conserved during the simulation. This is generally achieved by systematically introducing more elements in the domain, which is a drawback because it affects the computational time. A numerical study of the accuracy of vortex blob methods by Barba et al. [37] showed how quickly the accuracy deteriorates if the overlap ratio is not kept small enough, usually $h/\sigma \leq 0.7$.

Moreover, the method leads to some spatial error because the shape of the blobs is assumed to remain constant, while an actual fluid element is distorted with time due to internal shear forces [29]. Early numerical investigations found that, due to this factor, the error grows exponentially in time [38]. On the other hand, simulating flows past a body with the vortex blob method is subject to significant difficulties. When the vorticity field around a solid boundary is discretised by blobs of finite core size, undoubtedly part of these blobs will lie inside the surface, which implies that some of the vorticity has crossed the boundary, a phenomenon which is physically invalid since a flow can not cross a solid surface.

3.4 Vortex filament method

In three-dimensional problems, a generalisation of the two-dimensional vortex blob method is used where the vorticity is represented by a collection of N isolated vortex filaments. The spatial configuration of a filament is given by a space curve $\mathbf{f}_i(\zeta, t)$, where ζ is a parameter along the vortex. These thin tubes have a constant circulation Γ, a core radius σ and an instantaneous length $L(t)$, $L = \int |\partial \mathbf{f}_i/\partial\zeta| \mathrm{d}\zeta$, which obey the condition $\mathrm{D}(\sigma^2 L)/\mathrm{D}t = 0$. The vorticity field is then described by:

$$\omega(\mathbf{x}, t) = \sum_{i=1}^{N} \Gamma_i \int \gamma_i[\mathbf{x} - \mathbf{f}_i(\zeta, t)] \frac{\partial \mathbf{f}_i}{\partial \zeta} \mathrm{d}\zeta, \tag{3.9}$$

where γ_i is the cutoff function as in the vortex blob method. Early filament methods used first order curves, straight lines, but later on higher order splines were implemented [31].

Using the Biot-Savart integral, the velocity field is computed as:

$$\mathbf{U}(\mathbf{x}, t) = -\frac{1}{4\pi} \int \frac{(\mathbf{x} - \mathbf{f}_i) \times \omega(\mathbf{f}_i, t)}{|\mathbf{x} - \mathbf{f}_i|^3} \mathrm{d}\mathbf{f}_i + \nabla\phi, \tag{3.10}$$

where ϕ is a velocity potential introduced to satisfy the inviscid boundary condition.

In the vortex filament method, the equations of motion are derived following two assumptions:

1. the structure of the core remains nearly constant in time;
2. disturbance wavelengths are much larger than the core radius r.

The above conditions lead to many limitations on the method, due to the fact that a filament with a constant core structure cannot represent the dynamics of a higher radial mode [30].

3.5 Advantages and limitations of classical Lagrangian vortex methods

The classical Lagrangian vortex methods enjoy some advantages, and at the same time face some difficulties. The main advantage is the discretisation of the flow in terms of vorticity, which permits the use of computational elements in areas of nonzero vorticity only, thus allowing a clear visualisation of the field especially in complex and unsteady flows. Since vorticity fields are usually compact, they can be represented by small computational domains, reducing as a result the computational cost. Simulation time also benefits from the increased stability of Lagrangian vortex methods over other numerical approaches, which allow larger time steps during calculations [33]. A comparison between finite-difference and vortex methods by Ould-Salihi et al. [39] showed that the latter are faster by up to an order of magnitude, even when the computational domain is completely filled with vorticity.

Moreover, the grid-free nature of the methods is a major advantage, as grid-generation is often a very expensive process in CFD. Another advantage is the absence of the pressure from the vorticity transport equation (2.12), so there is no need to solve for it unless force measurements are required. A summary of the benefits of Lagrangian vortex methods is presented by Chen and Marshall [40].

Despite the many advantages of Lagrangian vortex methods, such as their efficiency and their requirement of control points only where significant vorticity exists, they experience a number of serious problems and suffer a bad reputation of being incapable of modelling complex flows [37]. This fact has affected their use in the simulation of fluid dynamics problems. Beside the specific limitations for each vortex method discussed in the previous sections, they share some common disadvantages.

One challenge is the accurate simulation of viscous flows because the methods do not account for diffusion effects of vorticity due to viscosity. Thus, they are unable to simulate the evolution of the vorticity field of low Reynolds number flows. Another disadvantage of classical vortex methods is simulation time. Traditionally, the velocity computation using the Biot-Savart integral is performed on a point to point interaction basis for all control nodes, which leads to $O(N^2)$ computational time for a vorticity field with N elements, and therefore the methods can be slow for large numbers of nodes. Adding to these difficulties is the effect of the Lagrangian discretisation of the domain. As the points move with the computed fluid velocity, the vorticity distribution gets distorted, which produces a loss of accuracy in the results.

However, in the past decades, research in numerical aspects of vortex methods has been very active in order to overcome these limitations. The modelling of viscosity has profited from significant progress in numerical methods. Various schemes for the addition of viscous effects have been developed and published in the literature, but proved to lose their accuracy as the spacing of the control points increases [41]. There are at least seven established viscous schemes with various degrees of accuracy. They are, in chronological order of publication, the random walk of vortex positions introduced by Chorin [35], nowadays better known as the random vortex method RVM,

the core spreading method [42], the particle strength exchange PSE [43], Fishelov's method [44], the diffusion velocity method [45], the vortex redistribution method VRM [46, 47] and triangulated vortex methods [14]. These schemes are reviewed in §3.6.

Computation time has been successfully reduced by applying fast multipole methods [48–50], which reduced it in some cases to $O(N)$. Finally, the loss of accuracy due to distortion of nodes was tackled by the application of spatial adaption schemes, which are discussed by Barba et al. [37], such as regridding, rezoning and particle redistribution. The early techniques added a grid to the originally meshless vortex methods, introducing some interpolation error, which limited their appeal. They also restricted the accuracy that can be obtained, a limitation referred to by Barba et al. as the "initial remesh error" [37].

To bypass the limitations of classical vortex methods, new techniques are constantly being developed and published. This shows that a consensus on the "best" vortex method has not been reached yet, and the field is still maturing.

3.6 Lagrangian methods for viscous diffusion

Inviscid simulations are not always an accurate representation of real life flows, where viscosity plays an important role in diffusing the vorticity field, especially at low Reynolds number. Thus, there is a need for numerical schemes able to account for viscous effects and compute dissipation. Over the last thirty years, several models for vorticity diffusion in Lagrangian vortex methods have been suggested. Most of these schemes use an approach called "operator splitting" [35], which considers in separate steps the inviscid and viscous parts of the vorticity transport equation (2.12). So at each time step, the vorticity is first convected and then diffused. This technique resembles Prandtl's concept introduced in 1904 [8] of distinguishing the viscous and inviscid phenomena when studying flow over a surface.

Each scheme adopts a different approach to model diffusion. Some change the parameters of the vortices, for example their positions, their sizes or their circulations, while others apply a smoothing interpolant to approximate the actual vorticity distribution or change the character of the diffusion process. Lagrangian methods for viscous diffusion will be briefly reviewed in the following subsections.

3.6.1 Random walk method

The random walk method, or the random vortex method (RVM), was proposed by Chorin in 1973 [35] to simulate slightly viscous flows. The idea is to perturb the position of the particles carrying vorticity by random displacements that have zero mean and a variance equal to twice the product of the kinematic viscosity and time step. The displacement of the particles spreads them, representing the diffusion of vorticity. RVM uses the splitting algorithm: the vorticity field is first updated by a

convection step, then subjected to the random walk equation:

$$\mathbf{z}_i(t+\Delta t) = \mathbf{z}_i(t) + \xi_i(t), \quad i = 1, 2, \ldots, N \tag{3.11}$$

where ξ_i are random numbers with a Gaussian distribution. The method has been applied for flows in free-space and over solid boundaries [51, 52], and its convergence to the Navier-Stokes equations has been proven. However, previous work has shown that in order to achieve accurate results the number of particles needs to be large [29], as RVM suffers from an error of $O(\sqrt{\nu/N})$.

The random walk method enjoys some advantages, which make it extensively used for studying various engineering problems. Shankar [46] provided a comprehensive summary of the different applications of RVM. Mainly, the method is simple, easy to implement, especially when simulating flows around solid geometries, preserves the grid-free formulation of vortex methods and conserves the total circulation. On the other hand, RVM suffers from some important disadvantages. For example, it can not model the full range of viscous flows, as the lower Reynolds number limit is around $\mathrm{Re} = 100$ [37]. The method also introduces an error in the position of the vortex system since it is not capable of conserving the mean size and location of the vorticity in free space, which pose difficulties in the physical interpretation of the results. This error can render the computed solution noisy and causes symmetric flows to become asymmetric. The impact of the error can be reduced by augmenting the number of vortex particles, as mentioned earlier, but this will increase convergence time, a major limitation in numerical simulations.

3.6.2 Core spreading method

In the same year as the introduction of the random vortex method, Kuwahara and Takami [42] presented a new technique based on vortex blobs with varying cores, which they used to compute the motion of a vortex sheet in an inviscid fluid. Their aim was to use the velocity field of a diffusing vortex to eliminate the large velocities induced by the point vortices. Later on, Leonard [29] adapted the method for the simulation of viscous effects, when he allowed the blob cores to expand according to the diffusion equation.

The core spreading method is analogous to the evolution of the Lamb-Oseen vortex described in §2.5. Taking the discretising equation of the vorticity field in vortex blob methods, Equation (3.6), with a Gaussian cutoff function, Equation (3.7), the core size of a blob, σ, is chosen as a function of viscosity and time, and formulated to satisfy the viscous term of Equation (2.12) as follows:

$$\sigma = \sqrt{2\nu t}, \tag{3.12}$$

$$\frac{\partial \sigma^2}{\partial t} = 2\nu. \tag{3.13}$$

As a result, the computation of the core expansion is done via the simple equation:

$$\sigma_i^2(t+\Delta t) = \sigma_i(t) + 2\nu\Delta t, \quad i = 1, 2, \ldots, N \tag{3.14}$$

Even though the core spreading method is deterministic, simple to implement, grid-free, does not use the operator splitting approach and converges faster than the RVM, its application has been limited since Greengard [53] proved it inconsistent as it does not converge to the Navier-Stokes equation in the convection term. The error is caused by the advection without deformation of large vortex blobs. Rossi in 1996 [54] resurrected the method by proposing a splitting scheme to correct the core spreading method, in which the large vortices are divided into smaller ones, and proving that this approach converges. However, the splitting technique increases the number of vortices exponentially in time and introduces some numerical diffusion [37].

3.6.3 Particle strength exchange

After the core spreading method was shown to approximate the wrong equation [53], a number of researchers introduced new deterministic techniques to simulate viscous diffusion based on the splitting approach of the vorticity equation. These methods assign initial circulations to uniformly distributed particles, then compute the diffusion effects due to the changes in the element strengths. The changes can be interpreted as the exchange of vorticity between neighbour particles, the reason why these methods were called particle strength exchange (PSE), also known as circulation redistribution [33]. Degond and Mas-Gallic [43] are usually credited with the creation of PSE after their work on diffusion operators, which was the origin of the method.

Particle strength exchange is described in detail by Cottet and Koumoutsakos [32, p.145]. In the scheme, the circulation of every element is considered an unknown variable that changes with time due to viscosity, and the Laplacian at a particle's location is approximated by an integral operator:

$$\nabla^2\omega(\mathbf{z}) \approx \int \mathrm{G}_\sigma(|\mathbf{z}-\mathbf{z}_j|)[\omega(\mathbf{z}_j)-\omega(\mathbf{z})]\mathrm{d}\mathbf{z}_j, \tag{3.15}$$

where $\mathbf{z}_j$ is a neighbour particle to $\mathbf{z}$. Using a Gaussian smoothing function, G_σ is calculated as:

$$\mathrm{G}_\sigma = \frac{2}{\pi\sigma^2}e^{-|\mathbf{z}|^2/2\sigma^2}. \tag{3.16}$$

The integral in Equation (3.15) is discretised using the particle positions as quadrature points.

The main disadvantage of PSE is its reliance on the uniformity of the particle distribution. Originally, the method's formulation was grid-free, but since its accuracy relies heavily on the quadrature rules used to discretise the integral, the scheme requires nearly uniformly spaced particles at every time step. This encouraged the use of remeshing techniques in vortex methods [55], which, as Barba et al. [37] claimed, caused some debate between researchers, because it was considered that the grid-free nature of the methods was weakened, especially when remeshing based on regular grids was applied. Using a mesh renders the handling of flows over complicated geometries difficult, and interpolation to the grid introduces numerical errors. Although these errors are generally small, they have a greater effect on the accuracy of the vortex

method when simulating high Reynolds number flows, where the numerical diffusion can submerge small scale viscosity.

3.6.4 Fishelov's method

In 1990 Fishelov [44] proposed a new deterministic method, based on convolving the vorticity ω with a cutoff function $\gamma(\mathbf{z})$, then approximating the Laplace operator in the vorticity transport equation by explicit differentiation of $\gamma(\mathbf{z})$. Thus, the computation of viscous diffusion is simply achieved by integrating the convolution. The mathematical formulation of the scheme is as follows:

$$\omega \approx \gamma * \omega, \tag{3.17}$$

$$\nabla^2\omega \approx \nabla^2(\gamma * \omega) = \nabla^2\gamma * \omega. \tag{3.18}$$

The numerical approach is determined by the choice of cutoff function, and resembles particle strength exchange due to the fact that the diffusion operator is approximated by an integral one. But Fishelov [44] claimed that her method is less complicated and easier to apply than PSE. The author showed that the scheme is accurate when applied to the Navier-Stokes equations, and stable for the heat equation if the cutoff function is chosen to have a positive Fourier transform.

However, Fishelov's method has similar disadvantages to those of PSE, as it loses accuracy when the domain becomes distorted [46], therefore requiring periodic remeshing on a fixed grid to counter the problem.

3.6.5 Diffusion velocity method

Degond and Mustieles [45] proposed in 1990 a new particle method for the computation of convection-diffusion problems by modelling diffusion as part of the convection process, and applied it in plasma physics. Ogami and Akamatsu [56] extended the method to study vorticity dynamics by integrating the diffusion term into the convection one in the vorticity transport equation (2.12). The name of the method comes from the fact that viscous diffusion is represented by adding the diffused velocity to an artificial velocity field in order to convect the particles. Later on, Ogami and Cheer [57] extended the scheme to simulate compressible flows.

The diffusion velocity method conserves the grid-free nature of Lagrangian vortex methods, which is an advantage over PSE and Fishelov's technique. But unfortunately, the scheme has its disadvantages: Clarke and Tutty [58] found that the method requires particles to overlap in order to accurately model diffusion, and that this arrangement must be always maintained. Moreover, the velocity diffusion is proportional to the gradient of vorticity and to ν/ω, which causes serious difficulties in regions of large vorticity gradients and zero vorticity. Degond and Mustieles' [45] simulations showed some numerical oscillations in areas of vanishing vorticity, which was a sign of instability. This fact prompted the authors to acknowledge that the diffusion velocity method might be less accurate than other schemes for the Navier-Stokes and heat equations.

3.6.6 Vortex redistribution method

The dependence of PSE and Fishelov's method on remeshing to fixed grids encouraged Shankar and van Dommelen [46, 47] to develop a new grid-free scheme for handling diffusion, which they called the vorticity redistribution method (VRM). The approach, like previous deterministic particle methods [43, 44], simulates diffusion through element circulation exchange, but unlike PSE and Fishelov's scheme it does not use an integral operator. At every time step, viscous effects are modelled by letting a fraction of the circulation of each vortex in the domain move to neighbouring nodes using a special system of equations. This fraction is referred to as strength fraction and denoted as f_{ij}^t. Selecting the neighbours and calculating the circulation fractions are critical in VRM, as they determine its accuracy, stability and conservation properties.

The former operation is achieved by considering all nodes within a specific distance from element i as its neighbours. The authors defined this distance to be proportional to the typical diffusion distance during a time step δt, $h_\nu = \sqrt{\nu \delta t}$. So a vortex j is neighbour to i if:

$$|\mathbf{z}_i - \mathbf{z}_j| \leq k h_\nu, \tag{3.19}$$

where k is a constant chosen following some criteria [46, §6.2.3]. Then the strength fractions f_{ij}^t are found by solving a system of equations that conserve circulation and linear and angular momenta.

Since f_{ij}^t indicates the vorticity diffused from i to j, and reverse vorticity flow is not a natural phenomenon in a flow field, Shankar and van Dommelen enforced the positivity of f_{ij}^t as a condition for an acceptable solution in order to ensure stability. In case the system of equations generates $f_{ij}^t \leq 0$, new elements are added in the vicinity of i and a new solution is attempted. The addition of nodes is repeated until an acceptable solution is achieved. This process can lead to a dramatic increase in the number of particles, making the simulation more expensive. The authors alleviated this problem by particle merging.

The advantage of the vorticity redistribution method is mainly its grid-free nature. However, this comes at the expense of its computational time. Searching for neighbours for each element and solving the N systems of equations at every time step slow down the simulation. The size of the system determines the accuracy of VRM. First order accuracy requires six neighbours per node, while a larger number leads to higher orders of accuracy [47].

3.6.7 Triangulated vortex methods

To bypass the limitations of the previous viscous schemes, §3.6.1–§3.6.6, new deterministic approaches based on triangular and irregular meshes with various techniques to include viscosity have been published. In these methods, the triangulated vortex methods, the computational domain is discretised by elements connected by Delaunay triangulation and the vorticity is approximated at each node. This fact means that, unlike vortex blobs, when simulating flows around solid bodies the vorticity field does not penetrate the surface [16]. Besides their convergence to the Navier-Stokes equations,

the primary advantages of triangulated vortex approaches are their grid-free nature, their ability to reduce computational time and simulate flows around complex geometries. Though the use of irregular grids is not new – Liszka and Orkisz used them for finite difference method [59] – their development was dependent on the progress of computer speed and memory.

In 1993, Russo [60] used vortex blobs to represent the vorticity field, and handled diffusion by approximating the Laplace operator in Equation (2.12) on a triangulation of the blob positions obtained from a Voronoi diagram. The approximation is done by assigning a weight coefficient β_{ij} to every vortex, which is a function of the position of the element. Russo stated that β_{ij} is "not uniquely defined and depend[s] on the particular discretization of the Laplacian" [60]. Once the system of equations is solved, vorticity convects with the velocity field, and its diffusion is modelled by changes in the weight coefficients. The author applied the technique to study two-dimensional unbounded flows and proved that it conserves vorticity and angular momentum.

Later on, Russo and Strain [14] abandoned the vortex blobs and published a new method based completely on Delaunay triangulation. However, its application was two-dimensional inviscid flows. In this approach, the vorticity varies in a piecewise linear manner over triangles. An adaptive approximation scheme is used to construct the initial distribution of the vortices from the initial vorticity field. Then, the velocity field is computed by evaluating the Biot-Savart integral using a fast multipole method with a continuous source distribution, to reduce the computational cost. At every time step the vertices are moved and the triangulation is efficiently reconstructed to maintain high accuracy for a long period. Numerical experiments showed that the triangulation represents the vorticity field better than equal-size blobs. Therefore, the current method is more accurate that the vortex blob methods, but its computational cost is slightly higher due to the construction of the triangulation at each time step.

Huyer and Grant [15] extended the method of Russo and Strain [14] to simulate two-dimensional unsteady flows past solid bodies. The vorticity is represented by a linear interpolation on the points connected by Delaunay triangulation, and used to solve the Biot-Savart integral. On the other hand, the surface vorticity satisfies the no-slip boundary condition and is transported into the flow by viscous diffusion. To compute the Laplacian, the authors used a similar technique to the one introduced by Marshall and Grant [41] for axisymmetric, viscous flows. To model viscous diffusion, the vorticity is represented at every computational element i by a second order polynomial function fitted to a set of control points neighbouring i; then the first- and second-order derivatives of vorticity are acquired by differentiating the function. The unknown coefficients in the polynomial expansion are solved for in a least-squares sense. Once the first- and second-order derivatives are found, the control points are advected by the diffusion velocity method of Ogami and Akamatsu [56], which moves the particles by the total velocity field, which is the summation of the induced velocity calculated by the Biot-Savart integral and the diffusion velocity. The triangulation is updated after the movement of points. This method was tested and found highly accurate for irregular points, unlike PSE and Fishelov's method [41]. Numerical solutions for impulsive flows past a circular cylinder and a flat plate were stable and in good

agreement with experimental results [15].

Russo and Strain's method [14] was extended even further by Marshall et al. [16] to compute incompressible, three-dimensional, viscous flows. They used a tetrahedral mesh constructed by Delaunay triangulation to discretise vorticity, which varies linearly within each tetrahedra. They evaluated the Biot-Savart integral via a fast method: the flow field is divided into three regions, where an analytical integration is used for the elements in the near field, Gaussian quadratures for moderately distant elements, and a multipole expansion acceleration for the far field elements. Viscous effects are computed by approximating the vorticity with a quadratic polynomial at each node i, and then finding the derivatives of the stretching and diffusion terms in Equation (2.12) using a moving least-squares method similar to that of Marshall and Grant [41]. When simulating flows past solid bodies, the surface vorticity is calculated taking into account the vorticity diffused from the geometry and the vorticity contained within the tetrahedra related to the boundary points. The method of Marshall et al., like other triangulated vortex methods, avoids vorticity penetration into solid surfaces, and offers accurate results even when the mesh is highly irregular. Simple simulations of uniform flow past a sphere at Reynolds number 100 proved the validity of the method.

3.7 A triangulated vortex method for inviscid flow

Beside being used for computing viscous effects, Russo and Strain's [14] triangular method was coupled by Carley [17] with an original approach to evaluate the Biot-Savart integral, in order to investigate unsteady axisymmetric inviscid flows. In such flows, as explained in §2.2, the integral for the streamfunction equation (2.18) contains elliptic integrals which become singular once the source point approaches the field point. This difficulty can be overcome when computing the induced velocity field by applying specialised approximation schemes, which usually are complicated to encode, inefficient and time consuming. However, Carley's approach circumvents this problem by integrating over a triangulated vortex disk with a linear vorticity distribution, without using the elliptic integrals in the calculations for an element to element interaction. With movement of the control points, the triangulation gets severely distorted, which affects the mesh quality and leads, as a result, to inaccurate approximation of the vorticity field. This is circumvented by remeshing the computational domain in order to restore the point distribution. Simulations of the motion of Norbury rings and the interaction of two initially identical circular core rings agreed with previously published results and proved the reliability of the method. The computational time was reduced from the classical $O(N^2)$ to $O(N)$.

Triangulated vortex methods have several advantages over other viscous schemes. They are grid-free, can be used with highly irregular point distributions, reduce computational cost, and proved to be reliable to compute various type of flows in two and three dimensions. For these reasons, the numerical method developed in this thesis will be based on a triangular vorticity scheme, where the nodes discretising the computational domain are connected by a Delaunay triangulation and the vorticity is

approximated at each triangle. For viscous calculations, the Laplacian is approximated at each node, then solved in a least-squares sense.

Chapter 4

Emergence of multipoles from vortex instability

What I am about to say on the phenomena of turbulent flows is still far from conclusive. It concerns, rather, the first steps in a new path which I hope will be followed by many others.

Ludwig Prandtl, 1926

4.1 Introduction

Turbulence is an irregular fluid motion characterised by chaotic changes such as rapid variation of pressure and velocity in space and time. Historically, vorticity and turbulent movement were believed to be random and unstructured, thus scientists were unable to understand the origin and progress of turbulence. In 1926 Ludwig Prandtl announced that "the researches on the problem of turbulence which have been carried on at Gottingen for about five years have unfortunately left the hope of a thorough understanding of turbulent flows very small. The photographs and kinetographic pictures have shown us only how hopelessly complicated this flow is" [10]. Undoubtedly, this was "an area that physicists have had difficulty explaining" [61]; as a result, they were incapable of studying turbulent vortices that occur in different forms throughout the universe. However, McWilliams' observations of vorticity concentrations arising from random initial conditions in turbulent flows in 1984 [11] fundamentally changed this fact. He showed that turbulence is, in essence, more structured than had been previously thought. His numerical study demonstrated how the flow changed from random and disoriented to organised structures, with the emergence of mostly monopolar isolated vortices that tend to assume axisymmetric shapes. An isolated vortex is one that has a core of a given sign surrounded by a ring of opposite sign, so that total circulation is zero.

These observations were soon followed by the experimental investigation of Couder and Basdevant on two-dimensional turbulence in thin liquid films [62], which showed

the spontaneous formation of vortex dipoles in unstable Von Kármán wakes. This striking visualisation motivated the authors to study the structure, behaviour and rôle of these vortices numerically and experimentally.

Since then, it has been well established that relaxing turbulent flow approaches a stable state after a long time evolution. The dynamics of two- and three-dimensional turbulent flows are intensely dominated by the self-organisation of vorticity into so-called 'coherent structures'. The emergence, evolution, interaction and persistence of these structures have become a fascinating subject for scientists due to the physical relevance of these phenomena in many areas, since they carry finite fluid volumes far away from the area of their production, affecting the transport of energy. Studying coherent structures has made turbulent flow, which was considered one of the great unresolved problems of classical physics, less mysterious and its dynamical understanding possible.

Examples of coherent vortices can be found in atmospheric and oceanic movements with the formation of cyclones and oceanic eddies. For example, the Gulf Stream that originates in the tropical Gulf of Mexico moves north in the Atlantic Ocean, bringing warm water to north-west Europe and affecting its climate [63]. Vortices are even found in astrophysical environments such as the Great Red Spot on Jupiter [64], first seen in 1664, the emergence of a new red spot, Red Spot Jr., in 2006 [65] and turbulence in the Sun that is involved in moving the star's nuclear energy from its inner core to the outer layers [66]. The Great Red Spot and Red Spot Jr. on Jupiter are shown in Figure 4.1. Moreover, coherent vortex structures have been observed in pure electron plasma flows and their nonlinear self-organisation and transport have been intensely studied [67].

Fluid dynamicists carried out investigations on the relaxation of vorticity mainly for two-dimensional flows because it has been experimentally proven that any rotating or stratified fluid can be realistically studied as two-dimensional [69, 70]. The most observed coherent structures that arise from a variety of situations are monopolar and dipolar vortices. The former consist of closed streamlines and have zero linear momentum but non-zero angular momentum. It was concluded that monopolar vortices approach axisymmetry as their natural asymptotic state [71]. The latter are self-propelling pairs of counter-rotating vortices. Other forms of coherent multipolar vortices, though rare, were also found to exist in two-dimensional flows. They include tripoles and triangular vortices, which consist of a vortex core surrounded by a number of vortex satellites of opposite sign.

In this chapter, the previous experimental and numerical investigations on the emergence of tripoles and high-order multipoles will be reviewed.

4.2 Previous work on the tripole

The tripole has received more attention in the literature than other multipolar vortices. It is a linear arrangement of three patches of vorticity of alternate sign: an elliptical core bordered by two weaker satellites at its longer sides as shown in Figure 4.2. In

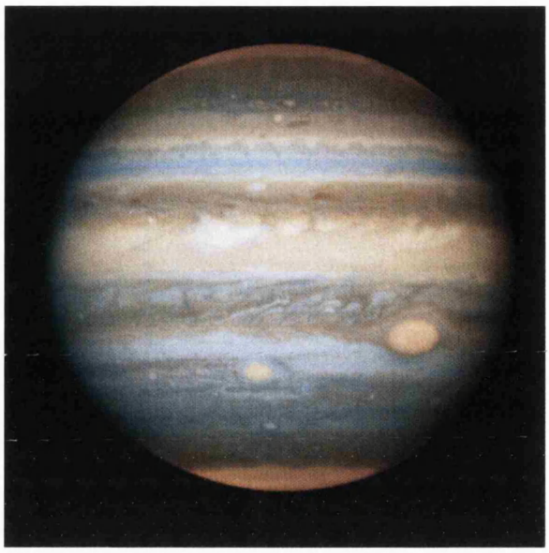

Figure 4.1: Image of Jupiter taken by the ACS/WFC on board of the Hubble Space Telescope on 16 April 2006. Two red spots can be seen: the Great on the right-hand side and the Junior in the middle of the southern hemisphere of the planet [68].

order of complexity, it comes after the monopole and the dipole, and has a quasi-steady rotation around its central axis in the same direction as the circulation of the core vortex.

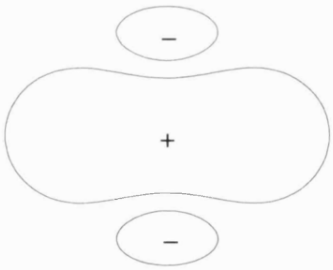

Figure 4.2: Structure of a tripole vortex.

Larichev and Reznik [72] were the first to observe, while investigating the results of solitary Rossby wave collisions, that tripoles can be produced from the collision of two asymmetric dipoles. However, they noted that the result of the collision depends essentially on the wave parameters.

Rossby waves, also known as planetary waves, are one of the most intriguing large scale oceanic and atmospheric motions that are produced by the shape and rotation of the Earth, and always travel from East to West. They were first mathematically

modelled by the Swedish meteorologist Carl-Gustav Rossby in 1939 [73] before being confirmed by satellite observations. These waves are characterised by the big difference in their horizontal and vertical scales, which makes them difficult to spot; usually, their horizontal scale is of the order of hundreds of kilometers, while their amplitude of oscillation is just few centimeters. When they are not periodic, Rossby waves are said to be solitary.

In 1984, Leith [74] argued numerically that it is possible to obtain a tripole by destabilisation of an axisymmetric vortex. Moreover, in 1988 the two-dimensional numerical simulations of Flierl [75] suggested that a shielded monopole might break up into a tripole. This was proven to be correct by numerous numerical and experimental studies later conducted on the subject. Shielded vortices were widely investigated due to their significance in the understanding of large scale turbulence since they appear frequently in Gulf Stream rings; this can be clearly observed in Figure 4.3, which shows the velocity of the Gulf Stream on Thursday 1st of February 2007. On the other

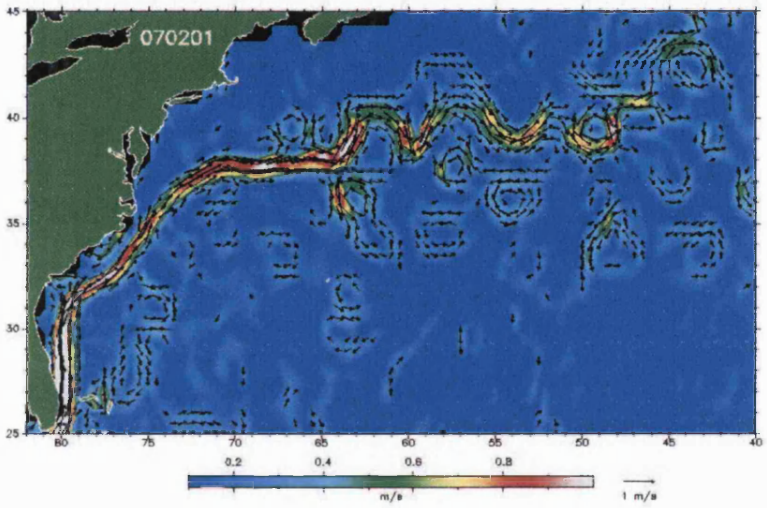

Figure 4.3: Gulf Stream velocities on Thursday 1st of February 2007 [76].

hand, Benzi et al. [77] predicted through numerical simulations that a tripole may emerge as a coherent structure from a two-dimensional randomly initialised turbulent flow.

It was not until 1988 that Legras et al. [78] observed the spontaneous emergence of tripolar vortex structures in their numerical simulations of randomly initialised two-dimensional turbulence and claimed that, to the best of their knowledge, it was the first time that a stable tripole had been analyzed. This new structure had three different vorticity regions with "a complicated shape which does not coincide with a simple curve, a circle or an ellipse" [78]. In their study they identified that for the tripole to emerge, the ratio of forcing timescale to turnover time, which is the time that the structure takes to complete one full revolution, $(t_{\mathrm{forc}}/t_{\mathrm{turn}})$ has to be very large.

4.2.1 Tripoles emerging from shielded monopole in rotating fluid

The first laboratory tripole was reported by van Heijst and Kloosterzeil [79] who observed the accidental emergence of a tripolar structure while studying the dynamics of barotropic vortices in rotating fluids. A barotropic vortex is one where the viscous diffusion of vorticity is negligible [19, p.1]. The authors found that under certain conditions the counterclockwise vortices became unstable and developed into a tripole that rotated as a solid body. These conditions were not explained in the article. Due to its persistence in the highly sheared fluid environment, van Heijst and Kloosterzeil concluded that the tripole seemed stable, thus making it possible for it to exist in natural geophysical flows. It was not long indeed before infrared images, Figure 4.4, taken by the satellite NOAA-11 in early 1990 emerged showing the existence of an oceanic tripole that lasted for 4 days in the Bay of Biscay [80]. The core of this structure measured about 50–70 km and rotated clockwise.

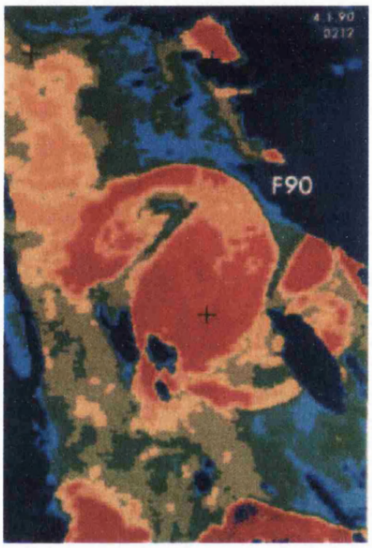

Figure 4.4: Infrared image, taken by the NOAA-11 satellite on 4th of January 1990, of a tripole in the Bay of Biscay. The cross in the centre is at 45° north, 4° west [81].

Previous numerical and experimental results brought attention to the tripolar vortex, and several investigations into this new structure followed. Carton et al. [82] performed a series of simulations using spectral methods to investigate the instability of perturbed isolated monopolar vortices. Their work showed that the unstable vortex due to the growth of wavenumber-2 instabilities evolved into a stable tripolar state, and provided detailed information about the vorticity distribution during this process. A wavenumber, which is the spatial analogue of frequency, is a wave property inversely related to wavelength. The authors explained that the evolution of tripoles depended on the steepness of the vorticity gradient, and was accounted for by the growth and saturation of instabilities. Their results agreed well with the experimental findings of

van Heijst and Kloosterzeil [79].

Then Polvani and Carton [69] conducted a numerical study to examine the existence and stability of two-dimensional tripolar vortices. They represented the tripole by three vertical elliptic vortices, where the satellites are left and right of the centre. Using a contour dynamical algorithm, they were able to determine the parameters for rotating tripolar states that are exact nonlinear solutions of the inviscid two-dimensional Euler equations. They showed that some parameters lead to stationary vortices with zero angular velocity, but these were "almost invisible" because their generated velocity fields decreased very rapidly away from them. The rotating tripoles were found to be robust under small perturbations, though when heavily disturbed they either tended to axisymmetry or broke up into two asymmetric dipoles. Then, using a pseudospectral code, Polvani and Carton [69] confirmed the previous results and showed the many possibilities for generating continuous tripoles from three elliptic vorticity patches as initial conditions.

In order to elaborate on their previous results, van Heijst et al. [83] published an extended article in which they presented more detailed characteristics of the tripolar vortex observed in [79], such as the rotation speed and the decay of the tripole due to viscosity. They also provided results for some flow properties such as the vorticity and the streamfunction. The tripole emerged as the end-state of a shielded axisymmetric monopole, which consisted of an anticlockwise centre surrounded by an opposite sign vortex ring with zero total circulation. The unstable monopole evolved in such a way that the core preserved its positive vorticity while its shear tore the ring, which reorganised itself into two satellites, one on each side of the centre. Once formed, the tripole rotated as a solid body around its central axis in the direction of the core. Initially, the satellites increased their strength due to vorticity advection but later on the structure started to decay. This decay, due to viscosity, was apparent from the horizontal expansion of the tripole and the decrease in its rotational speed. In the same article while discussing the stability of the structure, van Heijst et al. showed some figures illustrating the evolution of an unstable tripole. In this case the topology of the vortex drastically changed when the central core split into two halves each pairing with one of the satellites, forming two dipoles that moved in opposite directions. The authors concluded that this can happen only when the initial vortex core is unstable.

However, Kloosterziel and van Heijst [84] revealed that not every isolated monopole evolves into a tripole. During their experimental investigation, they found that cyclonic and anticyclonic vortices behave completely differently. Only cyclones, which are vortices characterised by inward spiraling motions rotating counterclockwise in the northern hemisphere and clockwise in the southern hemisphere of the Earth, evolved into tripoles by a similar process to that described in [83]. On the other hand, the anticyclones, which are the opposite to cyclones rotating clockwise in the northern hemisphere and counterclockwise in the southern hemisphere, were very unstable and directly split into two dipoles that moved away from each other. In some cases, the anticyclonic vortices evolved into high order multipoles before breaking into two dipoles. The authors suggested that this behaviour was due to centrifugal instability. While the cyclones suffered only slightly from it, the anticyclones were centrifugally unstable,

which prevented the flow from achieving the right conditions for tripole formation. Through Rayleigh's stability analysis, Kloosterziel and van Heijst concluded that only weak anticyclones are centrifugally stable.

The role of the centrifugal instability in the different behaviour of the cyclones and anticyclones was investigated by Orlandi and Carnevale [85] through three-dimensional numerical simulations. They found that for the anticyclonic vortex the centrifugal instability increased the vorticity gradient between the core and its surrounding ring, hence increasing the instability of the monopole, which led to the formation of two dipoles or higher order multipoles. In the cyclonic case, however, the effect of the centrifugal instability was weak and did not affect the stability of the core. In fact, some results shown proved that this instability can play a stabilising role for the cyclone by broadening the annulus of the shielded monopole. Finally, Orlandi and Carnevale found that it was possible for a stable tripole to emerge from an anticyclone as long as the centrifugal instability is weak or the vorticity gradient between the core and the annulus of the initial monopole is small. This observation, in a way, supported the conclusions of Kloosterziel and van Heijst [84].

Orlandi and van Heijst [86] studied numerically the experimental tripole of van Heijst et al. [83]. In addition, they investigated the collision of two identical Lamb dipoles vertically separated by an offset distance ϵ, a study similar to that of Larichev and Reznik [72] but on the f-plane, which is a two-dimensional rotating horizontal approximation of the spherical Earth. The rotation rate of the plane f, known as the Coriolis parameter, is calculated as $f=2\Omega \sin \phi$, where Ω is the Earth's angular velocity and ϕ the latitude, and is assumed to be constant when describing atmospheric and oceanic motions with time scales smaller than or equal to $1/f$. The parameter f is zero at the equator, and increases with latitude until it reaches its maximum at the pole. Figure 4.5 is a sketch of the initial conditions studied by Orlandi and van Heijst.

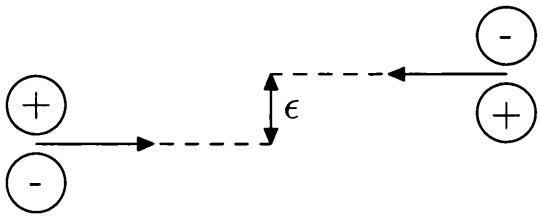

Figure 4.5: Dipoles separated by a vertical offset distance ϵ.

The results for this case showed that the offset distance ϵ between the dipole axes played a critical role in the outcome of the collision. The authors tested three values for ϵ=0.5, 1.0 and 1.5 during their study. For the smaller one the colliding dipoles exchanged negative vortices and the newly formed pairs travelled in opposite directions. In the larger distance example the dipoles passed each other without significant change to their structure. However, for ϵ=1.0 the collision gave birth to a tripole. In this special case, the centres of the positive vortices lay on the same line, so when they collided they merged into one vortex that was surrounded by the two negative vortices.

After a period of reorganisation, the structure had a well-defined tripolar shape, and rotated as a solid body. This result indicates that the β-effects, as in [72], do not play a significant role in the formation of the tripole.

The parameter β represents the latitudinal gradient of the Earth's angular velocity Ω, denoting as a result the latitudinal variation of the Coriolis parameter f. It is zero at the pole and reaches its maximum value at the equator [87, p.217]. The β-plane approximation is the linear variation of f in space, so it is the tangent plane to the surface of the Earth at a given latitude [87, p.152]. The β-plane is used when studying geophysical fluid dynamics to cast the relevant dynamics in a planar, Cartesian coordinate system rather than a spherical one. In this plane, the β-effect is the local change of the vertical component of vorticity [87, p.217].

To simulate the formation of the tripole observed in [83], Orlandi and van Heijst [86] applied a random spatial distortion to a shielded monopole and let it evolve freely. This technique is similar to that of Carton et al. [82] but without the specific azimuthal perturbation applied by them. As in the experiments, the centre of the initial vortex conserved its shape and the ring separated into two satellites around the core forming a tripole. This vortex had similar initial rotation and exponential decay to the experimental one, but became faster in later stages. The authors found that the tripole stability was proportional to the steepness of the initial vorticity distribution, in agreement with the conclusions of [82], and that the stable tripole had stronger satellites, which decreased its angular velocity. Analysing the vorticity-streamfunction relationship in the three vortices forming the tripole, they found that it is linear only in the core. They noticed as well that the ω-ψ relationships for the tripole formed by the colliding dipoles and for that which emerged from an axisymmetric monopole were different, clearly indicating that the tripolar structure does not have a unique solution, a result already proven by Polvani and Carton [69].

The evolution and decay of tripoles from unstable shielded circular vortices was analysed numerically by Carton and Legras [88]. They identified three stages during the transformation process from an isolated monopole to a tripole. In the first, they observed a linear increase of the perturbation that affected the outer ring, folding it into two satellites and creating three patches of vorticity. The second stage was the nonlinear growth of the satellites by pulling away some vorticity filaments from the central core, which amplified their magnitude. The final stage was the saturation of the structure with the three patches of vorticity aligning themselves under the tripolar form. This result explained the experimental observations of van Heijst et al. [83]. Using a simple elliptical model for the core and two point-vortices for the satellites they investigated the stability of the tripole. They concluded that the total angular momentum of the vortex played the key role in splitting the structure into two dipoles, as reported in [83], instead of the formation of a stable tripole whose existence required the magnitude of the angular momentum to be large enough. Finally they showed that after a long life-span, continuous stripping and diffusion of the core broke the symmetry of the tripole and led to an oscillatory behaviour of the core between the two satellites. This phenomenon was observed here for the first time.

Tripoles were also observed to emerge from the interaction of two similar co-

rotating two-dimensional shielded vortices. Carton [89] studied numerically the evolution of such vortices under different initial conditions. Their core vorticity was constant, but the core radii, the distance separating both vortices, the ring radii and their intensity were variables. He observed that when the cores were small and the rings were weak, the shear exerted by the vortices on each other was strong enough to just split the annuli but not the cores. The torn vorticity reorganised itself into satellites, thus creating two co-rotating tripoles that never merged. This case is of special interest because it is an equilibrium state between merging and breaking.

4.2.2 Tripoles in non-rotating flows

The first to experimentally investigate tripolar vortices in non-rotating stratified fluid were Flor et al. [90] who induced vorticity motion using two different mechanisms: a rotating sphere and a rotating bent rod. It was found that while the sphere generated axisymmetric, stable monopoles, the rotating rod led to unstable monopolar vortices that under certain conditions formed a tripole. As in [79], no further explanation was given of what these conditions might be. By studying the characteristics of this tripole, they found that the core vorticity ω_{core} depended linearly on the streamfunction ψ, in contrast to the relationship between the satellites' vorticity and ψ, which was non-linear. The structure, rotation and vorticity distribution of this tripole were similar to those observed in rotating fluid, indicating that tripolar structures are governed by the same dynamics.

In a later paper, Flor and van Heijst [91] gave more details of the evolution of the tripoles generated in stratified fluid. In this experiment a third mechanism, the tangential-injection of fluid, was used for generating vorticity beside the rotating sphere and the bent rod. As noticed in [90], the stirring rod generated highly unstable vortices that instantly transformed into asymmetric tripoles with strong satellites. These structures either split into two dipoles travelling in opposite directions as reported in the literature, or formed higher order vortices. In a few experiments, the rod generated symmetrical tripoles that appeared to be more stable and longer lived than the asymmetric ones before decaying, as the authors predicted, to monopoles. However, the tangential-injection method initially created less turbulence that gradually evolved into asymmetric tripoles with weak satellites. During their evolution the cores expanded horizontally and the satellites rapidly lost their intensity and transformed into vortex filaments. Then the cores started to assume a circular shape, which Flor and van Heijst explained as the result of internal waves, decaying the structures into monopoles.

4.2.3 Studies on large-scale tripoles

The generation of large-scale tripoles in planetary atmospheres and oceans was numerically investigated by Hesthaven et al. [92] who simulated the evolution of monopolar vortices on the β-plane. This plane is useful for the study of equatorial and mid-latitude flow. They found that this process depended directly on the initial monopole intensity. A weak vortex held its latitudinal position, decayed linearly due to Rossby waves and

the flow field remained symmetric. However, the evolution of a strong vortex was nonlinear with the core moving longitudinally and the flow becoming asymmetric. During its displacement, the core changed from circular to elliptical and two satellites appeared at its periphery, forming a tripolar structure. Hesthaven et al. conjectured that the emergence of tripoles on the β-plane might be due to the instabilities of the strong monopoles, which is also the reason for the formation of tripoles on the f-plane. However, on the β-plane the satellites oscillated around the vortex core and rotated separately, not with the core as one solid body as observed on the f-plane. The authors concluded that this oscillation and rotation might play an essential role in the mixing of the flow and the exchange of material between the vortex core and its surroundings, which could lead to the emergence of coherent structures.

The previous study was soon followed by the experimental and numerical investigations of Velasco-Fuentes et al. [93] on tripole dynamics under the influence of the parabolic free surface of a rotating fluid. This surface is analogous to the γ-plane that is used for modelling vorticity distributions close to the pole of a rotating planet, with the centre of rotation of the fluid corresponding to the pole. On this plane, the Coriolis parameter has a quadratic variation with latitude. The γ-plane is used for mesoscale oceanic flow simulations in the vicinity of the North or South poles of the Earth, because at the poles β is zero so that the quadratic variation of f is the dominant gradient. Experimentally, an isolated monopole was generated by stirring fluid cyclonically in a bottomless cylinder placed off-axis. When the cylinder was removed, the vortex became unstable and evolved into a symmetrical tripole that rotated as a solid body. This mechanism was similar to the behaviour of shielded monopoles in previous studies. However, in this case, the dynamics of the tripolar structure were completely different. Due to the initial position of the vortex off the axis of rotation, the angular velocities of the satellites were not equal, which caused them to squeeze and stretch as they rotated around the core. This meant that shortly after its formation, the tripole lost its symmetry and the central core paired with one satellite and moved away, creating a dipole-monopole state. Then during the rotation, the core oscillated, each time leaving its partner to pair with the other vortex while the whole structure moved westward and the asymmetry increased. This behaviour strongly stirred the fluid surrounding the vortex core and added some mass to the tripole. Numerical simulations of a point vortex tripole showed similar time dependent evolution and behaviour. The model predicted the vortex trajectory and fluid advection well, but failed to show an increase in the asymmetry amplitude.

The studies of Hesthaven et al. [92] and Velasco-Fuentes et al. [93] clearly show that large-scale tripoles, though they exist, are not very stable, which might explain why they have not been frequently observed in natural flows.

4.2.4 Tripoles emerging from perturbed unshielded monopoles

To study axisymmetrisation at large Reynolds numbers, Rossi et al. [94] conducted a nonlinear simulation of two-dimensional incompressible flow using the viscous vortex method based on core spreading and splitting or merging as described by Rossi [54]. In

contrast with previous work, the subject of their study was not a shielded vortex but a Lamb monopole, which is an exact solution of the Navier-Stokes equations, perturbed by a quadrupolar vorticity disturbance with an amplitude δ relative to the strength Γ of the main vortex. The numerical experiments were performed for δ=0.02, 0.1 and 0.25 at Re=10^4, then in a range of Reynolds numbers between 10^3 and 10^4 for δ=0.25. They found that the Lamb-Oseen vortex does not always return to the symmetric base state, contradicting what was suggested previously in literature. In fact, they observed two kinds of attractors for the relaxing vortex, a monopole and a tripole, depending on the magnitude of the perturbation. For small δ (0.02 and 0.1) the perturbed Lamb monopole relaxed to an axisymmetric state, but for larger δ it relaxed to a quasi-steady rotating tripole after a period of reorganisation, which proved to be stable under small disturbances. These results led Rossi et al. to believe that there is a critical perturbation amplitude (δ_{critical}) that separates the two end-states, but unfortunately they did not run more simulations with different Reynolds numbers to investigate this issue.

Later on, Le Dizès [95] analysed non-axisymmetric vortices in incompressible large Reynolds number flows using asymptotic methods, and assumed that the threshold perturbation amplitude would increase when Reynolds number decreased. No results were shown to support this claim. On the other hand, while studying the decay of the tripole, Rossi et al. [94] were disappointed to not observe quick shear-diffusion mixing in the vortex. However, by plotting the ratio of minimum to maximum vorticity $|\min(\omega)/\max(\omega)|$ with respect to the viscous time t/Re for δ=0.25 and different Reynolds numbers they concluded that the tripoles relaxed slowly on a viscous timescale, since the decay seemed to scale well with t/Re. However, Barba et al. [37] who studied the same perturbed vortex using a radial basis function (RBF) interpolation disagreed with this conclusion for the lowest Reynolds number. Their results showed a slower decay for Re=10^3, which was explained by the fact that RBF provided better accuracy than Rossi's method, which increased numerical diffusion due to the frequent splitting and merging action.

The latest paper to appear on this subject is by Barba and Leonard [96]. They performed over 50 simulations of the Gaussian monopole with a quadrupolar perturbation as described by Rossi et al. [94] for various Reynolds numbers and disturbance amplitudes δ. Their study was mainly motivated by the understanding of the axisymmetrization process of this vortex and the need to find the critical amplitudes that separate the monopolar and tripolar asymptotic states. The simulations were done using the grid-free two-dimensional viscous vortex blob method with RBF interpolation developed by Barba et al. [37]. By plotting the logarithm of vorticity in gray scale, Barba and Leonard were able to clearly observe the formation of satellites and describe in detail the evolution process of the perturbed vortex. They noted that for small perturbations the initial negative vortices were embraced by the main core and became homogenized leading to an axisymmetric monopole. However, for large amplitudes, the zero contour levels of vorticity enclosed some negative vorticity during their rotation and created two satellites around the main core. The size and life time of these satellites increased with δ. This mechanism, which was described by the authors as the "pinching" of the zero contour levels, clearly showed that there is indeed a critical perturbation that sep-

arates an axisymmetric state from a non-axisymmetric one. But since some amplitudes led to extremely weak satellites that vanished in a very short time, the two researchers were left with the problematic question of how to identify a tripole, thereby determining the threshold amplitude. They considered three different conditions to describe a tripole and found the critical amplitudes for each of them. The conditions were: the formation of satellites and the survival of the satellites for half a turnover time and for a full-turnover time. For all cases their results confirmed Le Dizès' [95] assumption that δ_{critical} increases when Re decreases. Moreover they observed that for Re between 10^3 and 10^4 the threshold varied approximately on an $\text{Re}^{-1/3}$ scale. While investigating the relaxation of the tripoles they noted that this process occurred on a viscous timescale (t/Re) for large amplitudes and on a shear-diffusion timescale ($t/\text{Re}^{1/3}$) for small ones. They justified this by the fact that shear-diffusion is a linear mechanism and for small perturbations nonlinear effects are not very important. Finally, in order to test the stability of the tripolar structure, they randomly perturbed the particle positions and found that the vortex, once formed, is very robust and able to recover from the perturbation back to its original state. This result agreed with the findings of Rossi et al. [94].

4.3 High-order multipolar vortices

Since the observation of the tripole, natural human curiosity pushed researchers to look for higher-order vortices that can be considered coherent structures. Numerical and experimental evidence showed that more complex vortices than the tripole do actually exist in two-dimensional flow. They can have different orders of multipole, where in each case the centre has an n-polygonal shape of one vortical sign surrounded by n satellites of opposite sign, one on each side. These multipoles for simplicity are called by the geometrical form of their cores, so they are triangular, square, pentagonal, etc. Usually their lifespan is shorter than that of the tripole due to their instability. Figure 4.6 depicts schematically the first three members of this family.

4.3.1 Experimental studies on high-order multipoles

A vortex generated in a flow where there is a density gradient along surfaces of constant pressure is called baroclinic. A triangular-like structure arising from an unstable baroclinic vortex in a two-layer rotating stratified fluid was observed by Griffiths and Linden [97]. During the experiment a monopole was created in a rotating tank, which resulted in the formation of an anticyclonic vortex in the upper layer and a cyclonic in the lower one, but the authors focussed their study on the evolution of the anticyclone only. The stability and strength of both vortices depended on the Richardson number (Ri), which is a dimensionless parameter that expresses the ratio of potential to kinetic energy, defined as $\text{Ri}=g'h_0/4\Omega^2R_0^2$, where $g'=g\Delta\rho/\rho$ is the reduced gravity between the two layers, $\Delta\rho$ is the density difference, h_0 the initial depth of the upper fluid, Ω the environmental rotation rate and R_0 the initial monopole radius. For large Ri the upper

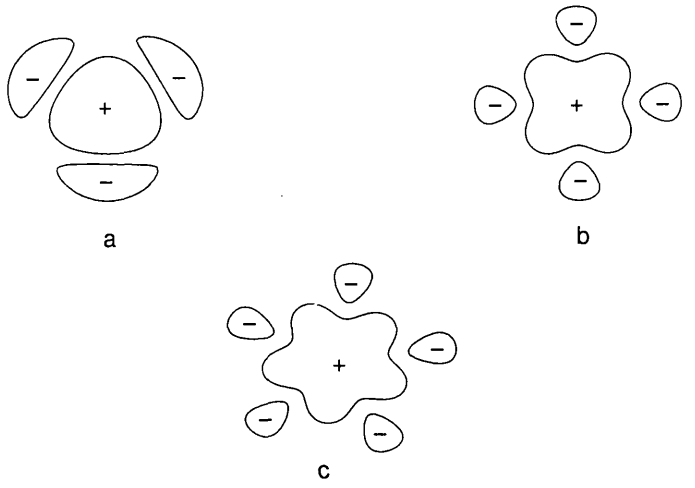

Figure 4.6: High-order multipolar vortices; a: triangular vortex; b: square vortex; c: pentagonal vortex.

vortex split into two dipoles due to a wavenumber-2 instability. However, for small Ri the three-dimensional instabilities led to the growth of a mode-3 perturbation, which created a triangular-like structure. The cyclonic vorticity around the anticyclonic core drew some fluid from the centre and formed three enclosed areas that exerted a shear on the main vortex, making it triangular, then pinched three patches of vorticity, creating three dipoles that travelled away from the centre. Later on, a numerical simulation of the Navier-Stokes equations by Verzicco et al. [98] for the same initial conditions produced results consistent with the observations of Griffiths and Linden.

Triangular vortices have been found to emerge from different initial conditions, in particular from unstable anticyclonic shielded vortices. Kloosterziel and van Heijst [84] were able to create such a vortex in the laboratory by stirring the fluid in a bottomless cylinder placed in the centre of a rotating tank filled with a homogeneous fluid. In most cases wavenumber-2 perturbations grew and the anticyclone split into two cyclonic vortices that moved away from the tank centre. The new vortices were unstable and quickly broke down into two counter-rotating dipoles. But in one experiment with a small Rossby number, which is a dimensionless parameter that expresses the ratio of net circulation in a fluid to the Coriolis acceleration arising from planetary rotation, $\mathrm{Ro} = U/Lf$, where L and U are respectively the characteristic length scale and velocity, wavenumber-3 perturbations grew, leading to the formation of a triangular shaped anticyclonic core surrounded by three cyclonic satellites. This structure had a solid body rotation in the same direction as the central vortex, and strangely enough, the maximum core vorticity had the same order of magnitude as the peak vorticity of the satellites. The authors stated that it was the first paper in the literature to report a triangular vortex. Soon after its formation, two of the satellites collapsed and the

core became elliptic, turning the triangular structure into an unstable tripole that did not live long before splitting into two dipoles. When trying to repeat the experiment, Kloosterziel and van Heijst found great difficulty in getting the same initial conditions as before, thus only rarely were they able to observe the emergence of a triangular vortex. Moreover, they could not create this structure from cyclonic shielded monopoles. They concluded that the instability and the scarcity of this new vortex might be the reasons why it had not been observed in the past. Studying the reasons that led to the evolution of such a structure, they noted that three-dimensional centrifugal instability may have played a role, since it was previously found that two dimensional cyclones and anticyclones behave similarly [75]. Moreover, the Rossby number was critical in this case, since triangular vortices emerged only from initial shielded monopoles with small Rossby number.

Carnevale and Kloosterziel [99] gave more experimental evidence that a triangular vortex can be the end-state of an unstable anticyclonic shielded monopole using the same technique as in the previous study. This triangular structure, as in [84], was unstable and broke up into a pair of dipoles after the merger of two satellites. They tried unsuccessfully to produce a stable triangle that decays due to viscous effects while conserving its form, by introducing three equally spaced separators in the cylinder. This experiment resulted in the creation of a more symmetric vortex with a triangular core and three semi-circular satellites that survived longer than the previous structure before breaking down. They stated also without giving graphical evidence that in some cases the core of the triangular vortex did not split up, but paired with the satellite formed after the merging, leading to a dipole-monopole end state.

This scenario is reported by Beckers and van Heijst [100] who also produced a triangular vortex from an anticyclonic isolated monopole. In the early stages, their vortex evolution was similar to that of other experimental vortices reported in the literature. However, after the merging of two satellites a tripole was formed, then the core paired with the resultant vortex and moved away from the other satellite, creating a dipole-monopole situation. This result was similar to the evolution of the tripole on the γ-plane [93]. The evolution and break up of this triangular vortex was well reproduced in a point vortex simulation, which showed that the asymmetric strength of the satellites is behind this special disintegration. Reproducing another triangular structure that behaved in the same way was not an easy task, and the authors clearly stated that they were unable to do so in further experiments.

In 1993, in a brief remark, Flor et al. [90] reported the formation of a vortical structure with a triangular shaped core in a non-rotating stratified fluid. Though it was the first time that a tripole had been observed in such a flow, no further information was given until 1996 when Flor and van Heijst [91] published an extended article on this subject. As mentioned in §4.2, stirring stratified fluid with a rotating bent rod created asymmetric tripoles with strong satellites. In some cases this vortex broke into two dipoles, but in others the core was squeezed by the strong satellites and took on a triangular shape, decreasing the angle between the side vortices at one end of it. Then, during the rotation, one of the satellites stretched around the centre and broke into two equal strength vortices such that one of them moved to the free side of the triangu-

lar core creating a new structure. This formation was stable and survived for several revolutions, leading the authors to predict its gradual decay to a monopole. In other experiments with the tangential-injection method, wavenumber-3 perturbations grew instantly in the flow, leading directly to the formation of a triangular vortex without passing through a tripolar transient phase. In contrast to the previous case, this vortex was highly unstable and decayed rapidly either to a monopole or to a tripole through a process similar to that of triangles in rotating fluid. While studying the characteristics of the stable triangular vortex, the authors found that it had a continuous vorticity distribution like other coherent structures, but rotated more slowly than the tripole. Moreover, the vorticity and the streamfunction in this vortex were linearly related in contradiction to previous results [86, 89, 99, 101]. Representing the centre by a 3γ strength point vortex and the satellites by 3 point vortices of strength $-\gamma$ each, placed on a circle and spaced equally by $2\pi/3$, this structure was modelled numerically. The simulation predicted well the motion and the angular velocity of the experimental vortex.

4.3.2 Numerical simulations of multipolar vortices

Triangular vortices, or quadrupoles as described by Carton [89], were in some special cases the result of the interaction of two equal co-rotating isolated monopoles. They found numerically that when the initial shielded vortices had wide cores with narrow, large vorticity amplitude, annuli, and were situated close to each other, they evolved into two short-lived quadrupoles. This transient structure broke into two dipoles or a finite number of monopoles. In the same article, Carton gave evidence of a long-lived triangular vortex. He stated that a 2-contour shielded monopole with a strong perturbation generated a stable quadrupole that performed several rotations with few structural changes due to dissipation. This was the first time that such a vortex had been reported.

Since the triangular vortices observed in the laboratory were very unstable and short lived, their evolution was not well understood. So Orlandi and van Heijst [86] decided to simulate such vortices, hoping to get a deeper insight into their dynamics. They were successful in generating a triangular structure from a two-dimensional cyclonic shielded monopole with a very steep vorticity profile. It is interesting to remember that in three-dimensional flow only anticyclonic vortices generate such a structure. However, like the experimental ones, this triangular vortex was highly unstable and two satellites quickly merged before it broke up into two dipoles. Studying the vorticity-streamfunction graph for their vortex, the authors noticed a striking relation; in the core, close to the maximum vorticity, ω and ψ were not related at all: $\partial\omega/\partial\psi=0$.

Another numerical investigation of the stability of high-order multipoles was performed by Carnevale and Kloosterziel [99] using high-resolution simulation and a point vortex model. First, they randomly perturbed an isolated monopole with a disturbance ξ' concentrated at the zero vorticity level between the core and annulus. Different behaviours of the vortex were observed depending on ξ'. In some simulations with

a very steep initial vorticity distribution the vortex evolved into a triangle, a similar result to that of Orlandi and van Heijst [86]. They suggested that the different evolutions are accounted for by the mix of different wavenumber growth in the perturbations. This appears to be a plausible explanation since in one case where modes other than mode-3 were weak, to the surprise of the authors, a stable symmetric triangular structure emerged and conserved its form for many rotations. The ω-ψ scatter plot for this vortex resembled that of [86], especially in the centre of the core ($\partial\omega/\partial\psi$=0), but the authors did not mention it.

This stable triangle motivated them to examine the possibility of such a vortex appearing in the laboratory. They performed a series of simulations with pure wavenumber-3 instability and different viscosities, and found that viscosity does not affect the stability of the structure, thus it is possible to produce experimentally a stable triangle that decays due to viscous effects only. However, further stability studies on the vortex showed that this is very unlikely because the triangle is unstable to infinitesimally small perturbations, which explains why it always breaks down during the experiment. Increasing the steepness of the vorticity profile in the initial shielded monopole led to the breaking of the outer ring into four satellites and the emergence of a new structure with a square core. This vortex, the square, was unstable and soon after its formation each pair of its satellites merged leading to a tripole, then broke to the familiar pair of dipoles.

Carnevale and Kloosterziel [99] conducted further simulations with pure mode-4 instability, which indicated that a square vortex can be observed in a laboratory, but it will not be stable and it will appear as a transitory phase since the smallest numerical noise is sufficient to destroy it. A square vortex has been produced in the laboratory in non-rotating stratified fluid by imposing mode-4 perturbations (van Heijst, private communication). Photographs can be seen on the website of the Fluid Dynamics Laboratory at Eindhoven University of Technology [102]. As predicted by the simulations, the vortex was unstable and shortly after its formation evolved into a tripole. Moreover, Carnevale and Kloosterziel briefly mentioned that they were able to create a pentagonal vortex through a wavenumber-5 perturbation that lived only for a very short period. Two pairs of its satellites merged, forming a triangular vortex that broke into a tripole before the final two-dipole state. Using a point vortex model to assess the stability of the multipoles, they remarked that it was easier to make a structure unstable once its satellites were not of equal strength. Finally they concluded that of the high-order multipoles they examined, only the triangle was stable enough to be considered a coherent structure beside the monopole, dipole and tripole, though due to its marginal stability it is the weakest member in this family.

An extensive study of the formation of multipolar vortices from shielded monopoles with piecewise-constant vorticity profile and their decay was carried out by Morel and Carton [101]. However, contrary to previous investigations, they used three-contour Rankine vortices as the initial condition. A Rankine vortex, named after its Scottish creator William John Rankine, is an idealized vortex with uniform vorticity inside a

circular patch of radius R and zero vorticity outside it. It is defined as:

$$\omega = \begin{cases} \omega_0, & r \leq R \\ 0, & r > R. \end{cases} \tag{4.1}$$

A three-contour vortex is formed by three areas of vorticity, a positive core separated from a negative ring by a wide annulus of zero vorticity. Morel and Carton argued that this annulus facilitated the formation of complex multipoles since the ring reorganised more easily into separate satellites, uninfluenced by the core shear. Depending on the wavenumber introduced, they were able to get quadrupoles, squares — referred to as pentapoles — and pentagonal vortices. Interestingly, they observed that for a mode less than 5 only one wavenumber instability grew on a given three-contour Rankine vortex, unlike the competition of perturbations suggested by Carnevale and Kloosterziel [99] for the two-contour monopoles. The nonlinear evolution of the initial condition was simulated with contour surgery and a pseudospectral code for modes 2, 3 and 4. It was observed that the lower the wavenumber the higher the linear instability, which meant that mode-4 perturbations developed more slowly than mode-2, giving ample time for nonlinear effects to produce more complex multipoles. The evolution process started by the condensation of the ring into n satellites, slightly changing the form of the core and leaving some filaments that folded around the side vortices and dissipated due to viscosity before the structure stabilized into its final shape. These multipoles were similar to the multipolar steady states of the Euler equations. The pseudospectral simulation for the triangle revealed that its circulation, angular momentum and energy were conserved during its formation, but its enstrophy decreased validating the hypothesis of Leith [74] that multipoles have lower enstrophy than monopoles. Enstrophy, a term made popular by Leith himself, is the integral of the square of vorticity over the velocity field and is conserved in two-dimensional inviscid flow. It is defined as:

$$E = \frac{1}{2} \int_S \omega^2 \mathrm{d}S, \tag{4.2}$$

Finally, the vortex had a nonlinear relation between ω and ψ in accordance with [86, 89, 99].

In order to examine the robustness of the multipolar family under slight disturbances or permanent deformations, Morel and Carton [101] carried out a stability study on each of its members. The tripole and the triangle were both found to be stable. However, higher order structures broke down through the known mechanisms of satellite merger, core destruction into two dipoles or core pairing with one satellite. The result of the breakdown was found to depend on the size of the core and its distance from the satellites. When the centre was small and distant from its side vortices, it was strong enough to resist the shear exerted by them, which led to a tripole or even sometimes a quadrupole due to the successive satellite mergers. Conversely, a large core close to its side vortices resulted in two dipoles. Though in this investigation the multipoles emerged from three-contour Rankine vortices, the stability results agreed with the conclusion of [99] that for high order structures only triangles are strong enough to be considered coherent vortices. Finally, the authors summarised in one figure [101, Figure 14] the evolution and decay of the different vortex types.

4.3.3 Large scale triangular vortices

Lin [103] found through fully nonlinear contour dynamics simulations that triangular vortices might exist in nature as the result of the evolution of tornado-like vortices. Based on previous studies, he divided the tornado into two regions, inner and outer, and argued that these areas are independent of each other so their evolutions can be studied separately. The outer region was represented by a shielded monopole that produced a tripolar vortex. However, the vorticity field of the inner area was approximated by a three-layer model, which consisted of a weak central ring, a middle strong annulus and a moderate outer layer all with positive vorticity. The vortex was unstable to an azimuthal wavenumber-3 perturbation, which destroyed the strongest layer and turned it into three vortices that the author called "suction vortices" due to their effect on the central layer. These satellites enrolled some vorticity from the core deforming it to triangular while keeping the outer annulus intact. This triangle differs from what has been previously reported by the fact that its core and its satellites are both cyclonic, which Lin believed to be the case in real tornadoes.

4.3.4 Multipoles emerging from perturbed unshielded monopoles

Lately, multipoles have been observed to emerge from perturbed Lamb vortices. Barba [104] superimposed non-axisymmetric distortions on a Gaussian distribution and analysed the axisymmetrisation processes. When subjected to a weak three-fold perturbation, the Lamb vortex relaxed directly to its base state, while a strong distortion led to the formation of a triangular vortex that rotated as a solid body. It was the first time that such a vortex had been produced from unshielded monopoles. As for the tripolar case in a previous study [96], the satellites were formed by the negative part of the disturbance while the positive part was embedded in the core. Under a stability test, the triangle proved to be a stable structure. In further simulations, an octopole perturbation produced a square vortex, and a decapolar one formed a pentagonal vortex. Both structures were unstable and evolved into tripoles through satellite merger. As for the tripole, Barba suggested the existence of a threshold perturbation value (δ_{critical}) that separates the axisymmetrisation of the perturbed vortex from the emergence of high-order multipole states.

Chapter 5

Numerical methodology

The obvious is that which is never seen until someone expresses it simply.

Sand and Foam, Khalil Gibran, 1926

A novel approach for the calculation of velocities in two-dimensional Lagrangian vortex methods is presented in this chapter. The computation scheme can be applied to simulate inviscid and viscous flows. The method solves the partial differential equation of the streamfunction directly on the node, using a standard linear solver for large sparse symmetric systems. The solution proceeds in an iterative manner until specified convergence criteria are met.

To develop the current numerical method, the computational domain is represented by a set of points connected by a Delaunay triangulation. At every node i in the domain the streamfunction ψ and its derivatives are approximated by a Taylor series truncated after the second order terms, since the derivatives in Equation (2.15) are second order. Then the streamfunction and velocities are computed directly at the nodes using a least squares method based on the three requirements of a valid solution to the partial differential equation for the system: a continuous solution between the nodes, the equation at nodes must be satisfied and the boundary conditions must be met. The first requirement is fulfilled through the approximation of ψ by the truncated Taylor series at each node, while making sure that the expansion at any given point matches that at nearby points to a pre-selected order. The second requirement is fulfilled through a relationship between the coefficients of the series at each node, and the third is imposed by fixing the streamfunction and velocities at the boundaries, depending on the conditions.

This method is not limited by the number of points in the computational domain nor by their fixed locations, allowing the addition, deletion and movement of points with no change in the numerical formulation.

5.1 Numerical formulation for plane flow

To approximate the streamfunction at a computational element (x_i, y_i), n points must be chosen as its neighbours where the second order Taylor series is applied. This guar-

antees the continuity of the solution of the streamfunction between the nodes. The mesh generation and choice of neighbours are explained in §5.3 and §5.4. Considering a node i interacting with a neighbour node j, the local approximation of the streamfunction is:

$$\psi^{(j)} \cong \psi^{(i)} + x_{ij}\psi_x^{(i)} + y_{ij}\psi_y^{(i)} + \frac{1}{2}x_{ij}^2\psi_{xx}^{(i)} + y_{ij}x_{ij}\psi_{xy}^{(i)} + \frac{1}{2}y_{ij}^2\psi_{yy}^{(i)}, \tag{5.1}$$

where $x_{ij} = x_j - x_i$ and $y_{ij} = y_j - y_i$. Differentiating Equation (5.1), with respect to x and y, one gets the truncated Taylor series approximation of the velocities:

$$\psi_x^{(j)} \cong \psi_x^{(i)} + x_{ij}\psi_{xx}^{(i)} + y_{ij}\psi_{xy}^{(i)}, \tag{5.2a}$$

$$\psi_y^{(j)} \cong \psi_y^{(i)} + x_{ij}\psi_{xy}^{(i)} + y_{ij}\psi_{yy}^{(i)}. \tag{5.2b}$$

Then, to satisfy the partial differential equation at the node i, the Poisson equation (2.15) is applied:

$$\psi_{xx}^{(i)} + \psi_{yy}^{(i)} = -\omega_i. \tag{5.3}$$

Once Equation (5.3) and the second order Taylor series (5.1) are expanded for all the nodes $i = 1, 2, 3, \ldots, N$ and their neighbours in the computational domain, the following linear system is produced:

$$\mathrm{A}_{ij}\boldsymbol{\Psi}_i = \psi^{(j)}, \tag{5.4a}$$

$$\mathrm{D}_i\boldsymbol{\Psi}_i = -\omega_i, \tag{5.4b}$$

where the left-hand side matrices contain the solution $\boldsymbol{\Psi}_i$ and its coefficients, and are written as the following vectors:

$$\boldsymbol{\Psi}_i = [\psi^{(i)}\ \psi_x^{(i)}\ \psi_y^{(i)}\ \psi_{xx}^{(i)}\ \psi_{xy}^{(i)}\ \psi_{yy}^{(i)}]^T, \tag{5.5a}$$

$$\mathrm{A}_{ij} = [1\ x_{ij}\ y_{ij}\ x_{ij}^2/2\ x_{ij}y_{ij}\ y_{ij}^2/2], \tag{5.5b}$$

$$\mathrm{D}_i = [0\ 0\ 0\ 1\ 0\ 1]. \tag{5.5c}$$

When Equations (5.4) are applied to two nodes neighbouring each other, the system to solve becomes:

$$\mathrm{A}_{ij}\boldsymbol{\Psi}_i + \mathrm{B}_{ji}\boldsymbol{\Psi}_j = 0, \tag{5.6a}$$

$$\mathrm{B}_{ij}\boldsymbol{\Psi}_i + \mathrm{A}_{ji}\boldsymbol{\Psi}_j = 0, \tag{5.6b}$$

$$\mathrm{D}_i\boldsymbol{\Psi}_i = -\omega_i, \tag{5.6c}$$

$$\mathrm{D}_j\boldsymbol{\Psi}_j = -\omega_j, \tag{5.6d}$$

where $\mathrm{D}_j = \mathrm{D}_i$ and $\mathrm{B}_{ij} = \mathrm{B}_{ji} = [-1\ 0\ 0\ 0\ 0\ 0]$. In order to compute the components of the streamfunction, Equations (5.4) are combined:

$$\mathrm{T}_{ij}\boldsymbol{\Psi}_i + \mathrm{B}_{ji}\boldsymbol{\Psi}_j = b_{ij}, \tag{5.7}$$

where the definition of matrix T_{ij} takes into consideration the position of node i if it is on the boundary or not and b_{ij} contains the nodal vorticities or any boundary condition to be applied. When i is not a boundary node, T_{ij} and b_{ij} are defined:

$$\mathrm{T}_{ij} = \begin{cases} \mathrm{A}_{ij} - \frac{x_{ij}^2}{2}\mathrm{D}_i, & \text{j even;} \\ \mathrm{A}_{ij} - \frac{y_{ij}^2}{2}\mathrm{D}_i, & \text{j odd,} \end{cases} \tag{5.8}$$

and

$$b_{ij} = \begin{cases} \frac{x_{ij}^2}{2}\omega_i, & \text{j even} \\ \frac{y_{ij}^2}{2}\omega_i, & \text{j odd} \end{cases} \tag{5.9}$$

T_{ij} alternates between the two forms to avoid having a row of zeros in the left-hand side matrix. On the other hand, if node i is a boundary node then its vorticity is part of the solution, thus the differential operator is not included in the system and the definitions of T_{ij} and b_{ij} are modified to apply the boundary conditions by setting the values of the streamfunction or the velocities. For a streamfunction boundary condition, T_{ij} and b_{ij} are:

$$\mathrm{T}_{ij} = \mathrm{A}_{ij} - [1\ 0\ 0\ 0\ 0\ 0], \tag{5.10}$$

$$b_{ij} = -\psi. \tag{5.11}$$

For a velocity boundary condition, the same approach is used to define the matrices:

$$\mathrm{T}_{ij} = \mathrm{A}_{ij} - [0\ x_{ij}\ y_{ij}\ 0\ 0\ 0], \tag{5.12}$$

$$b_{ij} = -x_{ij}\psi_x - y_{ij}\psi_y, \tag{5.13}$$

where ψ_x and ψ_y are defined using respectively the vertical and horizontal components of the velocity on the boundary.

5.2 Least-squares solution

Since the solution $\mathbf{\Psi}_i$ has six components, at least six neighbours must be chosen per node. Otherwise the system will be underdetermined and will have an infinite number of solutions. From the standpoint of accuracy and smoothness of the approximation of the streamfunction between the elements, it is preferable to include more neighbours than the number of unknown components. This will lead to an overdetermined system of equations that is solved in a least-square sense by minimising a defined local error. It is important to note that the accuracy of the least-squares method greatly depends on the order of the Taylor series. Strickland [105] investigated the accuracy of the least-squares method for different orders of the Taylor series, and found that a third order

series reduces the error by about two orders of magnitude from that of a second order series, while a fourth order Taylor series decreases the error by an extra two orders.

In the current study, Equation (5.7) is solved simultaneously for all the nodes. After choosing the n ($n > 6$) neighbours per node, an error ε_i is defined:

$$\varepsilon_i^2 = \sum_{j=1}^{n} (\mathrm{T}_{ij}\boldsymbol{\Psi}_i + \mathrm{B}_{ij}\boldsymbol{\Psi}_j - b_{ij})^2, \tag{5.14}$$

where subscript j refers to neighbouring nodes. If required in the calculations, Equation (5.14) can be multiplied by a weighting coefficient w_{ij} that depends on the distance between the nodes and defined as:

$$\mathrm{w}_{ij} = e^{-(x_{ij}^2 + y_{ij}^2)/\varsigma^2}, \tag{5.15}$$

where ς is the length scale depending on the local mesh geometry and defined either as the arithmetic or the geometric mean of the edge lengths connected to node i.

The least-squares solution for $\boldsymbol{\Psi}$ is found when the local residual ε_i^2 is a minimum, thus its derivatives with respect to each term in Equation (5.5a) are zero. Differentiating ε_i^2 with respect to $\psi^{(i)}$, $\psi_x^{(i)}$ and $\psi_y^{(i)}$:

$$\frac{\partial \varepsilon_i^2}{\partial \psi^{(i)}} = \sum_{j=1}^{n} 2\mathrm{w}_{ij}(\mathrm{T}_{ij}\boldsymbol{\Psi}_i + \mathrm{B}_{ij}\boldsymbol{\Psi}_j - b_{ij}), \tag{5.16a}$$

$$\frac{\partial \varepsilon_i^2}{\partial \psi_x^{(i)}} = \sum_{j=1}^{n} 2x_{ij}\mathrm{w}_{ij}(\mathrm{T}_{ij}\boldsymbol{\Psi}_i + \mathrm{B}_{ij}\boldsymbol{\Psi}_j - b_{ij}), \tag{5.16b}$$

$$\frac{\partial \varepsilon_i^2}{\partial \psi_y^{(i)}} = \sum_{j=1}^{n} 2y_{ij}\mathrm{w}_{ij}(\mathrm{T}_{ij}\boldsymbol{\Psi}_i + \mathrm{B}_{ij}\boldsymbol{\Psi}_j - b_{ij}). \tag{5.16c}$$

Once the error ε_i^2 is differentiated with respect to all terms and the derivatives are set to zero, the system to solve becomes:

$$\left(\sum_{j=1}^{n} \mathrm{T}_{ij}^T\mathrm{T}_{ij}\right)\boldsymbol{\Psi}_i + \sum_{j=1}^{n} \mathrm{T}_{ij}^T\mathrm{B}_{ij}\boldsymbol{\Psi}_j = \sum_{j=1}^{n} \mathrm{T}_{ij}^T b_{ij}, \tag{5.17}$$

where $\mathrm{T}_{ij}^T\mathrm{T}_{ij}$ and $\mathrm{T}_{ij}^T\mathrm{B}_{ij}$ are 6×6 blocks. Once Equation (5.17) is assembled for all N nodes in the computational domain the following system is produced:

$$\begin{pmatrix} \vdots & \vdots & \vdots & \vdots & \vdots \\ \cdots & \mathrm{T}_{ij}^T\mathrm{T}_{ij} & \cdots & \mathrm{T}_{ij}^T\mathrm{B}_{ij} & \cdots \\ \vdots & \vdots & \vdots & \vdots & \vdots \\ \cdots & \mathrm{T}_{ji}^T\mathrm{B}_{ji} & \cdots & \mathrm{T}_{ji}^T\mathrm{T}_{ji} & \cdots \\ \vdots & \vdots & \vdots & \vdots & \vdots \end{pmatrix} \begin{pmatrix} \vdots \\ \boldsymbol{\Psi}_i \\ \vdots \\ \boldsymbol{\Psi}_j \\ \vdots \end{pmatrix} = \begin{pmatrix} \vdots \\ \mathrm{T}_{ij}^T b_{ij} \\ \vdots \\ \mathrm{T}_{ji}^T b_{ji} \\ \vdots \end{pmatrix}. \tag{5.18}$$

The left-hand side matrix is a large, sparse, symmetric matrix with total size of $6N \times 6N$, where for example block $\mathrm{T}_{ij}^T\mathrm{T}_{ij}$ is located in row $6i+1$ to $6i+6$ and column $6i+1$ to $6i+6$ and block $\mathrm{T}_{ji}^T\mathrm{T}_{ji}$ is in rows $6j+1$—$6j+6$ and columns $6j+1$—$6j+6$.

After assembling the system of equations, the boundary conditions are imposed by modifying the rows of the streamfunction components in the left-hand side and right-hand side matrices corresponding to the boundary nodes. They are set to zero and replaced by equations depending on the condition imposed. For a velocity boundary condition, the equations are:

$$[0\ 1\ 0\ 0\ 0\ 0]\mathbf{\Psi}_i = -v, \tag{5.19a}$$

$$[0\ 0\ 1\ 0\ 0\ 0]\mathbf{\Psi}_i = u, \tag{5.19b}$$

where u and v are the components of the prescribed velocity on the boundary, while for a streamfunction condition the rows of the streamfunction at the boundary nodes are replaced by:

$$[1\ 0\ 0\ 0\ 0\ 0]\mathbf{\Psi}_i = \psi. \tag{5.20}$$

The assembly of the system can be summarised by the following algorithm:

ALGORITHM 4.1

for each node $i = 0, 1, \ldots, N-1$ **do**
  for each neighbour node $j = 0, 1, \ldots, n$ **do**
    Calculate A_{ij}.
    Assemble B_{ij}.
    if i is not a boundary node **then**
      Assemble D_i.
      Calculate T_{ij}.
      Evaluate Equation (5.7) and add to the system.
    else
      if Imposing a streamfunction boundary condition **then**
        Evaluate Equations (5.10–5.11) and add to the system.
      end if
      if Imposing a velocity boundary condition **then**
        Evaluate Equations (5.12–5.13) and add to the system.
      end if
    end if
  end for
end for
for each node $i = 0, 1, \ldots, N-1$: **do**
  if i is a boundary node **then**
    if Imposing a streamfunction boundary condition **then**
      Insert Equation (5.20).
    end if
    if Imposing a velocity boundary condition: **then**
      Insert Equations (5.19).
    end if
  end if
end for

The symmetric system of Equations (5.18) can be solved by a standard iterative technique that starts with an initial guess at the nodal points and uses a successive cycle of operations in order to obtain a more accurate solution and approximate the desired convergence criteria set by the user. In the current model, the BiConjugate Gradient Stabilized (Bi-CGSTAB) iterative method [106] is used.

5.3 Mesh generation

A critical phase in the development of new numerical models for vortex flow simulation is the choice of the vorticity approximation in the computational domain since this greatly affects the accuracy of Lagrangian vortex methods. The numerical approach developed in the previous sections is based on a triangulated vortex method, where the nodes discretising the computational domain are connected by a Delaunay triangula-

tion and the vorticity is approximated at each element. This technique has previously been used to compute planar, axisymmetric and three-dimensional flows [14–17, 60].

The initial computational domain, which can have various geometrical forms, is generated by defining its shape, its centre, its dimensions and the required number of points on the outer boundary, then meshed using a Delaunay triangulation. There exist different algorithms to produce this triangulation; in the current study a mesh generator based on the GNU Triangulated Surface Library of Popinet [107] is used to code the triangulation and generate the mesh. The functions in this library are ready to be directly used without any modifications. The user has just to define the minimum and maximum triangle areas, $A_{\min}$ and $A_{\max}$ respectively, and a tolerance between the computed and exact values of the vorticity distribution on the mesh. Then the initial domain is constructed in three phases; first, an initial triangulation is performed, then the mesh is refined by inserting points in order to meet the specified requirements for the triangles, and finally the vorticity is computed at each node and then interpolated at the centroid of each triangle and compared with the exact value. If the difference is larger than the specified tolerance, a new node is inserted at the centroid with the exact value of vorticity and the triangulation is updated. This iterative procedure is repeated until the tolerance is met on each triangle. Figure 5.1 shows a generated circular mesh for a Lamb-Oseen vortex situated at its centre after the second and third phase. Since the vortex has a high vorticity gradient in its core, the node density is higher there after the last step.

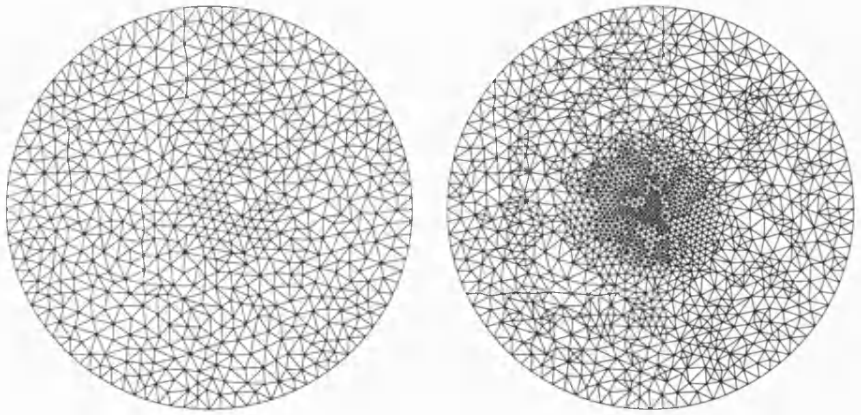

Figure 5.1: Mesh generation for a Lamb-Oseen vortex; a: initial mesh after Delaunay triangulation refinement, b: mesh after vorticity refinement.

When constructing the triangulation, the Triangulated Surface Library indexes the grid points and the edges directly without the user interference. Then, the total number of vertices, segments and triangles along with the node coordinates, their indices and their connectivity are saved. This storage is used later on for updating the mesh and retrieving information about it, for example for identifying the points connected to a

given node. Once the domain is generated, the information are sent to another code, which performs the approximation of the streamfunction, assembles the system of equations as described in Algorithm 4.1 and solves it using the Bi-CGSTAB iterative method.

For simulating flows over solid boundaries, the triangulation has to take into account the presence of the body in the computational domain. Nodes can not lie inside a closed geometry since this area is physically not part of the flow. Using an unstructured grid, as in the present study, makes the introduction of two dimensional geometries into the domain an easy task, as the mesh conforms well to any desired shape. To produce meshes around bodies, the initial mesh generator is modified by the author by using extra functions from the GNU Triangulated Surface Library. The domain is produced then as follow: an initial grid without the geometry in it is first generated, then the nodes are freed from their triangulation so the points forming the circumference of the solid body can be added to the domain by introducing their coordinates to the list previously saved. Freeing the nodes from their connections is crucial at this stage as the Triangulated Surface Library will not allow addition or deletion of points in a triangulated domain. Once the points of the solid geometry are added, all the nodes lying inside a closed area are removed. A technique similar to ray tracing is used to achieve this. From every node $i = 1, 2, \ldots, N$ a ray is projected rightwards and its intersection with the solid periphery of the body is checked. If a given ray crosses the border an odd number of times, then its corresponding node is inside the boundary, thus it is deleted. A simple example of this technique is shown in Figure 5.2. Point 1 is outside the circle, as a result its ray intersects the circumference twice, while the ray of node 2, which is inside the closed region, crosses it once. After all the points inside the body are removed, the nodes are re-triangulated, the mesh is updated and the indices of the inner boundary points are stored so they can be recovered when applying boundary conditions. Figure 5.3 shows the Delaunay triangulation for a circular cylinder and an ellipse in the computational domain.

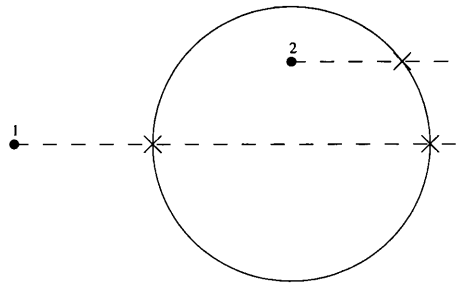

Figure 5.2: A simple example of the approach used to check if a node lies inside a closed area.

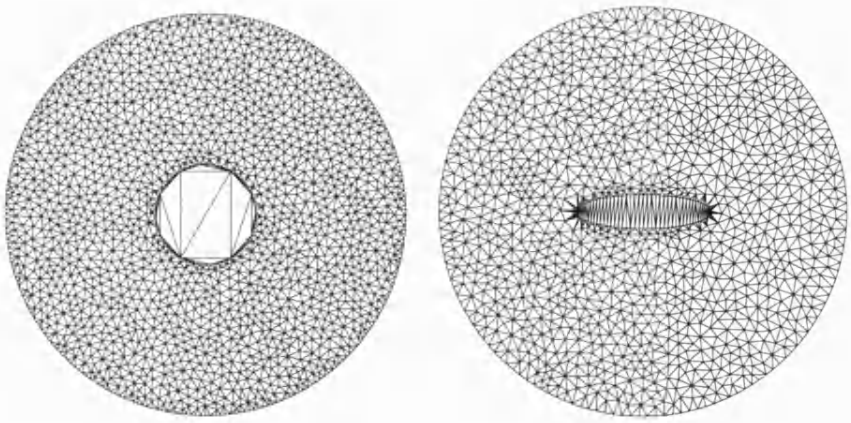

a b

Figure 5.3: Delaunay triangulation for solid bodies in the computational domain; a: mesh around a circular cylinder, b: mesh around an ellipse

5.4 Neighbourhood and connectivity

The choice of neighbours for a computational element is critical to the development of the current method since the arrangement of the neighbouring particles affects the approximation of the streamfunction and the accuracy of the least-squares method as discussed by Baty and Wolfe [108]. For instance, if the neighbours are along the same line no information is available about derivatives perpendicular to that line, or if they are all on one side of the node then the approximation of the streamfunction for the elements on the other side is missing, which can result in an ill-conditioned matrix A_{ij}. Also, the effect of a far away neighbour is less important than a close one, so for a better approximation it is desirable for the neighbours to be as close as possible to the main node.

Different techniques for selecting the neighbours of a node exist [59, 108–110] and this subject is an important area of research in triangulated vortex methods. Depending on the approach used, the process can be complicated, as in Perrone and Kao [110], computationally expensive, as in Baty and Wolfe [108] and Liszka and Orkisz [59], or fails to generate a good point distribution around the node due to the irregular density of the mesh, as in Jensen [109].

In the present method different algorithms for the selection of neighbours were tested before developing a novel procedure to accomplish this task. The developed approach enjoys several advantages over other algorithms as it is simple, time efficient and guarantees a good point distribution around the node. The Delaunay triangulation provides useful information about the vertices in the mesh connected to a given point by an edge. This information is used for every node $i = 1, 2, \ldots, N$ in the domain to identify the points directly connected to it by an edge and add them to a list. Then the code loops over all the nodes in the list adding the points connected to them. This step is repeated every time a new set of vertices is added to the list. In this way, a web

of nodes is built around every vertex i, from which the neighbours are to be selected. To minimize computing time, a cut off distance δx that depends on the mesh quality is defined around node i, after which no extra nodes are added to the web. So once a new vertex j is added to the list, its distance from i is checked. If $d(i,j) < \delta x$ then the points connected to j are added, otherwise the code does not loop over j. This step limits the number of nodes to loop over.

When simulating a flow over a solid geometry, an extra check is performed before adding nodes to the neighbour list, in order to guarantee the continuity and validity of the Taylor series expansion. Physically, two particles in the flow separated by a solid object will not affect each other, thus in the simulation they cannot be chosen as neighbours. So once a vertex is identified as a potential neighbour to node i, a straightforward approach is used to ensure that the points "see" each other: the two nodes are joined by a segment whose intersection with the body periphery is investigated. If the segment crosses the boundary, then the point can not be a neighbour to node i, as a result, it is not added to the list. The points on the boundary are part of the flow field, thus they can be neighbours to other nodes including boundary points as long as the joining segment do not fall inside the solid geometry. Figure 5.4 illustrates an example of this technique. Nodes a and b are boundary points and can be neighbours to nodes d and c respectively. However, since the segments joining a to c and b to d intersect the periphery, and the segment between a and d falls inside the closed area, these points are not accepted as neighbours to each other.

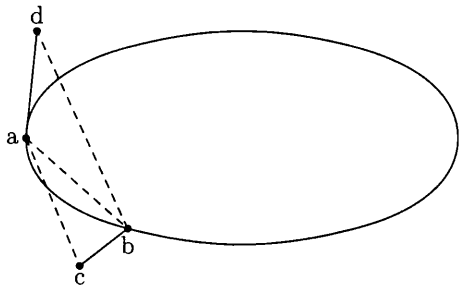

Figure 5.4: A simple example of points connectivity.

Once all the checks are performed and the web is built, the list of points is sorted by distance from node i. Then the n closest vertices are chosen as the neighbours for the Taylor expansion. As a result, a node not directly connected to i by an edge can be selected as a neighbour when assembling the system of equations. This procedure avoids using nodes directly connected to i that are not geometrically close to it, and guarantees the distribution of the neighbours around each node. Typical examples of neighbours of a node in the flow field and of a boundary node on a cylinder are shown in Figures 5.5 and 5.6 respectively. The following algorithm explains how neighbours are chosen:

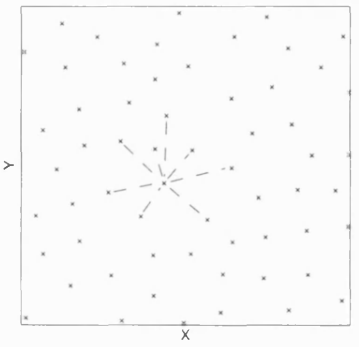

Figure 5.5: Example of neighbours of a node in the flow field.

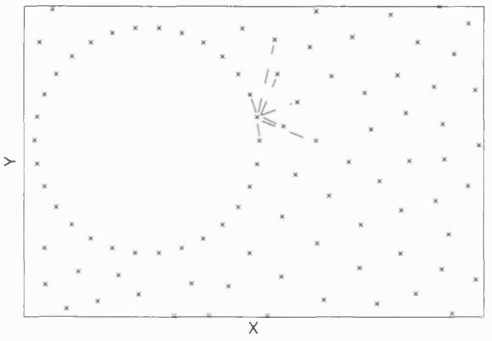

Figure 5.6: Example of neighbours of a boundary node on a cylinder.

ALGORITHM 4.2

for each node $i = 0, 1, \ldots, N-1$ **do**
  Add the nodes directly connected to it.
  for each node j in the web **do**
    if distance(i,j)<dx **then**
      Add the nodes connected to it.
    end if
  end for
  Repeat the **for** loop for every new node added to the web.
  if simulating flow over a solid body **then**
    for each node j in the web **do**
      Check i-j connectivity. If not separated by the boundary add j to list of neighbours.
    end for
  end if
  Sort list of neighbours by distance.
  Chose the n closest nodes as the neighbours to node i.
end for

5.5 Node movement

Once the solution Ψ_i is computed, the local velocities are acquired, which permits the calculation of the control point movement. There are several schemes that can be used to accomplish this task, depending on the desired accuracy, efficiency and simplicity. But when dealing with large systems, as in this case, storage requirement plays a critical role in the choice of the method. Runge-Kutta methodology offers an attractive tool for the formulation of a numerical integration technique that minimizes memory usage. In the current model the velocities are calculated and the nodes moved using the low storage Runge-Kutta scheme of Williamson [111], which in two-dimensional problems requires 4 memory locations per node, one for each of the coordinates and the velocities. Starting with the solution $x(t)$ of the initial value problem:

$$\dot{x} = f(x(t)), \quad x(0) = x_0, \tag{5.21}$$

the nth-order algorithm to advance the set of differential equations over a time step Δt is:

$$\begin{aligned} \dot{x_j} &= M_j \dot{x}_{j-1} + \Delta t f(x_{j-1}), \quad j = 1, 2, \ldots, n \\ x_j &= x_{j-1} + C_j \dot{x_j}, \end{aligned} \tag{5.22}$$

where M_j and C_j are defined by the Runge-Kutta coefficients $\beta_{j,i}$, w_j and α_j:

$$\begin{aligned} C_j &= \beta_{j+1,j}, \quad j \neq n, \\ C_n &= w_n, \\ M_1 &= 0, \\ M_j &= \begin{cases} (w_{j-1} - C_{j-1})/w_j, & j \neq 1, \kappa_j \neq 0, \\ (\beta_{j+1,j-1} - \alpha_j)/C_j, & j \neq 1, \kappa_j = 0. \end{cases} \end{aligned} \tag{5.23}$$

By definition $\sum_{j=1}^{n} w_j = 1$ and $\alpha_j = \sum_{i=1}^{j-1} \beta_{j,i}$, $\alpha_1 = 0$, where the coefficients $\beta_{j,i}$ are the intermediate weights of each Runge-Kutta step j. The precise values of C_j and M_j are determined depending on the order of the scheme. For a second-order scheme they are:

$$\begin{aligned} M_1 &= \alpha_2, \quad M_2 = w_2, \\ C_1 &= 0, \quad C_2 = (w_1 - M_1)/w_2, \end{aligned}$$

while for a third-order scheme they are:

$$\begin{aligned} M_1 &= \alpha_2, \quad M_2 = \beta_{32}, & M_3 &= w_3, \\ C_1 &= 0, \quad C_2 = (w_1 - M_1)/w_2, & C_3 &= (w_2 - M_2)/w_3. \end{aligned}$$

In the current model the node motion is calculated using a third-order Runge-Kutta scheme, where Equations (5.22) are solved through a three step loop. The values of the Runge-Kutta coefficients $\beta_{j,i}$, w_j and α_j used are those given by Williamson([111], Table 1). After every step the new values of u_j, v_j, x_j and y_j overwrite the previous ones so only 4 storage locations are needed per node.

5.6 Viscous diffusion

As discussed in §2.2, in inviscid incompressible flow vorticity is transported by the velocity field as a material element. However, in viscous flow there is an additional mode of transport, diffusion, due to viscosity, and as a result vorticity is transported via advection and diffusion. Thus it moves from regions of large vorticity magnitude to regions of lesser magnitude. The vorticity transport equation (2.12) is divided into separate advective and diffusive terms:

$$\frac{\partial \omega}{\partial t} + \mathbf{U} \cdot \nabla \omega = 0, \tag{5.24}$$

$$\frac{\mathrm{d}\omega}{\mathrm{d}t} = \nu \nabla^2 \omega, \tag{5.25}$$

which are solved consecutively. In this case the computation of the vorticity development depends on the calculation of $\nabla^2\omega$. This is accomplished via a moving least-squares method as in the work of Marshall and Grant [41], who proved the technique to be robust and reliable. The vorticity about a node i is expressed in a second order least-square fit as:

$$\omega_j - \omega_i = \omega_x x_{ij} + \omega_y y_{ij} + \omega_{xx} x_{ij}^2/2 + \omega_{xy} x_{ij} y_{ij} + \omega_{yy} y_{ij}^2/2. \tag{5.26}$$

Once Equation (5.26) is solved, the coefficients of the polynomial are used to estimate $\nabla^2\omega$ since for a plane flow

$$\nabla^2 \omega = \omega_{xx} + \omega_{yy}.$$

In practice, as explained by Marshall and Grant [41], to avoid numerical problems in regions of large vorticity gradient, the polynomial is fit to $\log|\omega|$ and the derivatives of ω are computed using the chain rule for differentiation, for example:

$$\begin{aligned} \frac{\partial(\log|\omega|)}{\partial x} &= \frac{\partial(\log|\omega|)}{\partial \omega}\frac{\partial \omega}{\partial x} \\ &= \frac{\omega_x}{\omega}, \end{aligned}$$

and

$$\begin{aligned} \frac{\partial^2(\log|\omega|)}{\partial x^2} &= \frac{\partial}{\partial x}\left[\frac{\partial(\log|\omega|)}{\partial \omega}\frac{\partial \omega}{\partial x}\right] \\ &= \frac{\partial}{\partial \omega}\left[\frac{\partial(\log|\omega|)}{\partial \omega}\frac{\partial \omega}{\partial x}\right]\frac{\partial \omega}{\partial x} + \frac{\partial(\log|\omega|)}{\partial \omega}\frac{\partial^2 \omega}{\partial x^2} \\ &= \frac{\partial^2(\log|\omega|}{\partial \omega^2}\left(\frac{\partial \omega}{\partial x}\right)^2 + \frac{\partial(\log|\omega|)}{\partial \omega}\frac{\partial^2 \omega}{\partial x^2} \\ &= \frac{\omega_{xx}}{\omega} - \frac{\omega_x^2}{\omega^2}. \end{aligned}$$

However, if the vorticity is small or changes sign, Equation (5.26) is applied directly. Once the diffusive term is computed, the vorticity is updated via a forward-Euler step, a technique used by Russo [60]:

$$\omega_t = \omega_{t-1} + \frac{\mathrm{d}\omega_{t-1}}{\mathrm{d}t}\Delta t, \tag{5.27}$$

where Δt is the time step.

The local velocities are always computed and nodes are moved as described in §5.5, but for viscous computation on a moving mesh there is a restriction on the time step due to stability conditions. For the current method, the well-known criterion for a square grid is applied [41, 60]:

$$\Delta t \leq \frac{l^2}{2\nu}, \tag{5.28}$$

where l is the minimum permissible edge length between two control points. At the beginning of the simulation, once the kinematic viscosity ν and the triangulation criteria are defined, Δt is computed and set to be used when moving the nodes.

5.7 Mesh update

The continuous evolution of vorticity via advection and diffusion, and the movement of the nodes affects the quality of the triangles, which stretch and compress, deforming the mesh. Since the approximation of the streamfunction and the interpolation of the vorticity on the mesh in the current method depends on the triangulation, a distorted grid will cause a dramatic increase in the numerical error. To overcome the loss of accuracy due to Lagrangian distortion and maintain the spatial resolution of the vorticity field, the computational domain is remeshed every few time steps. This process is of critical importance in triangulated vortex methods [14, 17, 41], especially in simulations of rotating fluids where the deformation of the control point distribution can be intense.

Remeshing consists of rediscretising the computational domain, then recalculating the vorticity distribution by interpolation on the new nodes. The approach adopted in order to achieve this task is by setting a minimum and maximum edge length, $l_{\min}$ and $l_{\max}$, in the triangulation, which also imposes the required triangle qualities. If two control points lie closer to each other than $l_{\min}$, they are merged so the short edge is replaced by one node with a combined vorticity value which conserves the total mesh circulation. The four edges defined by the previous two vertices are collapsed into two segments sharing the new node. This amalgamation is necessary first, for viscous diffusion stability, Equation (5.28), second, for ensuring the quality of the triangles and third, for maintaining the number of control points so it does not become too big. If an edge becomes longer than $l_{\max}$, it is split in half by inserting a new node at its midpoint where the vorticity is calculated by interpolation. Adding points to the mesh ensures the spatial resolution and the smoothness of the vorticity distribution. Finally, as vorticity diffuses towards the outer boundary of the computational domain, there

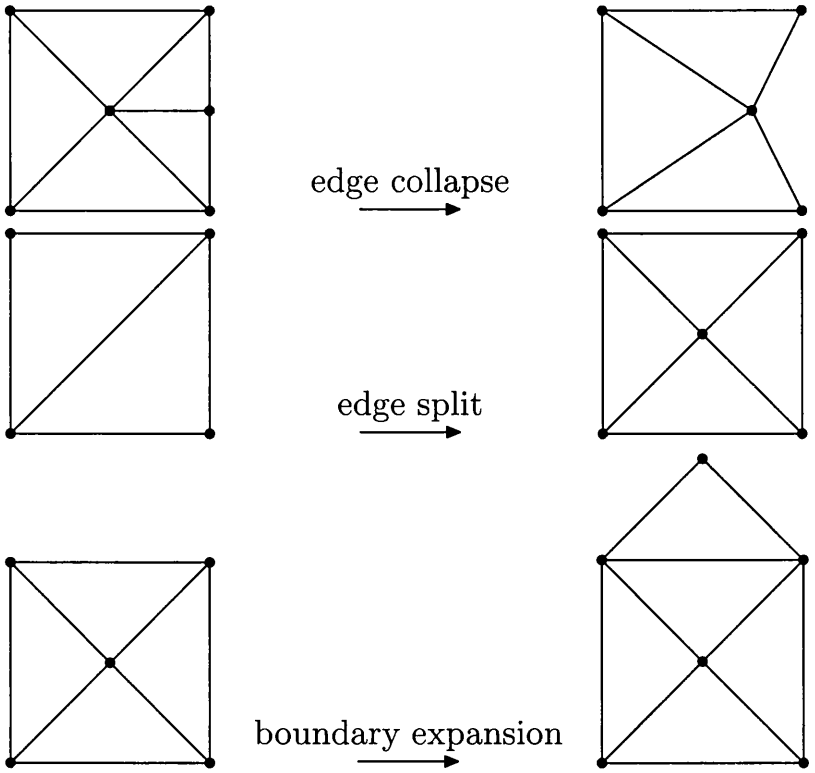

Figure 5.7: Basic remeshing operations

arises the need to expand it. This is accomplished by adding new nodes outside the mesh on the normals to the boundary edges. The distance at which these points are placed is defined by the user. After updating the triangulation, the added nodes form the new boundary of the domain. Figure 5.7 displays three examples of the basic operation discussed.

Chapter 6

Code validation

> *Every item of physical knowledge must therefore be an assertion of what has been or would be the result of carrying out a specified observational procedure.*
>
> *The Philosophy of Physical Science*, Sir Arthur Eddington, 1939

To "simulate" means to build a likeness of a certain situation that might happen in reality. Computer simulations are designed and used to provide solutions to problems or to investigate processes that scientists and engineers are interested in. So, a simulation is a numerical representation of the case under study and not the case itself. Due to restricted computer resources and sometimes the complexity of the study, simplifications and assumptions have to be made when the initial problem is numerically modelled, which inevitably affect the output in advance. Thus, once a new computer code is built, questions about its accuracy and the resemblance of its results to the real model arise: does the software provide numerically stable, convergent and reliable solutions; do the results correspond to the physical requirements of the real situation? To answer these questions, researchers have to assess the credibility and validate the numerical output of the code, a process commonly known as "validation". Validation is a careful analysis of the computed results in order to examine if the simulation agrees with theoretical or experimental observations, and to determine to what extent the computer model is accurate in representing the studied case. The process can be lengthy, costly and time consuming but it is a cornerstone of the development of scientific software. The strategy is to identify and quantify errors and uncertainties by comparing the simulation output to theoretical or experimental data. The accuracy required in the validation activity depends on the application itself, and so the process should assess various levels of accuracy. Thus, there is not one test to use for the verification of the results; numerous methodologies exist to undertake this activity. Verifying numerical codes for all possible situations is an impractical task, so the choice of the procedures depends on the programmer himself and the targets he wants to achieve. The different methods used in determining the credibility of the computed solution can be classified in two groups: internal and external checks. Internal checks consist of a careful analysis of the degree to which the boundary conditions or the physical characteristics of the

results are fulfilled. External checks are based on the comparison of the computed solution to data from other numerical methods or experiments, or to analytical solutions if they exist.

In the current chapter, the numerical method presented in Chapter 5 is validated using different techniques from those two groups. The Method of Manufactured Solutions is used to perform internal checks, while external checks are accomplished by studying potential flows past a cylinder and over an ellipse, and simulating the development of an isolated Lamb-Oseen vortex and wake vortices. Those tests confirm the accuracy and robustness of the current method.

6.1 Method of manufactured solutions

As discussed, computer coding is highly prone to error, thus a critical phase in the development of scientific codes is the verification that the equations are solved correctly. The best benchmarks to use in this operation are exact analytical solutions, which do not need to be realistic since in this case the validation is purely mathematical. There are numerous methods of verification; one commonly used in the field of computational fluid dynamics is the Method of Manufactured Solutions (MMS) [112], which provides a high level of confidence in the implementation of the code and the expected order of accuracy of the results. Roache [112] assesses the method as such: "When used with systematic grid refinement studies, which are remarkably sensitive, MMS produces strong Code Verifications with a theorem-like quality and a clearly defined completion point". The method is based on Polya's saying: "Only a fool starts at the beginning; the wise one starts at the end" [113]. Normally in differential equations the givens are the differential operators, the source term, also called the right-hand side, and the initial and boundary conditions. The MMS allows us to pick an analytical solution, then set the differential equations and the initial and boundary conditions based on it. If the code is well implemented, the computed solution will be very accurate compared to the analytical one, which provides the verification needed. The comparison between the computed and chosen values is done through an error measure. The order of accuracy of the algorithm is critical to the efficiency of the MMS. As a result, grid refinement must demonstrate the convergence of the numerical solution, which means that when the grid is refined the error should decrease.

To verify the code used in the current study using MMS, different solutions for the streamfunction ψ are chosen; in each case, the vorticity field and the velocity on the boundary are defined using equations (2.15) and (2.5). These conditions are set in the numerical model, then the computed solutions are checked against the initial ones by calculating a maximum error $\epsilon_{\max}$, which is defined as:

$$\epsilon_{\max} = \frac{\max|U_{\text{chosen}} - U_{\text{computed}}|}{\max|U_{\text{chosen}}|}. \tag{6.1}$$

To begin, a first order solution for the streamfunction, $\psi{=}x + y$, was tested. As a result the field had zero vorticity, $\omega{=}0$, and on the outer boundary the velocities were

set to u_x=1, u_y=−1. Two simulations were run with different numbers of nodes N in order to assess the effect of grid refinement on the accuracy of the results. In both cases, the code was very accurate in computing the velocity with maximum error of 1.47% for N=5458 and 0.48% for N=14520. The improvement of the results with the increase in the number of nodes is expected since a finer mesh leads to a better representation of the flow. Figure 6.1 shows the streamlines of the computed ψ and Figure 6.2 shows the contour lines of the absolute error, ϵ, for N=14520.

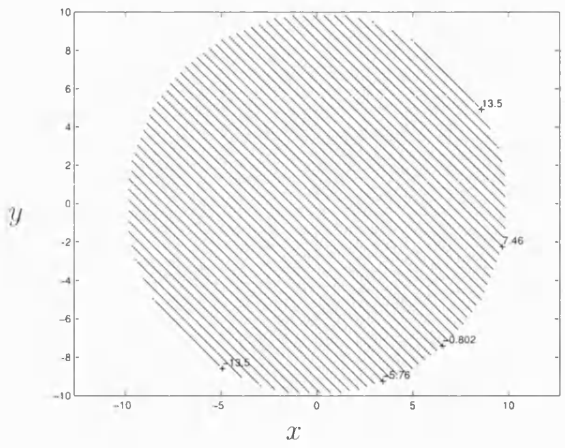

Figure 6.1: The streamlines of the calculated streamfunction using MMS for ψ=$x+y$; number of nodes in the computational domain N=14520.

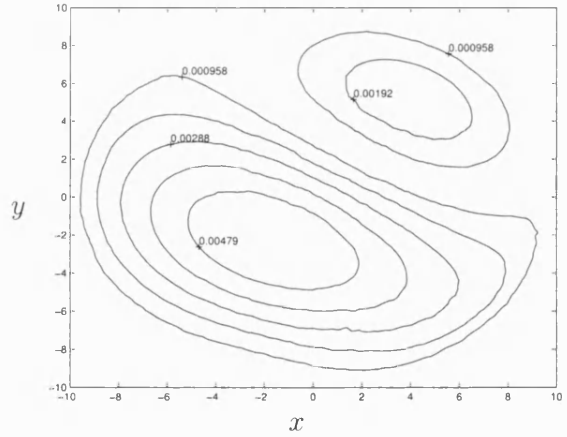

Figure 6.2: Contour lines of absolute error between the chosen and computed velocity using MMS for ψ=$x+y$; number of nodes in the computational domain N=14520.

After the satisfactory results of the first case, another problem was considered where ψ was chosen to be a second order function, ψ=x^2+y^2, which produces circular streamlines. Consequently, the vorticity of the computational domain was set to

$\omega=-4$, the velocities on the boundary to $u_x=2y$ and $u_y=-2x$, and simulations were run for different grid densities, $N=8628$, 9541 and 13313. In all three cases, the computed values matched the theoretical ones well, though the maximum error $\epsilon_{\max}$ was higher than in the previous problem, $\psi=x+y$, but still small and acceptable. Moreover, as expected, the refinement of the mesh improves the results. When the computational domain is discretized with $N=8628$ nodes $\epsilon_{\max}$ is 3.12%, and then the error decreases with increasing N to 2.46% for $N=9541$ and 2.19% for $N=13313$.

Since the streamlines in this case are circular, the velocity in the domain is rotational. The contour plots of the velocity and absolute error for the coarsest mesh are displayed in Figures 6.3 and 6.4 respectively, while Figures 6.5 and 6.6 show the streamlines of the calculated streamfunction and contour plots of the absolute error ϵ for the simulation with $N=9541$. Contour plots of ϵ for the last case, $N=13313$, are depicted in Figure 6.7.

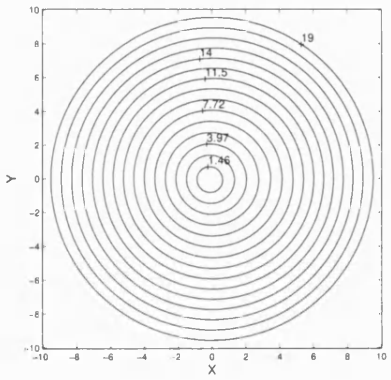

Figure 6.3: Contour plots of the calculated velocity U_{computed} using MMS for $\psi=x^2+y^2$; number of nodes in the computational domain $N=8628$.

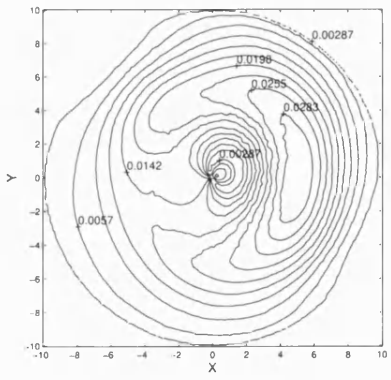

Figure 6.4: Contour lines of the absolute error ϵ using MMS for $\psi=x^2+y^2$; $N=8628$.

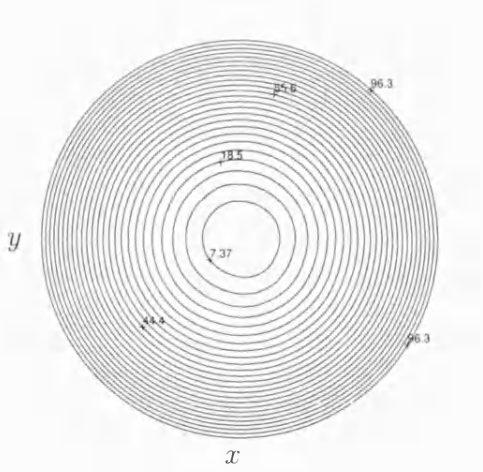

Figure 6.5: Contour lines of the calculated streamfunction ψ_{computed} using MMS for $\psi{=}x^2{+}y^2$; number of nodes in the computational domain $N{=}9541$.

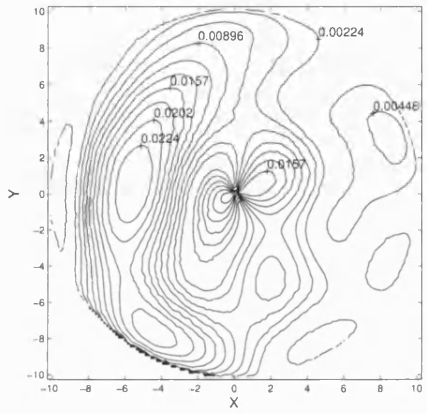

Figure 6.6: Contour plots of the absolute error ϵ using MMS for $\psi{=}x^2{+}y^2$; $N{=}9541$.

In the literature, vorticity is often considered to have a Gaussian distribution, thus a third case for code verification was considered with $\psi{=}e^{-r^2}$, where $r^2{=}x^2{+}y^2$. As a result, the flow vorticity is $\omega{=}4(1+r^2)e^{-r^2}$, and the boundary conditions are $u_x{=}{-}2ye^{-r^2}$ and $u_y{=}2xe^{-r^2}$. In a simulation run on a grid of 9975 nodes, the maximum error is found to be $\epsilon_{\text{max}}{=}2.94\%$. Contour plots of the absolute error in this case are displayed in Figure 6.8. It is interesting to note that in this case the error increases towards the centre from the outside until it decreases again exactly at the centre of the domain. This can be explained by the Gaussian distribution of the vorticity. As the vorticity gradient increases towards the centre, more nodes are needed for a better approximation. However, in this case the mesh was not fine enough in this region to provide an exact vorticity distribution, which explains the increasing error between the theoretical and computed vorticity. At the centre, on the other hand, the vorticity gradient decreases, thus the number of nodes available in this region is able to give a

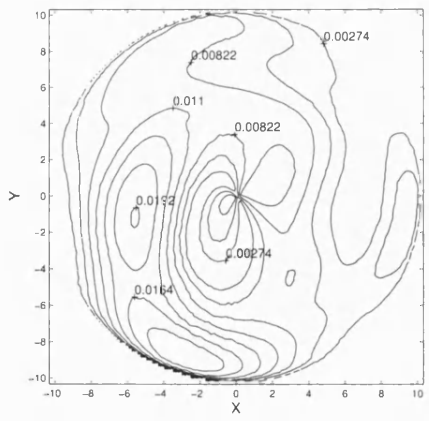

Figure 6.7: Contour plots of the absolute error ϵ using MMS for $\psi{=}x^2{+}y^2$; $N{=}13313$.

better approximation for the vorticity field, which decreases the error ϵ. Increasing the number of nodes in the computational domain should decrease the maximum error as a finer mesh provides a better vorticity distribution. Indeed, in another simulation with $N{=}14909$ the error decreases to $\epsilon_{\max}{=}1.67\%$, affirming the robustness of the current method.

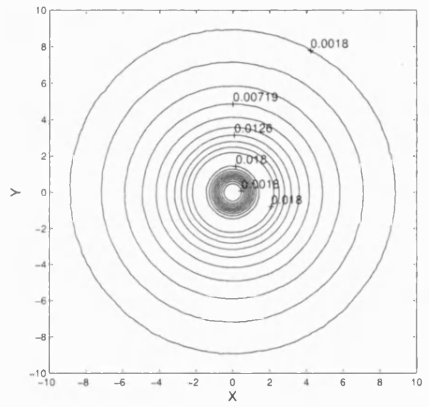

Figure 6.8: Contour plots of the absolute error ϵ using MMS for $\psi{=}e^{-r^2}$; $N{=}9975$.

6.2 Flow past a circular cylinder

Potential flow around a circular cylinder is one of the most basic problems in fluid dynamics and offers a canonical test for validating new numerical methods in CFD. Therefore, it is essential to test the current code with this problem. It is well established that in viscous regimes, the flow around a circular cylinder becomes unstable

and develops wake vortices, a process known as vortex shedding. However, for potential flows, the inviscid theory predicts the smooth and complete closure of the flow behind the cylinder, thus no wake is generated [20]. As a result, the field around the cylinder should be symmetrical about the horizontal and vertical axes of the body. Hence the streamlines are also symmetrical about both axes.

In order to calculate the streamfunctions and velocities of a potential flow around a cylinder, the body is assumed to be a streamline, so the no penetration condition is applied, and the free stream velocity U_∞=1. Thus the streamfunction on the geometry boundary is held constant, and the velocities on the outer boundary of the computational domain are u_x=1 and u_y=0. The streamfunction for such a problem is:

$$\psi_{\text{theoretical}} = U_\infty(r - R^2/r)\sin\theta, \tag{6.2}$$

where r and θ are the radial coordinates of the point and R the cylinder radius. Subsequently, on the surface of the cylinder, r=R, the streamfunction is ψ=0. The velocity field is obtained by differentiating Equation (6.2):

$$\begin{aligned} U_r &= \frac{1}{r}\frac{\partial\psi}{\partial\theta} \\ &= U_\infty\cos\theta(1 - R^2/r^2), \\ U_\theta &= -\frac{\partial\psi}{\partial r} \\ &= -U_\infty(1 + R^2/r^2)\sin\theta. \end{aligned}$$

From the above equations, one can easily determine two stagnation points on the boundary at θ=0 and θ=π where U=0, and the absolute maximum velocity on the surface at θ=$\pi/2$ and θ=$3\pi/2$ where U=$2U_\infty$.

For this simulation, the computational domain is a circular mesh of radius r_{mesh}=4 discretized by N=9258 points, and the circle has a radius R=1. In order to assess the accuracy of the numerical model for this problem, a maximum error between the theoretical and calculated streamfunction is computed as follow:

$$\epsilon_{\max} = \frac{\max(|\psi_{\text{calculated}} - \psi_{\text{theoretical}}|)}{\max|\psi_{\text{theoretical}}|}. \tag{6.3}$$

The code yields very good agreement between the computed and theoretical streamfunction and velocity, with a maximum error, $\epsilon_{\max}$, of 0.65%. Figure 6.9 shows the streamlines of the flow around the cylinder, while the velocity vectors are presented in Figure 6.10. Conforming to inviscid theory, the flow is symmetric around the body and closes smoothly behind it. Two stagnation points are observed, one on the approaching surface, θ=π, and the other on the trailing surface, θ=0, and the locations of maximum velocity U=$2U_\infty$ are clearly seen at θ=$\pi/2$ and θ=$3\pi/2$. Contour plots of absolute difference between the theoretical and calculated values, $|\psi_{\text{calculated}} - \psi_{\text{theoretical}}|$, are presented in Figure 6.11.

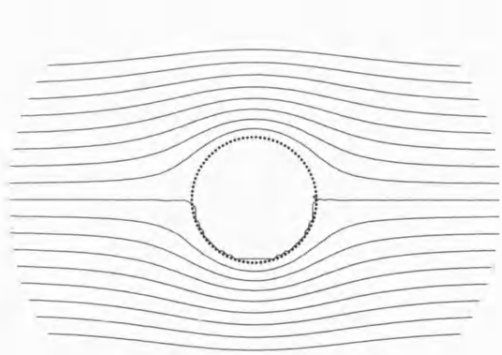

Figure 6.9: Streamlines of a potential flow around a cylinder.

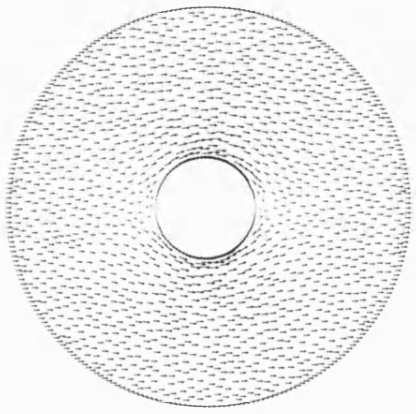

Figure 6.10: Velocity vectors of a potential flow around a cylinder.

6.3 Potential flow over an ellipse

An ellipse is the closest geometrical approximation to an aerofoil over whose surface the complex velocity potential can be calculated analytically. This means that potential flow over an ellipse became a classical problem in aerofoil theory. For an ellipse given by

$$\frac{x^2}{a^2} + \frac{y^2}{b^2} = 1, \tag{6.4}$$

the potential for the flow over it is [114]:

$$w = -\frac{1}{2}U(a+b)\left[\frac{e^{-i\alpha}(z+\sqrt{z^2-c^2})}{a+b} + \frac{e^{i\alpha}(z-\sqrt{z^2-c^2})}{a-b}\right], \tag{6.5}$$

where a and b are respectively the semi major and semi minor axes of the ellipse, U the velocity on the surface, z the complex variable $z{=}x + iy$, α the angle of attack of

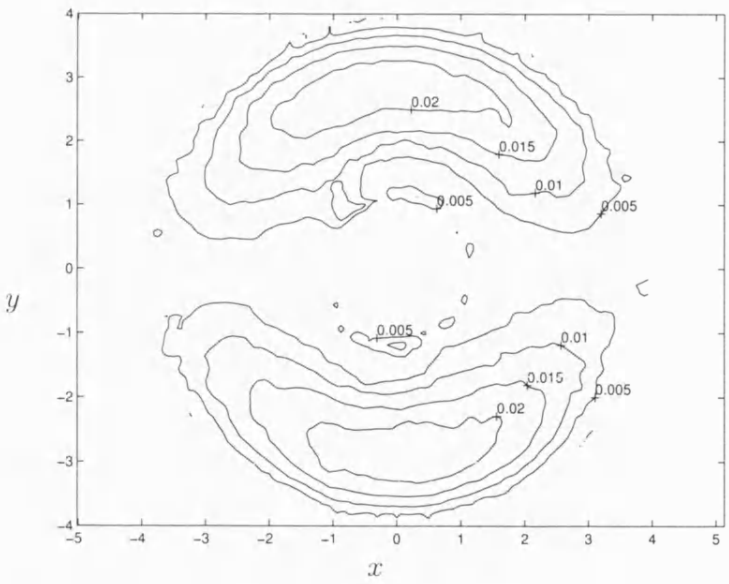

Figure 6.11: Contour lines of the absolute difference between the theoretical and calculated streamfunction, $|\psi_{\text{calculated}} - \psi_{\text{theoretical}}|$, around a cylinder.

the ellipse and $c^2{=}a^2 - b^2$. The velocities on the surface can be calculated as:

$$u = \frac{1}{2}\left(\frac{\mathrm{d}w}{\mathrm{d}z} + \frac{\mathrm{d}\overline{w}}{\mathrm{d}\overline{z}}\right), \tag{6.6a}$$

$$v = \frac{i}{2}\left(\frac{\mathrm{d}w}{\mathrm{d}z} - \frac{\mathrm{d}\overline{w}}{\mathrm{d}\overline{z}}\right), \tag{6.6b}$$

where $\overline{w}$ and $\overline{z}$ are the complex conjugates of w and z respectively. Equations (6.5) and (6.6) can be used for code validation by comparing the numerical results to the analytical ones. However, to validate the current model, a different approach was used: instead of computing the complex potential for the flow, the maximum surface velocity $U_{\text{maxsurface}}$ is found and compared to the value given by Lighthill [115] for incompressible potential flows:

$$U_{\text{maxsurface}} = U_\infty(1 + \varepsilon), \tag{6.7}$$

where U_∞ is the free stream velocity, and ε the thickness or aspect ratio of the ellipse, $\varepsilon{=}a/b$.

Potential flow over ellipses of different thicknesses, 0.12, 0.25 and 0.5, at different angles of attack is simulated using the current numerical method. The body in the computational domain is assumed to be a streamline so the no penetration boundary condition is applied, and the free stream velocity and the semi major axis are both chosen to be unity for all cases, $U_\infty{=}1$ and $a{=}1$. As a result, at a zero angle of attack the velocities on the outer boundary are set to $u_x{=}1$ and $u_y{=}0$. In order to represent

the body at an angle of attack α, the ellipse is kept in its original position, while the free stream velocity in the computational domain is applied at the required angle with respect to the horizontal axis of the body, as shown in Figure 6.12. Therefore, the velocities at the outer boundary are set to u_x=cos α and u_y=sin α. This is a well adopted technique in CFD simulations [116].

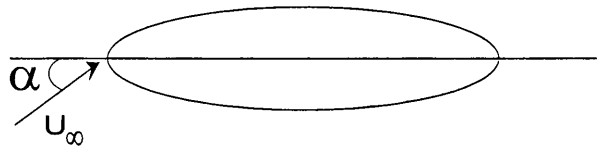

Figure 6.12: Ellipse at angle of attack α.

It is found that the error depends on the aspect ratio of the body ε. For the thinnest ellipse, ε=0.12, the maximum error is $\epsilon_{\max}$=1%, then it increases to 2.2% for ε=0.25 and 6.8% for the thickest body ε=0.5.

For the present problem, another test is performed to assess the validity and accuracy of the numerical code. The streamfunction in a potential flow over an ellipse can be calculated in terms of elliptic coordinates [114, p.169]:

$$\psi_{\text{theoretical}} = U_\infty(a+b)\sinh(\xi-\xi_0)\sin(\eta-\alpha), \tag{6.8}$$

where ξ and η=$\tan^{-1}(y/x)$ are the elliptic coordinates of the points in the computational domain and ξ_0=$\cosh^{-1}(a/c)$=$\sinh^{-1}(b/c)$ the coordinate of the points on the ellipse. This solution is used to calculate the error between the theoretical and computed streamfunctions at α=0. The code yields good results for the streamfunction with an error of 3.5% for the 0.25 and 0.5 thickness ratio ellipses, and 3.6% for ε=0.12. Contour lines of the absolute difference between the theoretical and computed streamfunctions, $|\psi_{\text{theoretical}} - \psi_{\text{computed}}|$, are shown in Figure 6.13. The streamlines of the potential flow over the ellipses of different aspect ratio at different angles of attack are presented in Figures 6.14–6.16. The results for the thickest ellipse, Figure 6.16, are in very good agreement with previous studies conducted on this subject [116, Figure 2].

6.4 Isolated Lamb-Oseen vortex

For viscous plane flows, analytical solutions are available to check the accuracy of the computational method. After conducting checks for potential flow, the performance of the current method was assessed for viscous calculations using an isolated Lamb-Oseen vortex [117, §334a] with a Gaussian vorticity distribution. The vorticity starts as an impulsive source of circulation and evolves over time according to:

$$\omega(x,y,t) = \frac{\Gamma_0}{2\pi\sigma^2} e^{-[(x-x_0)^2+(y-y_0)^2]/2\sigma^2}, \tag{6.9}$$

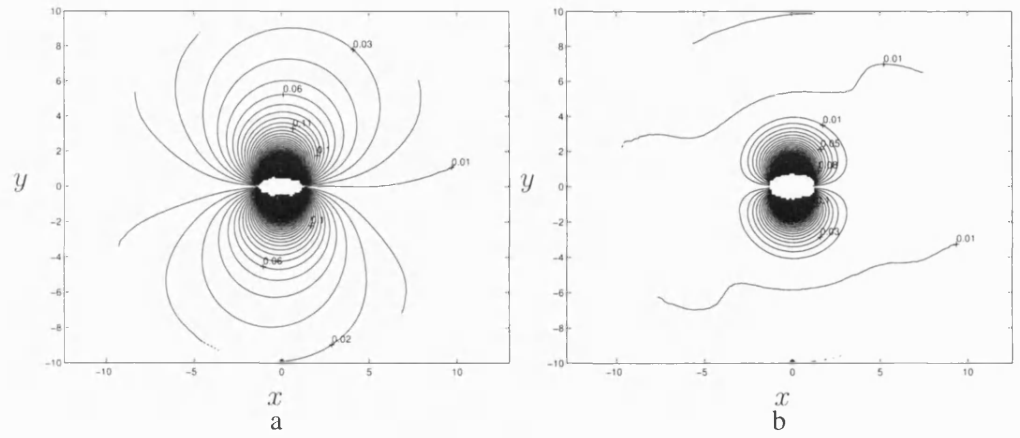

Figure 6.13: Contour lines of the absolute difference between the theoretical and computed streamfunctions over an ellipse of thickness ratio a:0.25; b:0.5.

where Γ_0 is the initial circulation of the vortex, (x_0, y_0) its initial position and the standard deviation $\sigma=\sqrt{2\nu t}$ is determined by its core radius r_c according to $\sigma=0.6308 r_c$ [118].

The time decay of a Lamb-Oseen vortex centered at $x_0=1$, $y_0=0$ with an initial core radius of $r_c=0.125$, and initial standard deviation $\sigma_0=0.07885$, is investigated using the current method and compared with the theoretical predictions. For this simulation, the dimensionless time is $t^*=t\Gamma_0/r_c^2$, and the kinematic vorticity was set to $\nu=0.00303$ so that the Reynolds number based on the circulation, $\mathrm{Re}=\Gamma_0/\nu$, is low, $\mathrm{Re}=330$. To achieve a smooth vorticity distribution, especially around the core of the vortex, the computational domain was discretized initially with the following criteria: minimum and maximum triangulation areas were set to $\mathrm{A_{min}}=0.0004$ and $\mathrm{A_{max}}=0.001$ respectively, and for remeshing the edge length was allowed to vary between $\mathrm{h_{min}}=0.01$ and $\mathrm{h_{max}}=0.1$. The initial error tolerance between the specified and computed values of the vorticity was set to 10^{-4} in order for the mesh to be finer around the non-zero vorticity core than the rest of the flow. These parameters were found to give a satisfactory first triangulation, which is critical to accuracy of the results. The quality of the mesh affects the vorticity distribution, which influences the decay of the vortex.

Theoretically, it is well known that a Lamb-Oseen vortex has a zero self-induced velocity, thus it is spatially stable. With time, the vortex decays and its core radius expands. The computed and theoretical transient vorticity distributions and the core radius expansion for this vortex, displayed in Figure 6.17, are found to be in good agreement. It is clear that the isolated vortex does not change position but just decays with time, starting with a fast decay rate that slows down over time. At $t^*=0$ the fit between the curves is perfect, but at later times an error develops and the maximum computed vorticity is lower than the theoretical one. This is an expected result, which is due to the number and position of the control points. In the current case the domain was discretized by 6700 nodes, leading to a maximum error between maximum theoretical and computed vorticities of 6.6% at $t^*=10$ and 6.9% at $t^*=20$.

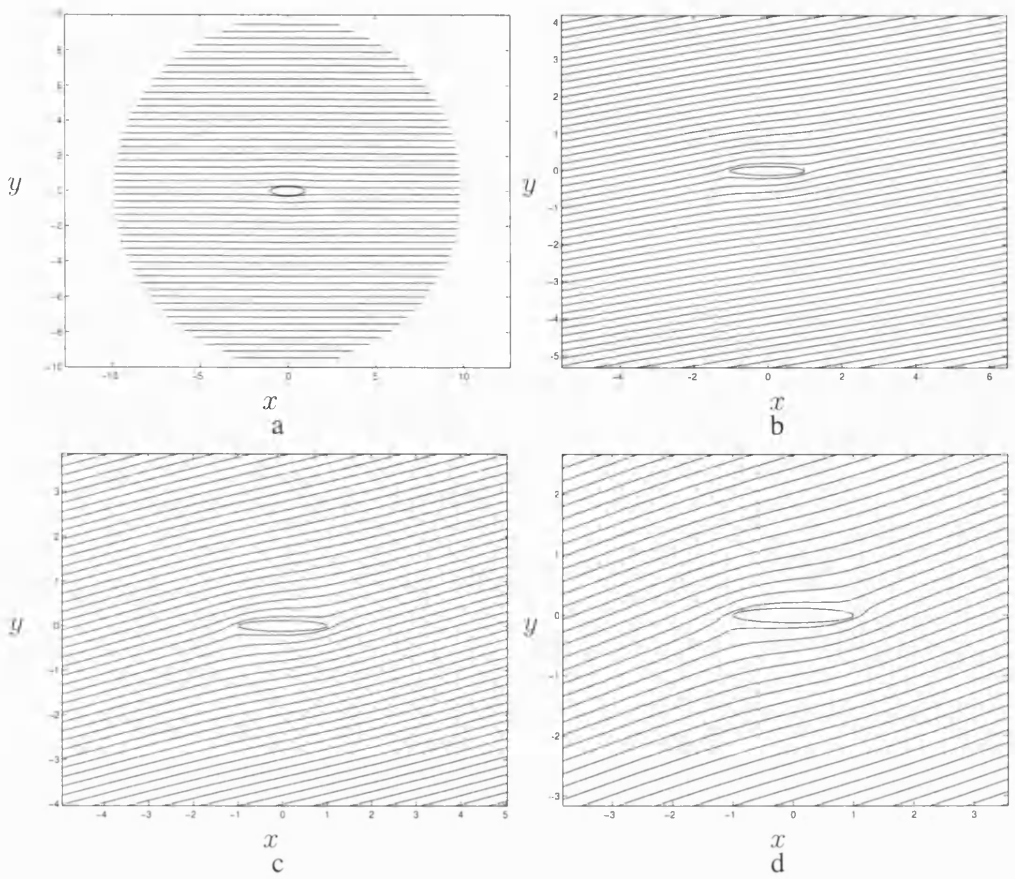

Figure 6.14: Streamlines of the potential flow over an ellipse of aspect ratio 0.12 at different angles of attack; a:0°; b:10°; c:15°; d:20°.

To assess the validity of the code, several simulations with different numbers of nodes N were run for the decaying Lamb-Oseen vortex, and the evolution over time of the maximum difference between the computed and exact vorticities scaled on the maximum theoretical vorticity, $\max|\Delta\omega|/\max\omega$, was computed and is plotted in Figure 6.18. The numbers shown on the graph are the initial number of nodes in the domain before remeshing is applied. During the simulations, due to the expansion of the vortex and remeshing, this number is expected to change. In all cases, the error initially increases with time before reaching an asymptotic value. For the coarsest mesh, N=2498, even at t^*=0 an error is observed, which indicates that this number of nodes is not enough to accurately discretize the flow. For this case the error reaches as high as 16%. As expected, increasing the number of nodes produces a smoother vorticity distribution, which decreases the initial error and improves the accuracy of the calculations. From Figure 6.18 the existence of a critical range of numbers of nodes that greatly affect the error is clear. Increasing N even further outside this range is seen to slightly improve the accuracy while it increases the time cost of the simulation, thus a

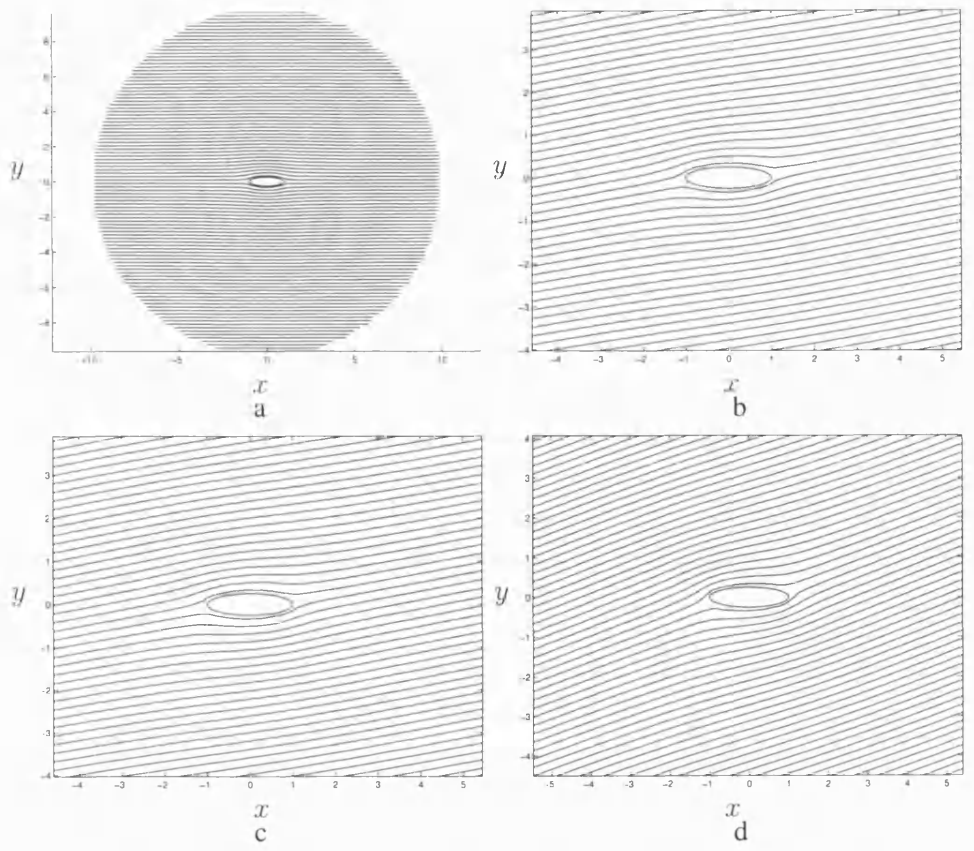

Figure 6.15: Streamlines of the potential flow over an ellipse of aspect ratio 0.25 at different angles of attack; a:0°; b:10°; c:15°; d:20°.

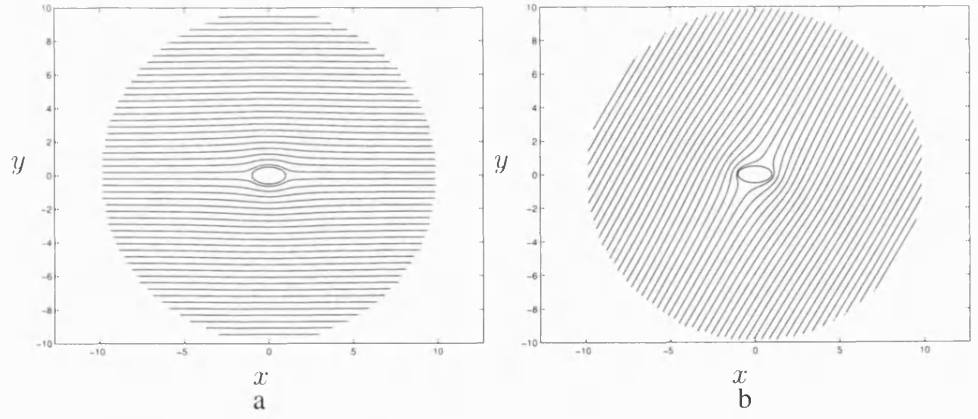

Figure 6.16: Streamlines of the potential flow over an ellipse of aspect ratio 0.5 at different angles of attack; a:0°; b:60°.

careful consideration must be made when deciding on the initial number of points in order to find a good balance between the cost and the accuracy required. The results provided in Figure 6.18 are an extra proof of the robustness of the computational code used in this thesis.

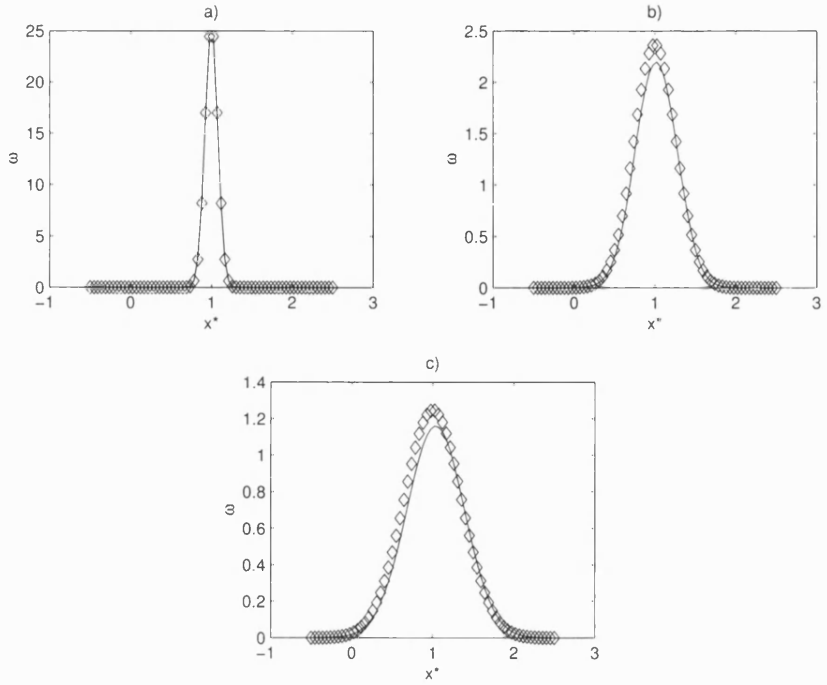

Figure 6.17: The vorticity distribution $\omega(x, y, t*)$ of a Lamb-Oseen vortex at various times. $-$ computed, $\diamond$ theoretical. a: $t = 0$; b: $t = 10$; c: $t = 20$.

6.5 Pair of wing tip vortices

The development of wake vortices was simulated using the current code. Lifting aircraft wings generate spanwise vorticity sheets that rapidly roll-up into vortex structures. The number and strength of the vortices produced depends on the configuration of the lifting surfaces. In the cruise condition, the far wake of the aircraft generally consists of wing tip vortices, which are a pair of counter-rotating monopoles of equal but opposite circulation, Γ, separated by the wing span, b. The experimental investigation of Barker and Crow [119] revealed that after complete roll-up of the vortex sheet, the fundamental dynamics of the wake can be modelled as a two-dimensional problem. Figure 6.19 presents a schematic configuration of this situation. Thus to simulate their downstream behaviour, the wing tip vortices were represented by two symmetrical Lamb-Oseen vortices with initial circulations of $-\Gamma_0$ and Γ_0 centered respectively at $(-b/2,\ 0)$ and $(b/2,\ 0)$. According to Turk et al. [118], for complete roll-up of

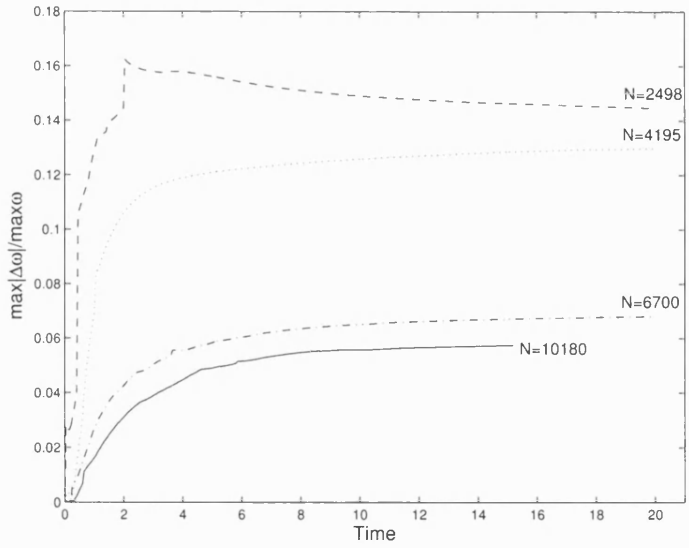

Figure 6.18: Evolution of the Lamb-Oseen vortex: maximum error in vorticity during calculation.

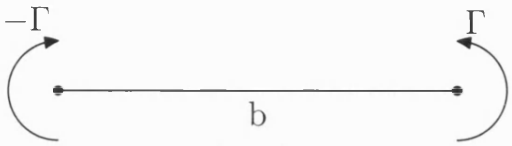

Figure 6.19: Schematic representation of wing tip vortices.

a vortex sheet of a heavy aircraft, a Boeing-777 for example, the core radius of the vortex is assumed to be r_c=0.125b. The non-dimensional system in this problem was built with the following quantities: Γ^*=Γ/Γ_0, t^*=$t\Gamma_0/b^2$ and lengths scaled on b. As a result, the initial non-dimensional standard deviation for both vortices was equal to σ^*=0.6308r_c^*=0.07885. The Reynolds number was set to Re=330 and the mesh specifications were the same as in §6.4. The downstream development of the wake until t^*=22 is depicted in Figure 6.20. The pair of counter-rotating vortices expand, decay and move downwards due to the induced velocity that each monopole exerts on its partner while conserving the symmetry of the vorticity distribution. Once the two vortices hit each other, they do not merge but form a self-propelling dipole. These findings agree well with the results of published studies on aircraft trailing vortices [120, 121] and the observation of the wake development in nature, an example of it being shown in Figure 6.21. As in the isolated vortex case, the vorticity decays rapidly in the first time steps then at a slower rate further on. The vorticity distribution of the wing tip vortices at three different times t^* is displayed in Figure 6.22.

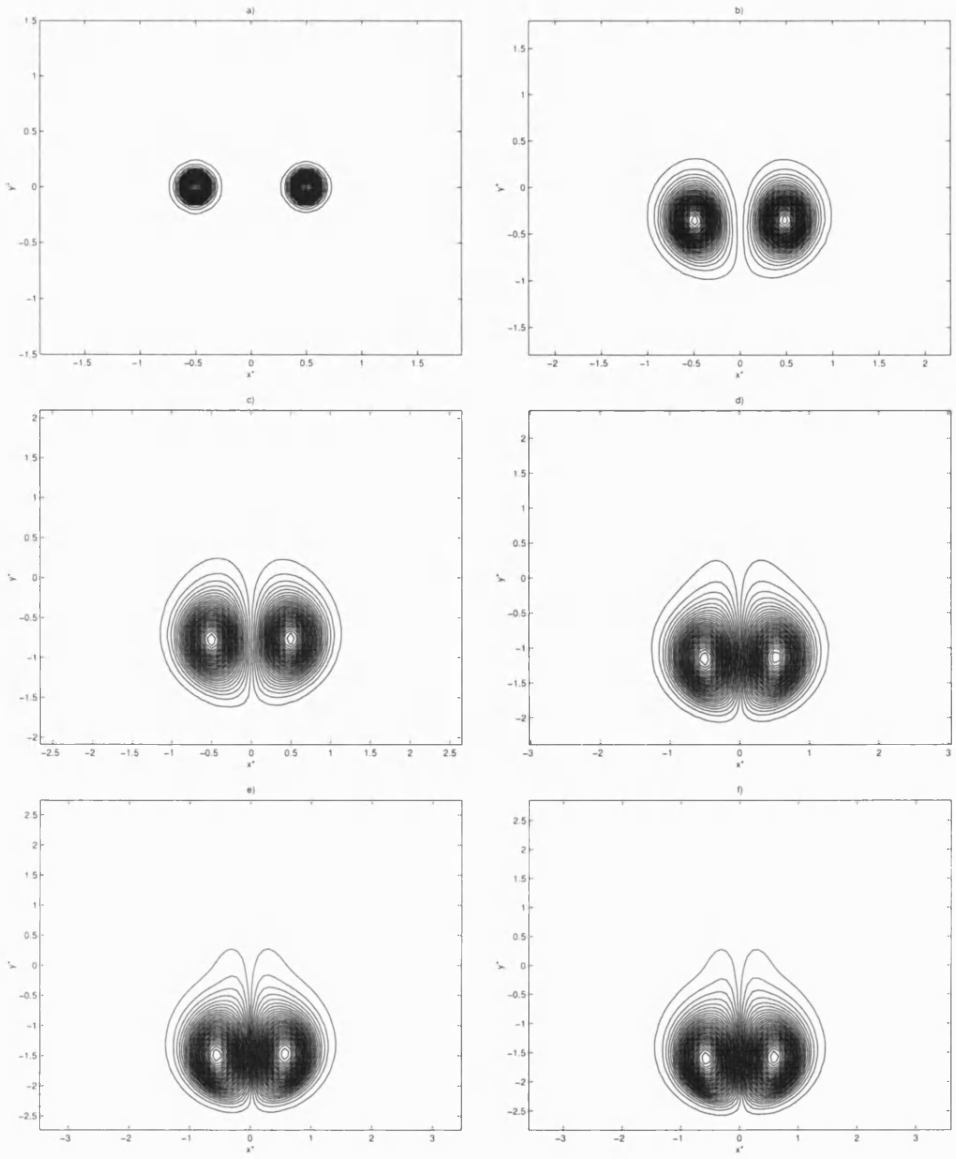

Figure 6.20: The vorticity distribution of the wing tip vortices as they move downstream; a: $t = 0$; b: $t = 5$; c: $t = 10$; d: $t = 15$; e: $t = 20$; f: $t = 22$.

6.6 Four-vortex wake model

The wake of an aircraft can consist of a four-vortex configuration; the wing tip vortices plus an inner pair of monopoles generated by different aerodynamic devices. Two cases exist in such a system as the inner vortices can be co-rotating with the wing tip ones if they are produced by the outer flap edges, or counter-rotating if they are generated by the inner flap edges, the tail wing or the fuselage of the aeroplane. In this

Figure 6.21: The roll-up of wing tip vortices of a Boeing 767 visualised by the perturbation of a cloud layer. Picture taken at London - Gatwick airport 16 June 2007. (Courtesy of Steve Morris - AirTeamImages, private communication)

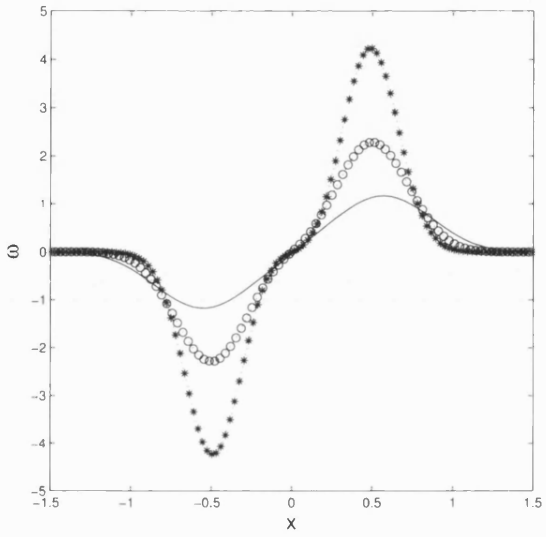

Figure 6.22: Vorticity distribution of the wake vortices at; $*$: t^*=5, $\circ$: t^*=10, $-$: t^*=20.

section the development of the wake of a large heavy commercial aircraft, for example Boeing-747, is investigated. The system is formed by four vortices, two from the main wing tips and two from the tail wing. Since the main wing produces lift while the horizontal tail generates downforce for stability purposes, the half-span plane of the wake after the roll-up of the vorticity sheet consists of a pair of counter rotating vortices. The four-vortex configuration is displayed in Figure 6.23. The outboard vortices are initially characterized by their circulations Γ_1 and $-\Gamma_1$ and their core radius r_{c1}, and are separated by the wing span b_1, while the inboard vortices have initial circulations $-\Gamma_2$ and Γ_2, a core radius r_{c2}, and are separated by the tail span b_2.

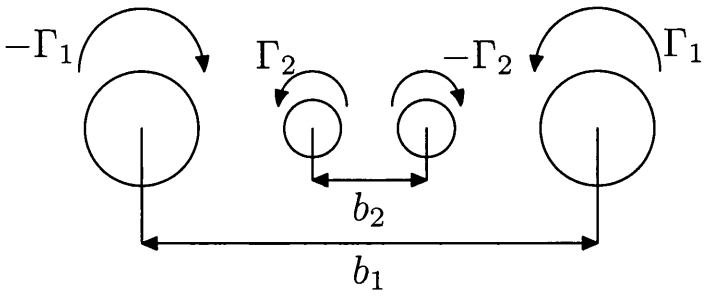

Figure 6.23: Schematic configuration for a four-vortex wake model

Four ratios are determined in this model, Γ_2/Γ_1, b_2/b_1, r_{c1}/b_1 and r_{c2}/b_2, which for aeronautical interest Fabre and Jacquin [122] determined to be in the following ranges; $0.4<\Gamma_2/\Gamma_1<0.5$, $0.1<b_2/b_1<0.5$, $0.01<r_{c1}/b_1<0.2$ and $0.01<r_{c2}/b_1<0.075$. For the current study, the ratios were chosen as $b_2/b_1=0.15$ and $r_{c1}/b_1=0.125$, then following the relation between b_2/b_1 and Γ_2/Γ_1 given by Rennich and Lele [123]:

$$\left(\frac{b_2}{b_1}\right)^3 + 3\left(\frac{\Gamma_2}{\Gamma_1}\right)\left(\frac{b_2}{b_1}\right)^2 + 3\left(\frac{b_2}{b_1}\right) + \left(\frac{\Gamma_2}{\Gamma_1}\right) = 0, \tag{6.10}$$

$|\Gamma_2/\Gamma_1|$ was calculated to be 0.424, which is within the acceptable range. Assuming that the initial standard deviation σ is related to the core radius of the corresponding vortex by the following relation $\sigma=0.6308r_c$ [118] and that the inner vortex radius is equal to $r_{c2}=0.125b_2=0.0187b_1$, σ_1 was found equal to $0.07885b_1$ and σ_2 to $0.01182b_2$. To non-dimensionalise the system of variables, the circulation of the outboard vortices and the span of the main wing were set to $\Gamma_1=1$ and $b_1=1$, then the other variables were calculated correspondingly as described in §6.5.

Previous studies on this subject have shown that the downstream development of the wake depends on the position and characteristics of the vortices [122, 124, 125]. If the distance separating the inner and outer pairs is large, $b_2/b_1 \ll 1$, the inboard vortices escape from the influence of the external ones and evolve as a dipole, while the wing tip vortices keep their trajectories. This configuration is unattractive in aeronautical problems. However, if the pairs are close to each other, the inboard vortices are attracted by the external ones and orbit around them. The results of the current simulation, which are depicted in Figure 6.24, agree well with this evolution. Due to the difference of intensities, the tail wing vortices are drawn by the main ones and roll-up around them, which accelerates their decay rate. Meanwhile, they exert pulling forces on the external vortices, moving them apart and slowing their downward movement, in comparison with the results of the two-vortex wake model, Figure 6.20. Another comparison between the vorticity distribution of the wing tip vortices in the previous case, §6.5, and the current one shows that in a four-vortex wake the decay rate is faster, which might be the effect of the shear forces of the revolving vortices. Figure 6.25 shows the vorticity distribution of the wing tip vortices in both situations at $t^*=10$. It is clear that in the four-vortex wake the vortices are moved apart and their peak vorticity is lower than that of the two-vortex model. In the later stage development of the

flow, the tail vortices completely diminish during their roll-up and the wake becomes a two-vortex model that evolves as observed in §6.5.

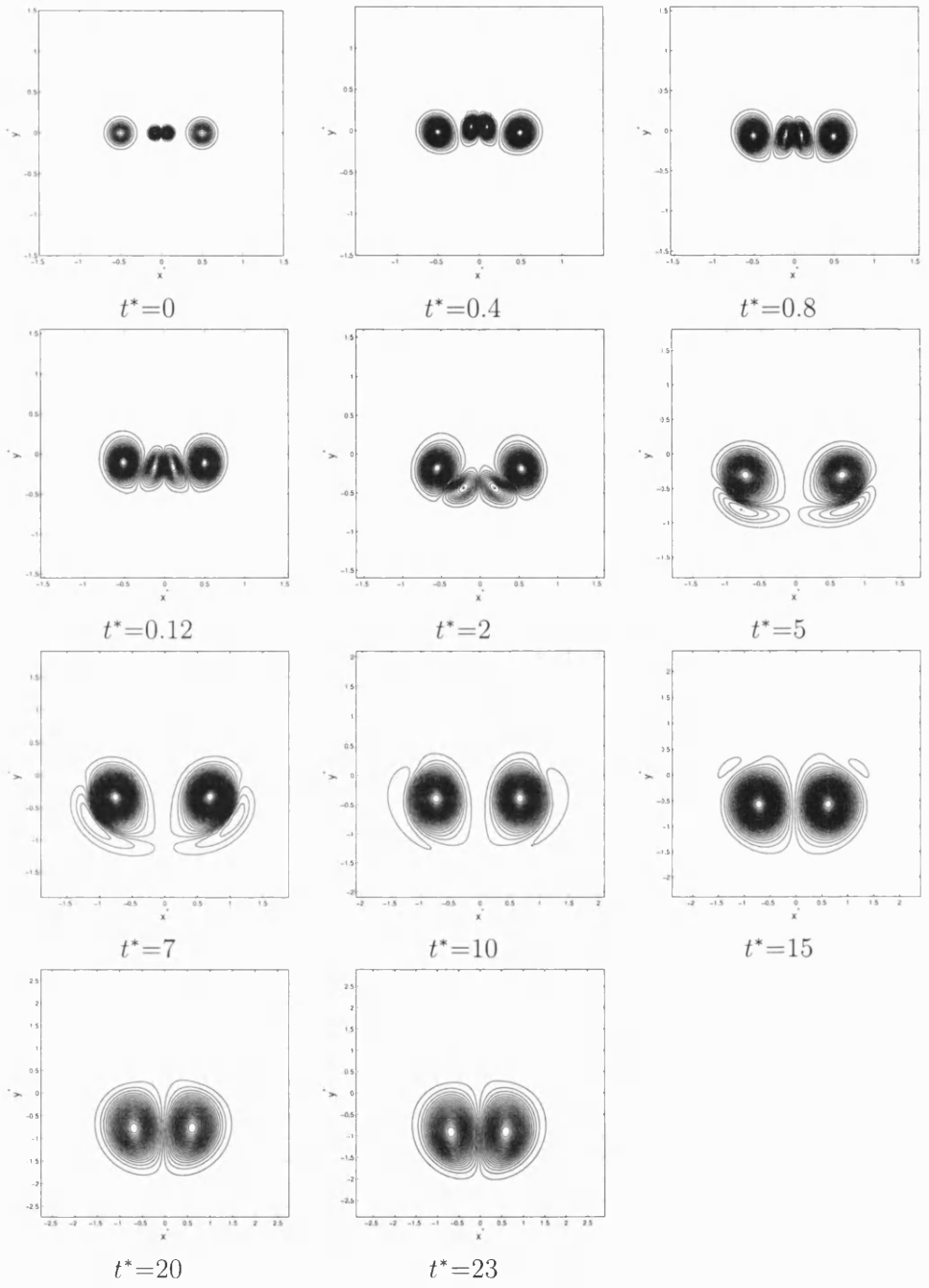

Figure 6.24: Contour plots of vorticity of the four-vortex wake model during the flow development.

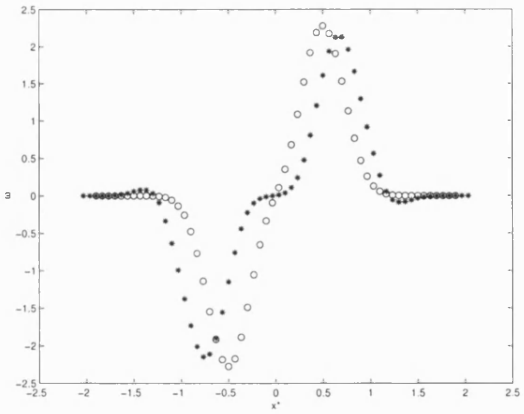

Figure 6.25: A comparison between the vorticity distribution of the wing tip vortices at $t^*=10$; $\circ$ two-vortex wake, $*$ four-vortex wake.

6.7 Wing tip vortices in presence of ground plane

When an aircraft is flying at low altitude, especially during take off and landing, the evolution and development of the wing tip vortices are affected by the presence of the ground. After the full roll-up of the vorticity sheet, both vortices induce each other to move downward as explained in §6.5 until they reach the ground. Then, the force produced by their interaction with the plane causes them to separate and move outward from the aircraft's path. This phenomenon is visualised in Figure 6.26, which shows a SAAB JAS39 Gripen landing on a wet runway. After this initial phase, the behaviour of the vortices becomes very complex due to the separation of the boundary layer from the ground, so they rebound, rise and move along complicated trajectories that are hard to investigate [118].

To simulate the development of wing tip vortices in the presence of a ground plane, the wake was represented by two Lamb-Oseen vortices of equal but opposite initial circulation, and the presence of the ground was modelled by inserting the images of the wing tip vortices, as shown in Figure 6.27. The counter rotating pair is separated by the wing span b and is placed at a distance h from the ground. The Reynolds number for this simulation was set to $\mathrm{Re}=330$, the initial core radius r_c of each monopole to 0.5 so the standard deviation is $\sigma=0.3154$, the wing span $b=2$ and the initial vertical distance from the ground to $h=3$. The evolution of the wake is presented in terms of contour plots of the vorticity in Figure 6.28.

In the early stage of the development, the wing tip vortices move downward due to the induced velocities they exert on each other, while their images move upward with equal velocity until both pairs hit each other. In a real situation this represents the moment when the vortices meet the ground. Then each vortex in the wake pairs with its image and they form new dipoles that move apart horizontally, duplicating the effect of the ground. The trajectories of the wake vortex cores are displayed in Figure 6.29. The path of the image vortices is symmetrical about the x-axis. Hardin

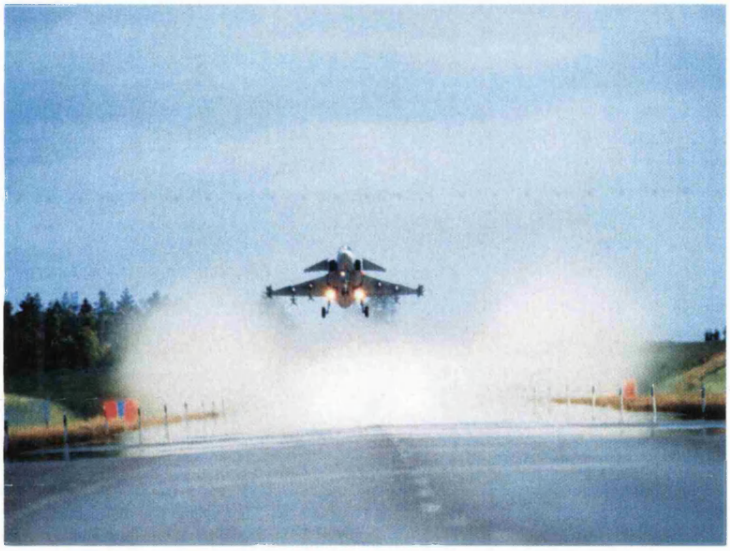

Figure 6.26: A SAAB JAS39 Gripen landing on a wet runway. The outward separation of the wake vortices when they hit the ground is visualised by the foggy cloud over the runway [126].

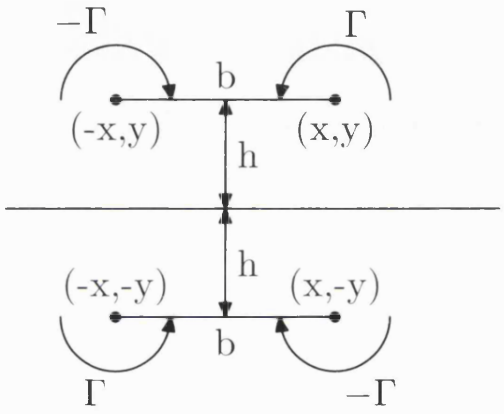

Figure 6.27: Schematic representation of wing tip vortices in presence of ground plane.

and Wang [127] showed in their numerical investigations on this subject that after the vertical descent, the vortices level off with the ground at an asymptotic altitude of $b/2$. The current results agree very well with this conclusion, as the wake is observed to flatten out at $y^*=1$, which is indeed half of the initial wing span. Then, after hitting the ground, the vortices rebound and rise as mentioned by Turk et al. [118].

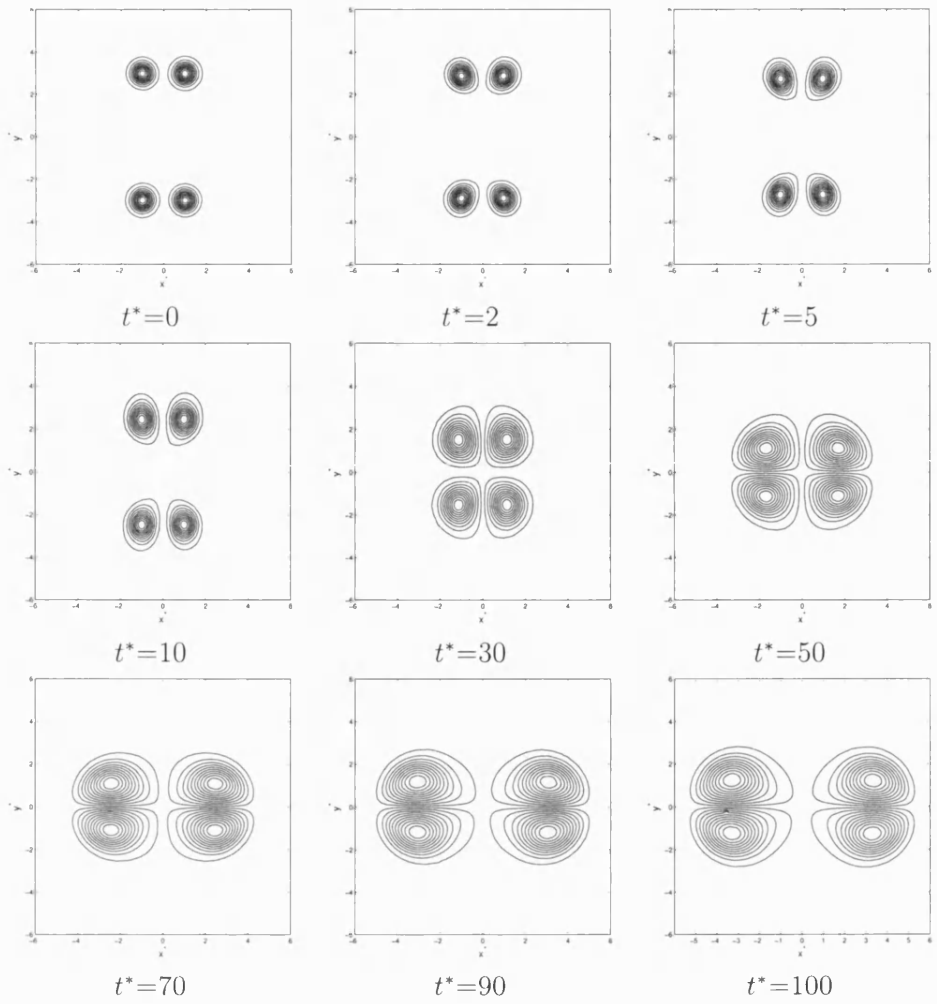

Figure 6.28: Evolution of the wing tip vortices in the presence of a ground plane. The effect of the ground is simulated by inserting the images of the wing tip vortices.

6.8 Conclusions

Newly developed scientific software must pass a crucial test in order to prove its accuracy, reliability and robustness. The credibility of its results is checked in a meticulous examination process, commonly known as validation. However, there is not one test to assess the validity of a numerical algorithm, but various methods are used, depending on the development phase, the performance and level of accuracy needed.

To validate the current code, different techniques were used. In order to check the implementation of the code, the Method of Manufactured Solutions was applied; three different problems for the streamfunction were considered, and for each one different simulations were run with different mesh densities. In all cases, the computed

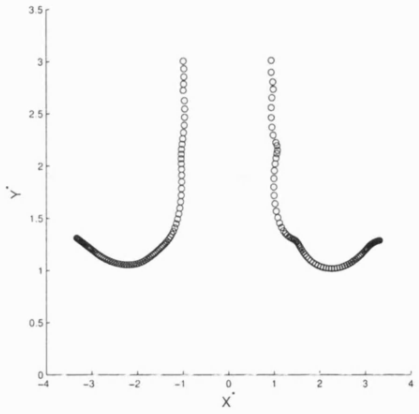

Figure 6.29: The trajectory of the wing tip vortices in the presence of a ground plane.

output matched the theoretical values and refinement of the grid improved the results, confirming the validity of the code. A summary of the tests performed and errors in each one is provided in Table 6.1.

ψ	N	$\epsilon_{\max}$
$x+y$	5458	1.47%
	14520	0.48%
x^2+y^2	8628	3.12%
	9541	2.46%
	13313	2.19%
$e^{-(x^2+y^2)}$	9975	2.94%
	14909	1.67%

Table 6.1: Error behaviour during tests performed using MMS.

Then comparison tests between computed and theoretical values were performed for two fundamental problems in fluid dynamics: potential flow over a circular cylinder and an ellipse. For the latter problem various simulations were run for different aspect ratios and angles of attack. In the cylinder case the maximum error between the velocities was 0.65%, while in the ellipse study the maximum error between the velocities increased with the thickness of the body from 1% to 6.8%, and the maximum error between the streamfunctions stayed nearly constant at around 3.5% for all aspect ratios investigated. For a thickness of 0.5, the results at different angles of attack agreed well with previous studies conducted on the subject. These findings assert the accuracy of the numerical model.

Moreover, the performance of the code was assessed for viscous flows by simulating the development of an isolated Lamb-Oseen vortex, wing tip vortices with and without the presence of the ground and the evolution of a four-vortex wake system. In the first problem, the computed decay and expansion of the vortex matched the

exact analytical solutions, and refinement of the mesh increased the accuracy of the calculations. In the other cases, the outputs of the current simulations were in good agreement with results of published studies on the subjects and natural observations. The performed tests prove that the numerical code developed in this thesis is robust and reliable to be used in further studies.

Chapter 7

Evolution of perturbed Lamb-Oseen vortices

Big whirls have little whirls that feed on their velocity,
and little whirls have lesser whirls and so on to viscosity.

Weather Prediction by Numerical Process, Lewis F. Richardson, 1922

Multipolar vortices play an important role in large scale geophysical flows affecting the transport of mass and energy. Extensive numerical and experimental investigations of the emergence of these structures from monopoles surrounded by counter-rotating vortex rings with zero total circulation have been conducted. This type of monopole is referred to in the literature as a shielded or isolated vortex. Unfortunately, however, the evolution and formation of multipoles from unshielded vortices are still poorly understood. It was previously conjectured by some investigators [128, 129] that a perturbed Gaussian monopole with a non-axisymmetric disturbance will relax to axisymmetry. But Rossi et al. [94] and Barba [96, 104] disagreed with this conclusion and showed that the perturbed vortex decays to a variety of end states depending on the Reynolds number and the distortion magnitude. In order to contribute to the understanding of this subject and to build on the work of Rossi et al. and of Barba, a detailed parametric investigation has been performed on the evolution of perturbed Gaussian distributions with a variety of initial conditions, and their axisymmetrisation, or non-axisymmetrisation, mechanisms have been examined. Barba [104] in her study used the vortex blob method, which limited her ability to study low and high Reynolds numbers. However, due to the advantages of the current method in discretising the vorticity field, the range of Reynolds number investigated was extended to cover cases from $\mathrm{Re}=5\times10^2$ to $\mathrm{Re}=10^5$. The study is also a proof of robustness for the numerical method presented in this thesis.

7.1 Initial conditions

In the current study a perturbed Lamb-Oseen vortex is allowed to decay freely. The initial vorticity field ω is the superposition of a Gaussian distribution ω_G and a disturbance ω', so

$$\omega = \omega_G + \omega', \tag{7.1}$$

where

$$\omega_G = \frac{\Gamma}{2\pi\sigma^2} e^{-r^2/2\sigma^2}, \tag{7.2}$$

$$\omega' = \frac{\delta\Gamma}{2\pi\sigma^2} r^2 e^{-r^2/2\sigma^2} \cos m\theta. \tag{7.3}$$

Thus

$$\omega = \frac{\Gamma}{2\pi\sigma^2} e^{-r^2/2\sigma^2}(1 + \delta r^2 \cos m\theta), \tag{7.4}$$

with

$$r^2 = (x - x_0)^2 + (y - y_0)^2,$$
$$\theta = \tan \frac{y - y_0}{x - x_0}.$$

Γ is the total circulation of the vortex, σ the standard deviation based on the core radius r_c such as σ=0.6308r_c [118], δ the perturbation strength and m the order of the perturbation. Figure 7.1 shows the contours of the base Lamb vortex ω_G, and a quadrupolar and a hexapolar ω'.

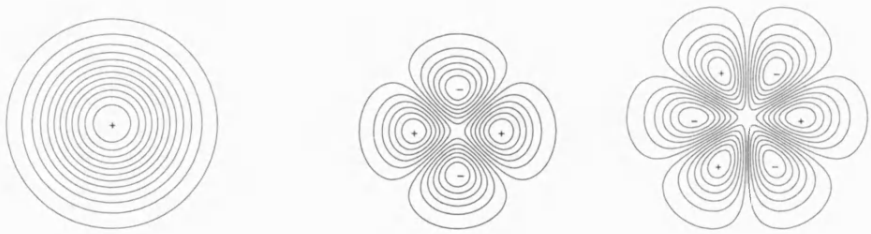

a b c

Figure 7.1: Vorticity contours of the a: base Lamb vortex; b: quadrupolar perturbation; c: hexapolar ω'.

Simulations have been carried out for different values of δ, m and Re=Γ/ν. The flow field is represented as a circular domain of radius r=8 and discretised initially with the following criteria: minimum and maximum triangulation areas are set to $A_{\min}$=0.003 and $A_{\max}$=0.03 respectively and the error tolerance between the specified and the computed values of the vorticity is 10^{-4}. A small tolerance is chosen in

order to have a smooth initial vorticity distribution, which leads to a finer meshing of the non-zero vorticity area compared with the rest of the flow. These parameters are found, after several trials, to give a satisfactory first triangulation, leading to good results. The choice of the initial values is critical in order to get decent results, because a coarse mesh will not have a smooth vorticity distribution, which will affect the evolution and decay of the vortex, while a very fine mesh with small grid spacing leads to numerical instability if any edge length h happens to be smaller than the characteristic length scale $2\nu\Delta t$, as explained in §5.6. This latter limitation can be overcome by building a new algorithm that controls the time step Δt. In the current study, Δt is pre-selected at the start of the simulation and kept constant during it. This means that the characteristic length scale is constant during the whole simulation and an edge length can become at some point smaller than it. However, changing the time step during the calculation depending on the minimum edge length, guarantees the numerical stability of the simulation since Equation 5.28 will always be valid. This approach is worth investigating in future work.

The initial discretisation for a vortex with a quadrupolar perturbation is presented in Figure 7.2. The time step is set to Δt=0.2 and after every six time steps the domain is remeshed imposing the condition that the edge length lie between $h_{\min}$=0.07 and $h_{\max}$=0.3. These values are chosen to keep the triangle areas within the initial range. In all cases, a streamfunction boundary condition was applied, where the outer boundary was set to be a streamline, simulating the wall of a circular tank, as used in experimental studies [79].

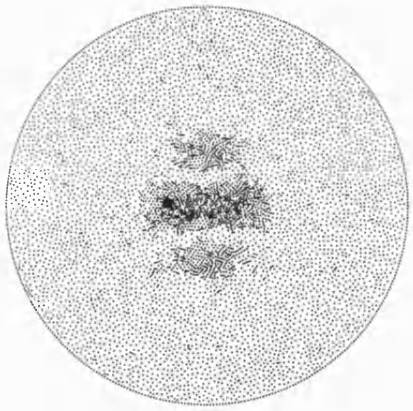

Figure 7.2: The initial discretisation of ω with m=2.

7.2 Decay of an isolated perturbation

Prior to running the model for the perturbed Lamb vortex, the decay of a quadrupolar isolated perturbation centred at the origin of the domain, x_0=y_0=0, was simulated

in order to analyze its evolution and decay. The Reynolds number for this case was $\mathrm{Re}=10^4$, the circulation $\Gamma=1$, the amplitude $\delta=0.05$ and the standard deviation $\sigma=\sqrt{2}$.

The contour plots of ω' are displayed in Figure 7.3 and the vorticity distribution in Figure 7.4 for three different times. It is observed that the disturbance has an equilibrium state and so decays while conserving the symmetry of its four components, both in their shapes and their strengths, while, due to the shear forces that the poles exert on each other, their expansion rate is low. A close inspection of the positions of the centres shows that while expanding the poles push each other and move away, the positive ones horizontally and the negative ones vertically at equal speed. This can be clearly seen in Figure 7.5. The positions of the poles are symmetrical with respect to the centre of the domain $(x_0, y_0)=(0, 0)$, and the small variations observed in the x and y position are due to the discretisation.

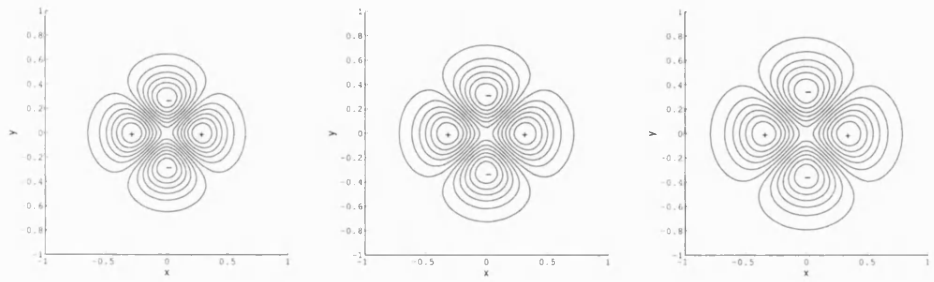

a b c

Figure 7.3: Vorticity ω', $m=2$ at a: $t=0$; b: $t=50$; c: $t=100$.

7.3 Evolution of a Lamb vortex with a dipolar perturbation

An $m=1$ perturbation with strength $\delta=0.25$ was superimposed on a Lamb-Oseen vortex with a standard deviation $\sigma=\sqrt{2}$ and unit circulation for a high Reynolds number, $\mathrm{Re}=10^4$. The number of elements in the domain at $T=0$ was $N_0=6677$ but during the simulation due to remeshing and vorticity expansion it was increased so at $T=1425$ there were $N_f=8330$ points.

Figure 7.6 illustrates the evolution of the initial vorticity field. The first frame shows a dipolar state: the distorted positive Lamb-Oseen vortex was flanked by a smaller and weaker vortex of opposite sign. Due to the difference in intensities, the shear exerted by the dominant vortex was stronger so the satellite stretched and orbited counterclockwise around the centre while having a clockwise rotation itself. This meant that its angular velocity was slower than that of the base vortex, which helped the axisymmetrisation process. At the start the strong vortex was egg-shaped but during the evolution its free elliptical circumference bent to one side and at some point,

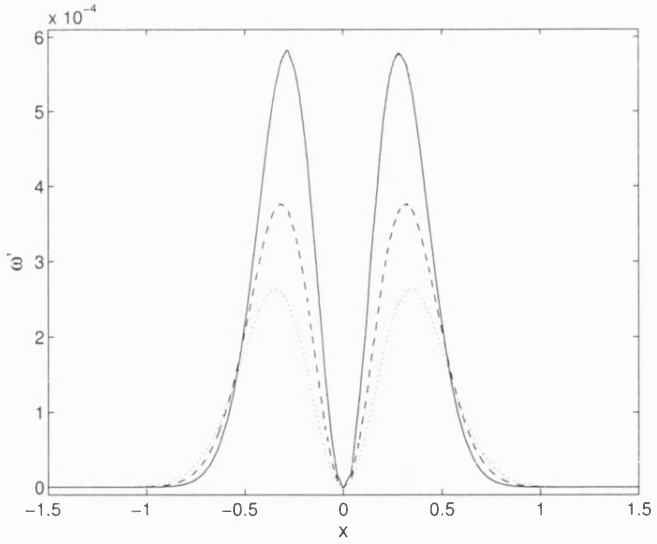

Figure 7.4: Vorticity distribution of the dipolar perturbation at y=0 and t=0 (solid line), t=50 (dashed line), t=100 (dotted line).

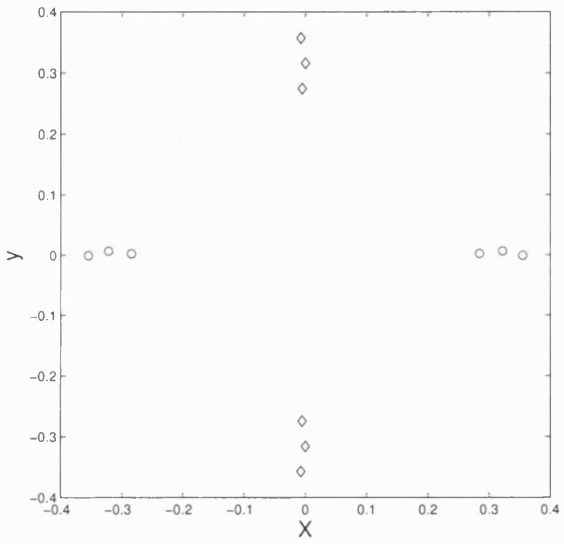

Figure 7.5: Position of the dipolar perturbation poles, ○ positive and ◇ negative during the decay for a time step of Δt=50.

due to the difference in rotation speeds, was squeezed between the centre and the encircling vortex, as seen in frame 7 of Figure 7.6 (T=400). Then the vorticity was compressed into a filament that decayed, turning the Lamb-Oseen vortex back to its base state.

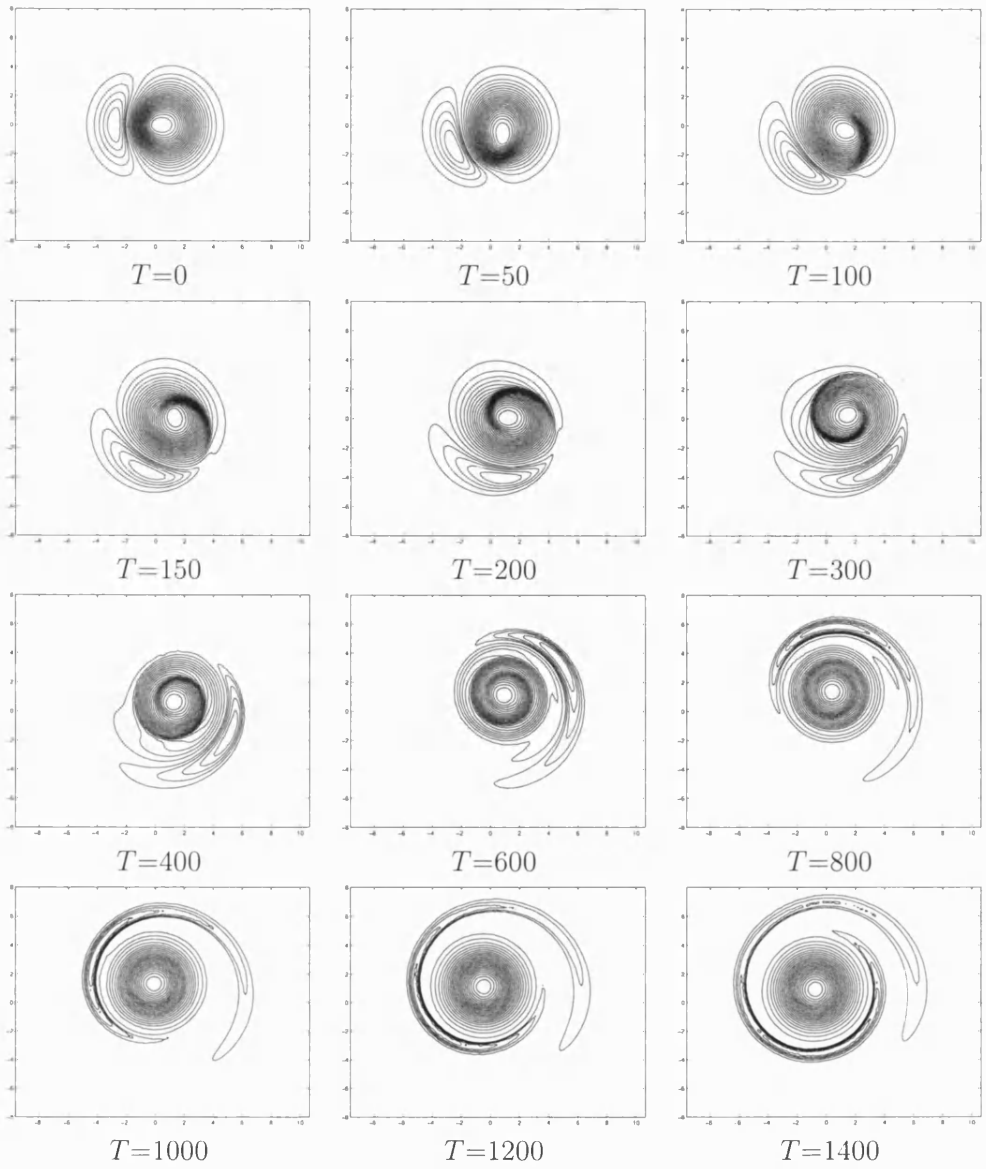

Figure 7.6: Evolution of a Lamb-Oseen vortex with a dipolar perturbation: m=1, Re=10^4 and δ=0.25

The axisymmetrisation of vortices through filamentation was numerically studied by Melander et al. [71]. They showed that the edges of an isolated elliptic vortex developed during its rotation into filaments that broke the elliptical symmetry and activated an "axisymmetrisation principle" on the structure. In the current study the core of the main vortex started to become circular even before the formation of the filament but axisymmetry was not reached until its total decay. It is well known that an unper-

turbed Gaussian monopole rotates with zero linear momentum. However, in this case the shear exerted by the companion vortex while stretching affected the position of the principal one as shown in Figure 7.7. Primarily, the base vortex drawn by the weak one

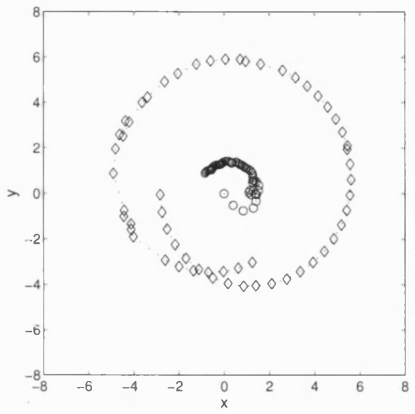

Figure 7.7: Positions of the centre of the main vortex ($\circ$) and of the satellites ($\diamond$) during the evolution of the Lamb-Oseen vortex with a dipolar perturbation at different time steps Δt=25. Both vortices rotate counterclockwise.

travelled downward at a fast pace, then after a reorganisation phase rotated slowly on a circular course. This movement matched that of the satellite, which first moved down on an elliptical trajectory due to the shape of the main vortex, then assumed a circular path due to the effect of the axisymmetrisation mechanism on the centre before being drawn closer to it as the filament separating both vortices diminished and disappeared. This is manifested by the sudden displacement of the centre of the satellite as observed on the left hand side of Figure 7.7.

The change in trajectory and speed of the positive vortex might be due to the decreasing intensity of the small vortex during its revolution. The decay of the negative vorticity is displayed in Figure 7.8 on a logarithmic time scale, which helps to see clearly the early stages of the process. Consequently, its effect is apparent from the development of the ratio $\omega_{\max}/\omega_{\min}$ in Figure 7.9. Initially, the magnitude of the side vortex was strong enough to draw its partner towards it ($|\omega_{\max}/\omega_{\min}|$=7.4), and the slow diminution phase observed in the decay curve coincides with the early fast displacement of the main vortex. But as the slope of the declination steepened, the effect of the negative satellite weakened, which slowed down the rotation of the central vortex. Finally, it is worth remarking that during the evolution the satellite degenerated without mixing with the Lamb vortex, and based on its rotation and decay rate it is expected that it will stretch even further becoming a thin filament that will gradually vanish due to viscous effects leaving the axisymmetric monopole as the end state.

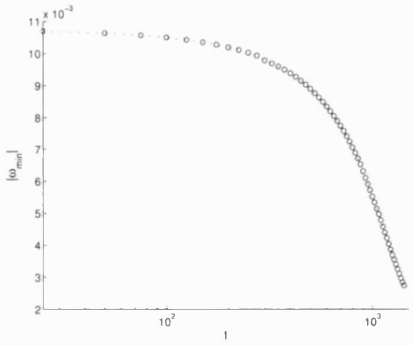

Figure 7.8: Decay of the satellite (m=1) on a logarithmic time scale.

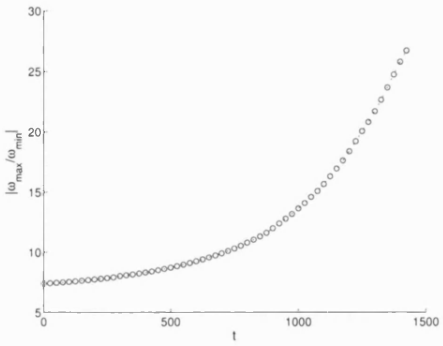

Figure 7.9: Absolute value of $\omega_{\max}/\omega_{\min}$ during evolution of the perturbed vortex: m=1, Δt=25.

7.4 The tripole

The Lamb-Oseen vortex was perturbed by a quadrupolar nonlinear distortion, and the effect of perturbation amplitude and Reynolds number on the evolution of the base vortex was investigated. The results are shown in the following subsections.

7.4.1 Formation and evolution

In this stage of the study, the base vortex with Γ=1 and $\sigma^2 = 2$ was distorted by a quadrupolar perturbation, m=2. Different simulations were carried out for various Reynolds numbers and perturbation amplitudes. Since it was previously found that two-dimensional cyclonic and anticyclonic vortices behave similarly [75], no tests were done with a negative vorticity centre and positive side blobs. The initial condition, the first frame of Figure 7.10, could be considered a tripole but as the simulations show it is not a steady state. The evolution of the initial tripolar structure has been discussed in the literature and it was found that it either decayed to an axisymmetric monopole or to a quasi-steady rotating tripole, depending on the perturbation ampli-

tude δ and the Reynolds number Re. A quasi-steady vortex is defined as one that keeps its vorticity distribution for some time while decaying solely due to viscous diffusion. As conjectured by Le Dizès [95] and observed by Barba and Leonard [96], the present results prove that the critical perturbation strength δ_{critical} that separates the monopolar and tripolar attractors, increases as Re decreases. For high Reynolds numbers a small δ is sufficient for the disturbed vortex to form a rotating tripole. However for high viscosity (low Re) the Lamb-Oseen vortex needs to be highly perturbed in order to relax into a tripole, otherwise it decays back to its base state.

It was also found that even the quasi-steady tripole tends to assume axisymmetry as its asymptotic state. Figures 7.10 and 7.11 depict schematically the evolution of a perturbed vortex with δ=0.2 and 0.35 respectively at Re=10^3. In the small dis-

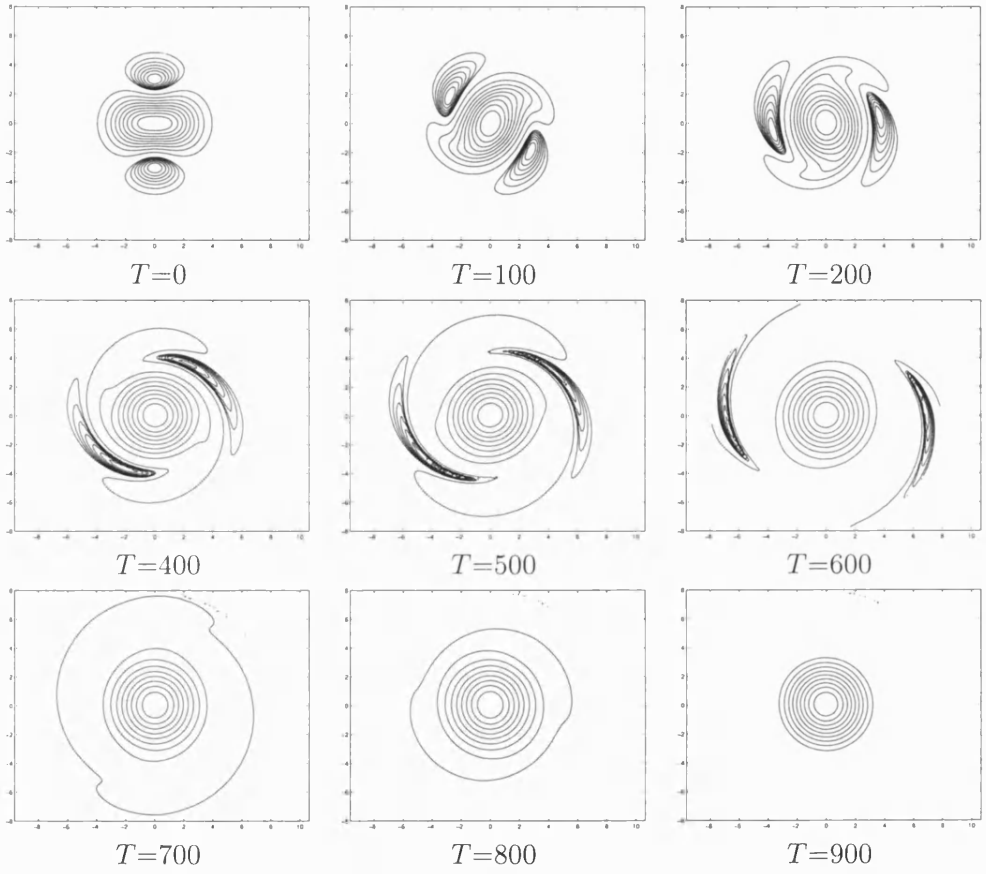

Figure 7.10: The relaxation of a perturbed Lamb-Oseen vortex into a monopole: m=2, Re=10^3, δ=0.2. Initially the satellites are represented by 8 equally spaced contours of vorticity and the core by 10.

turbance case, the side negative blobs stretch around the core into thin filaments that vanish leaving an axisymmetric monopole. However, in the latter figure a tripole is observed to emerge after a reorganisation period. The squeezed centre expands and

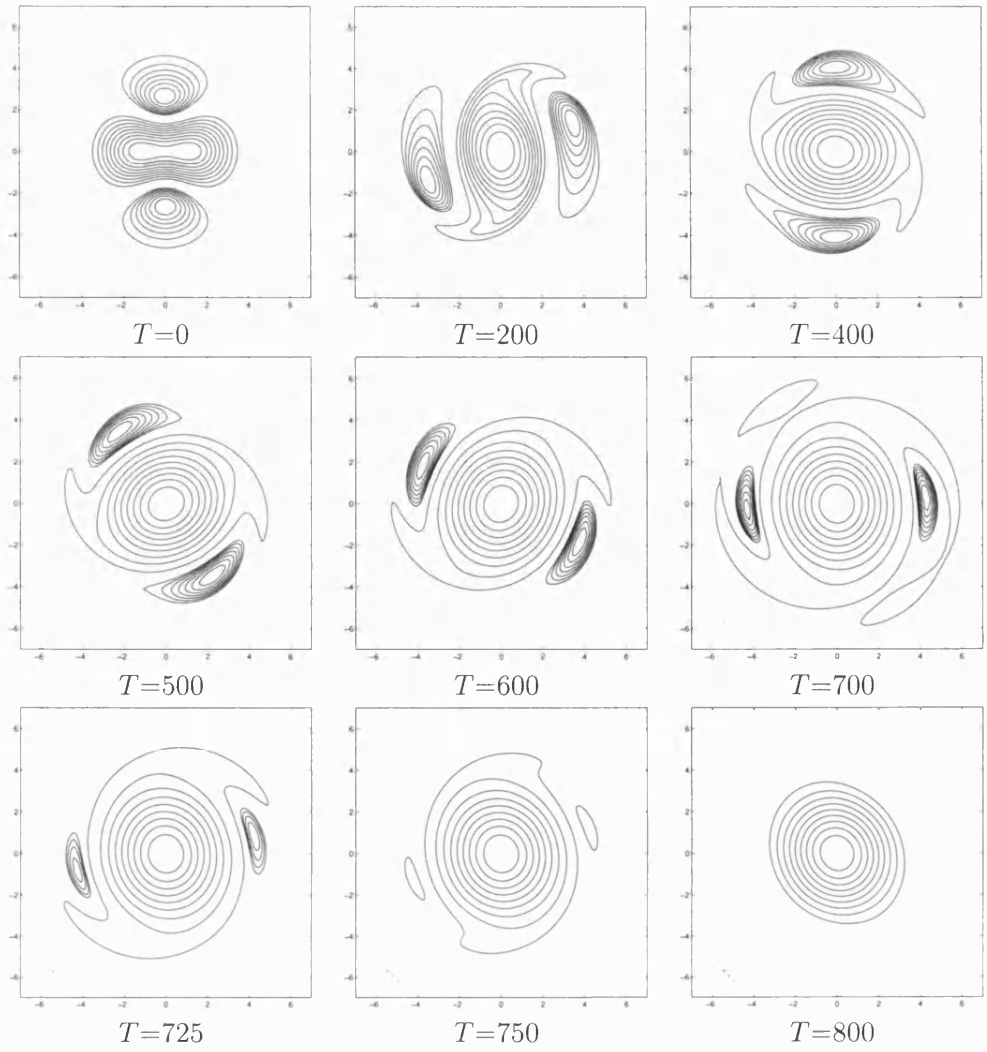

Figure 7.11: Contour plots of the relaxing perturbed vortex: m=2, Re=10^3, δ=0.35. The satellites are represented by 8 equally spaced contours of vorticity and the core by 10.

the two side satellites take on an elliptical shape while the whole structure rotates as a solid body around its central axis in the same direction as the core rotation. Due to viscous effects, the satellites diminish with time leading to a monopolar end state.

Increasing the value of δ results in larger and stronger satellites that live longer. In order to better visualize changes in the flow topology during the development process, the gray-scale contour levels of the logarithm of the absolute value of vorticity for δ=0.2 and δ=0.35 at Re=10^3 are plotted in Figures 7.12 and 7.13. Zero vorticity is emphasized by superposing the zero contour line on the plots. This line marks the boundary where ω changes sign. In the former figure it can be seen that the sides

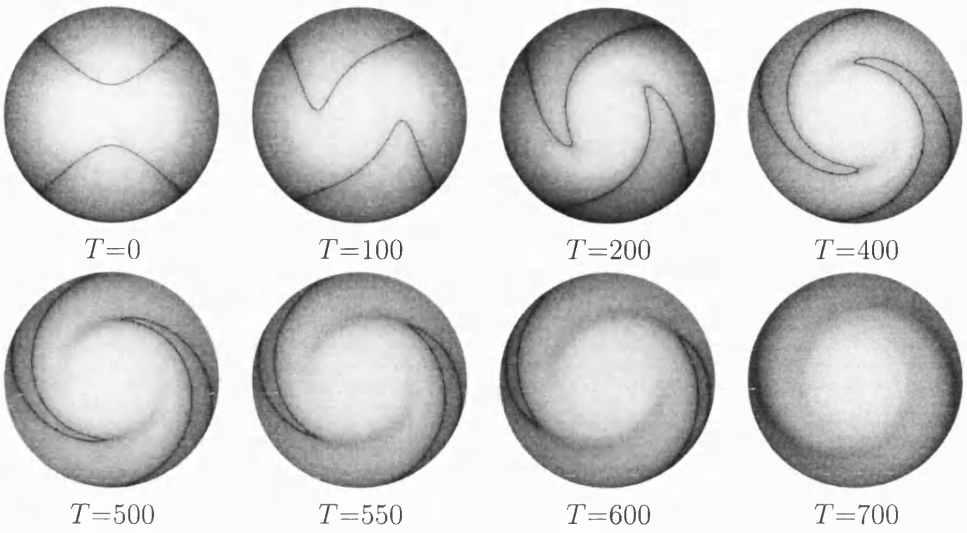

Figure 7.12: Gray scale plots of $\log|\omega|$ and zero level contour lines: m=2, Re=10^3, δ=0.2.

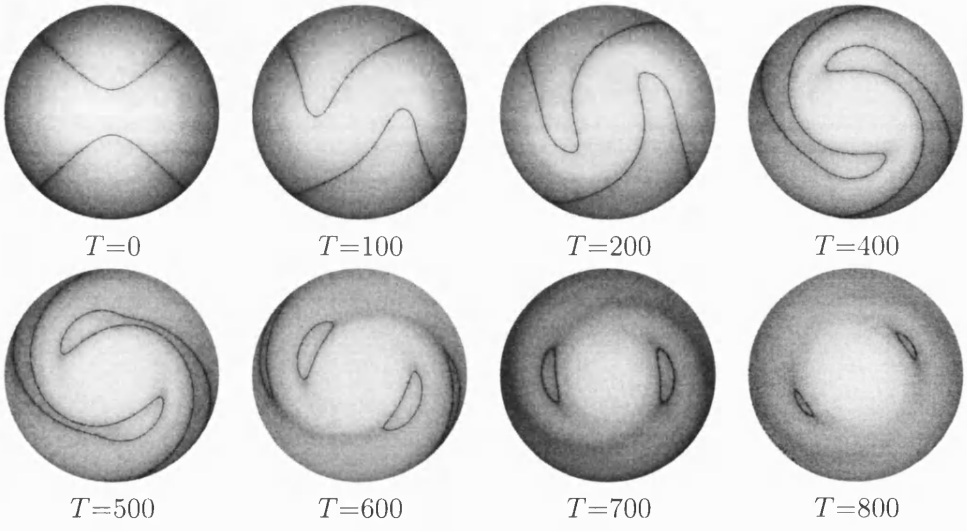

Figure 7.13: Gray scale plots of $\log|\omega|$ and zero level contour lines: m=2, Re=10^3, δ=0.35.

form thin filaments and decay as they rotate, pushing the negative vorticity region far away from the centre, which relaxes towards axisymmetry as seen in the last frames of Figure 7.10. However, Figure 7.13 clearly displays the emergence of the quasi-steady tripole. Since in this case δ is large, the negative blobs stretch around the centre in wide filaments and, as observed at $T \simeq 500$, the zero contour lines enclose two regions of negative vorticity while the rest of the filaments quickly vanish, forming two isolated

satellites around the core that degenerate with time. This mechanism was described by Barba and Leonard [96] as the "pinching" of the zero contour levels where they reported it for Re=10^4 and δ=0.25.

The effect of changing δ on the emergence of the tripole is illustrated in Figures 7.14 and 7.15 where Re=10^3 and δ=0.25, 0.3 respectively. Comparing these figures

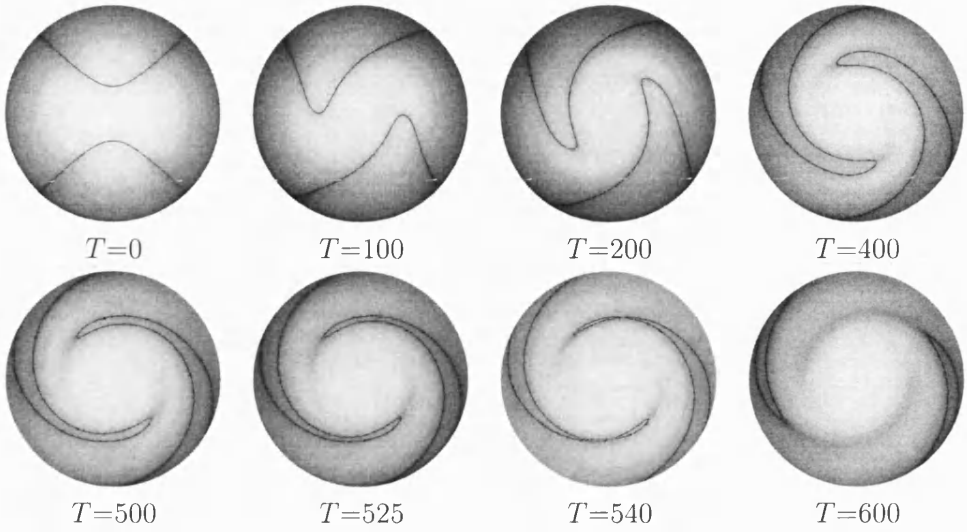

Figure 7.14: Gray scale plots of $\log|\omega|$ during the evolution of the perturbed Lamb vortex: m=2, Re=10^3, δ=0.25.

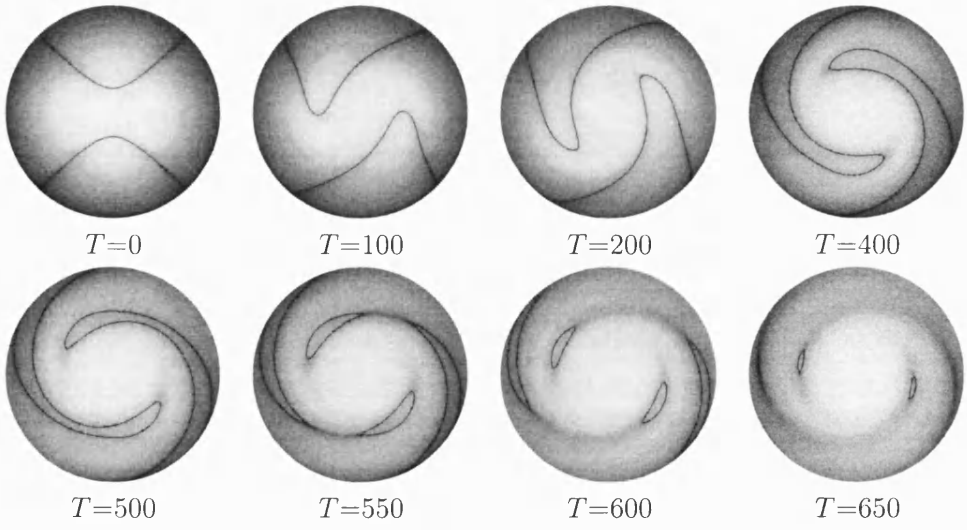

Figure 7.15: Gray scale plots of $\log|\omega|$ during the flow development: m=2, Re=10^3, δ=0.3.

with Figures 7.12 and 7.13, it is evident that a larger δ leads to the central vortex

being initially more squeezed and the side vortices becoming wider and more stretched as they revolve around the core before forming the satellites. Moreover, increasing δ accelerates the pinching process and increases the area of the enclosures, so the satellites appear at an earlier time with stronger magnitudes, thus increasing the life span of the emerged tripole. However, the angular velocity of the structure, $\Omega_{\text{structure}}$, in the early stages of flow evolution seems to be constant for all cases and not affected by δ. This can be explained by the fact that $\Omega_{\text{structure}}$ is defined by the maximum vorticity of the central vortex, $\Omega_{\text{structure}}=\omega_{\max}/2$, and since initially the maximum vorticity is equal for all cases, $\omega_{\max}(0)=1/4\pi$, so the rotation rate is constant. As a result, the initial turn-over time, $\tau_0=4\pi/\omega_{\max}(0)$, for all vortices is equal to $\tau_0 \approx 158$.

Rossi et al. [94] and Barba et al. [37] simulated the same initial vorticity distribution using different numerical methods. A comparison between both results at $T=500$ and $\delta=0.25$ can be found in [37]. At high Reynolds numbers, 5×10^3 and 10^4, the decay of the tripolar vortex was similar, but for $\text{Re}=10^3$ Rossi et al.'s simulation showed more erosion of the tripole. Barba et al. concluded that their method is more accurate and that the difference in the results is due to numerical errors in the method used in [94]. Unfortunately, in both papers the time evolution of the tripole for $\text{Re}=10^3$ with various perturbation amplitudes was not shown to compare it with the present results. However Rossi et al. briefly mentioned that for $\text{Re}=10^3$ and $\delta=0.25$ the negative enclosures had completely disappeared at $T=600$, in agreement with the last frame of Figure 7.14.

Barba and Leonard [96] showed in Figure 1 of their paper the relaxation over time of the perturbed vortex into a quasi-steady tripole for $\delta=0.25$ and $\text{Re}=10^4$. In order to compare the results obtained using the method developed in this thesis with theirs, the same case is simulated and the contour levels of the relaxing perturbed Lamb vortex are presented in Figure 7.16. The vorticity was normalized by $\omega_{\max}(0)$ and represented by 14 equally spaced contours as in [96]. The results compare well in terms of the shape of the decaying structure with those of Barba and Leonard. However, in the present simulation the angular velocity and the decay rate are slower than theirs. In [96] the pinching of the zero contour level took place at $T=580$, in contrast to the current results where the negative inclusions appear at around $T=650$ as displayed in Figure 7.17. This indicates that the stretching and the decay of the negative side blobs are faster in Barba and Leonard's simulation. This difference might be attributed to the improvement of accuracy in the current method compared to the core spreading method used by Barba and Leonard, which requires good core sizes and blob overlap to represent accurately the vorticity field. Once the spatial distribution of the blobs is distorted, some details of the vorticity diffusion are missed. Barba and Leonard [96] admitted that substantial development is needed to improve the code efficiency. This limitation is surmounted in the current method where triangulated nodal points discretise the vorticity field. The triangulation is updated at every time step, which ensures the accuracy of the vorticity distribution. For this case, $\delta=0.25$ and $\text{Re}=10^4$, the tripole survived for a long time before relaxing into a monopole in agreement with Barba and Leonard's observations. Figure 7.18 illustrates the long time evolution of the tripole up to $T=3000$.

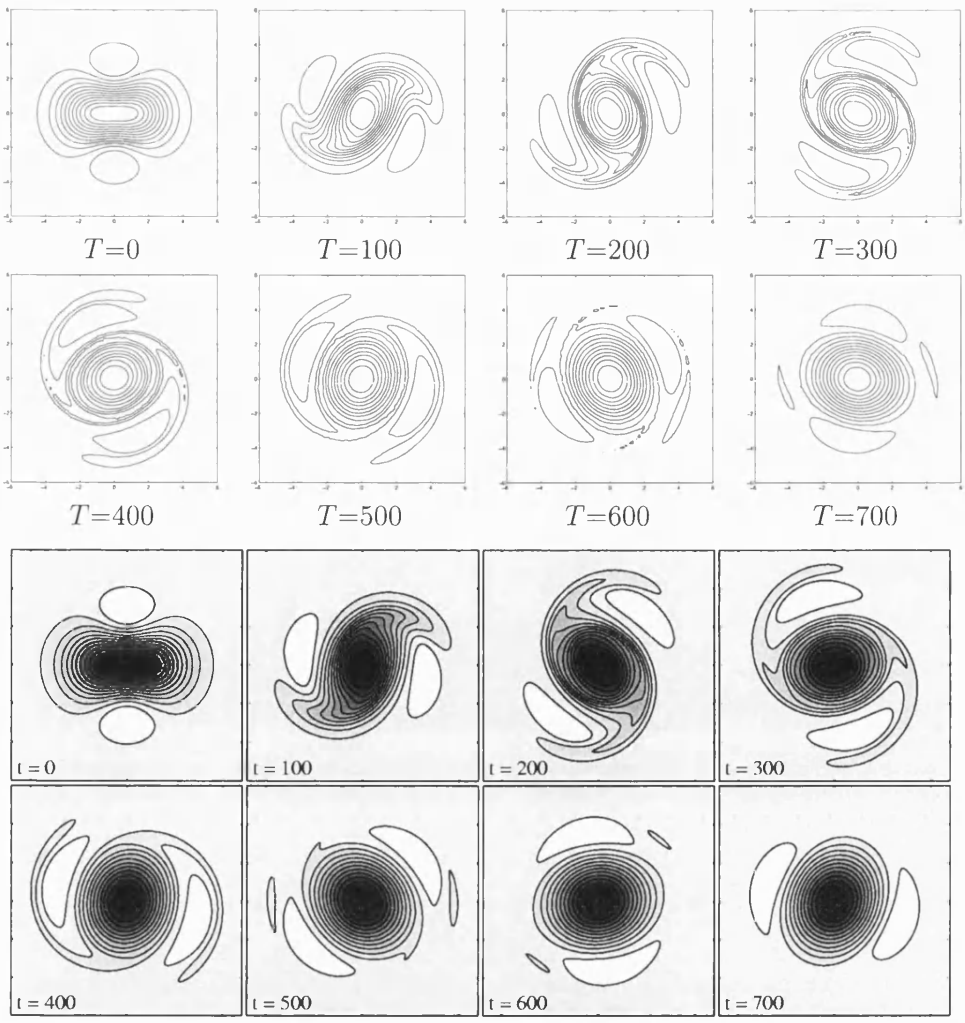

Figure 7.16: The contour plots of the relaxing tripole at $\mathrm{Re}=10^4$, $\delta=0.25$. 14 equally spaced contours of vorticity normalized by $\omega_{\max}(0)$. Top two rows: current results, bottom two rows: Barba and Leonard's results, reproduced from Reference [96] with permission.

7.4.2 The effect of Re on the emergence of the tripole

As mentioned previously, the higher the Reynolds number, the easier it is for the perturbed Lamb-Oseen vortex to relax into a tripole. So far in the literature the maximum Re studied is 3×10^4 by Barba and Leonard [96] who could not consider higher values due to the limitations of their method. They also could not easily study very low Re cases for the same reason. However, using the current method the decay of perturbed vortices at $\mathrm{Re}=5 \times 10^2$ and $\mathrm{Re}=10^5$ could be studied without facing great difficulties.

For very low and large Re, Barba and Leonard encountered computational diffi-

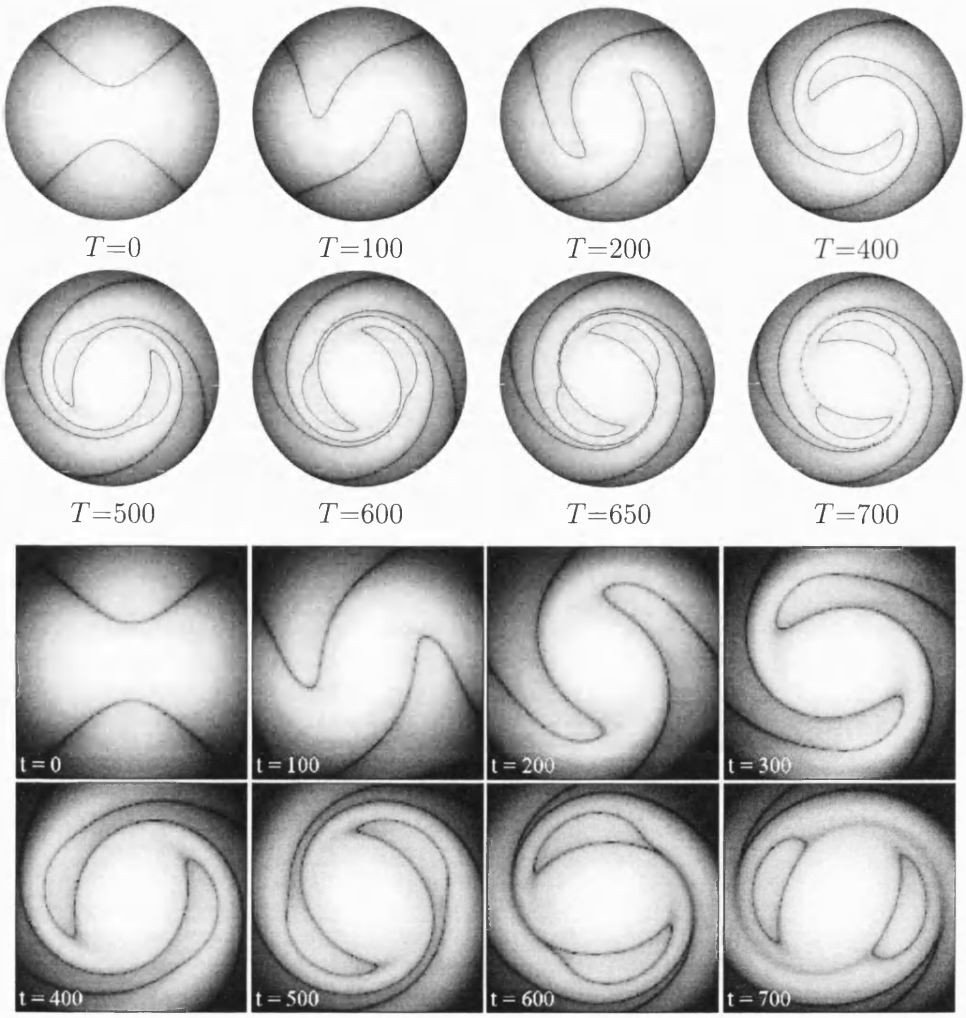

Figure 7.17: Gray scale plots of $\log|\omega|$ during the flow evolution: m=2, δ=0.25, Re=10^4. The vorticity was normalized by $\omega_{\max}(0)$. Top two rows: current results, bottom two rows: Barba and Leonard's results, reproduced from Reference [96] with permission

culty concerning the required CPU time and memory allocation due to the limitation of their method. In order to increase the resolution of their calculation, their method required constant spatial adaptation because it is based on core spreading. So the adjustment of the core sizes and the superposition of the vorticity blobs, which is carried out to ensure a smooth vorticity distribution, augmented the number of particles in the computational domain. This limitation is overcome in the current method where the vorticity field is represented by nodal points and not vortex blobs, so there is no need for frequent spatial adjustment to guarantee the overlapping of the blobs. Figure 7.19

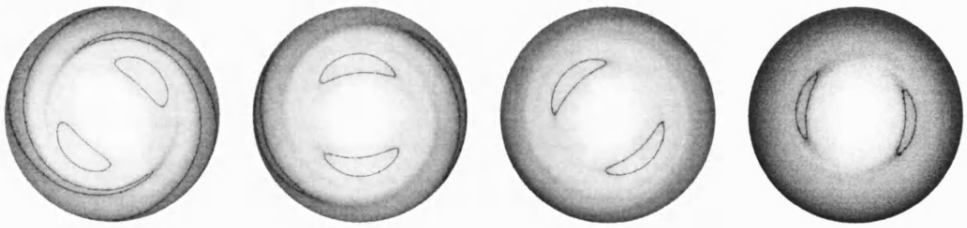

Figure 7.18: Gray scale plots of $\log|\omega|$ showing the long time evolution of the tripole: δ=0.25, Re=10^4, vorticity normalized by $\omega_{\max}(0)$.

shows the variation with time of the number of points N in the computational domain for δ=0.2 at four different Reynolds numbers: 5×10^2, 10^3, 10^4 and 10^5. In the early

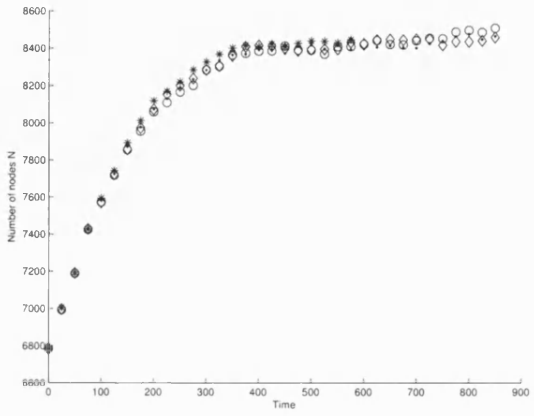

Figure 7.19: Number of points N in the computational domain against time for m=2, δ=0.2; $*$: Re=5×10^2, $\bullet$: Re=10^3, $\circ$: Re=10^4 and $\diamond$: Re=10^5.

stages of the simulation, the number of points discretising the flow field increases due to vorticity dissipation but later tends to reach an asymptotic value as the structure decays towards axisymmetry. It is apparent that Re does not have an effect on the number of points, since N is nearly equal and behaves similarly in all cases.

To assess the effect of the Reynolds number on the emergence of tripoles, four simulations were run with an equally perturbed vortex, δ=0.2, at Re=5×10^2, 10^3, 10^4 and 10^5. Figure 7.20 presents the results of the latter two tests. Comparing this figure with Figure 7.12, it is obvious that for larger Re the initial tripolar structure decays into a quasi-steady tripole whereas, as previously discussed, for Re=10^3 it relaxes directly into an axisymmetric monopole. When the viscosity is large, the decay rate of the negative vorticity is faster than the wrap up of the zero contour line, so satellites do not form. However, as the viscosity decreases the decay rate becomes slower, thus the negative vorticity patches live longer allowing the zero contour line to enfold and form a tripolar vortex. For the same reason, when comparing the new structure, for example

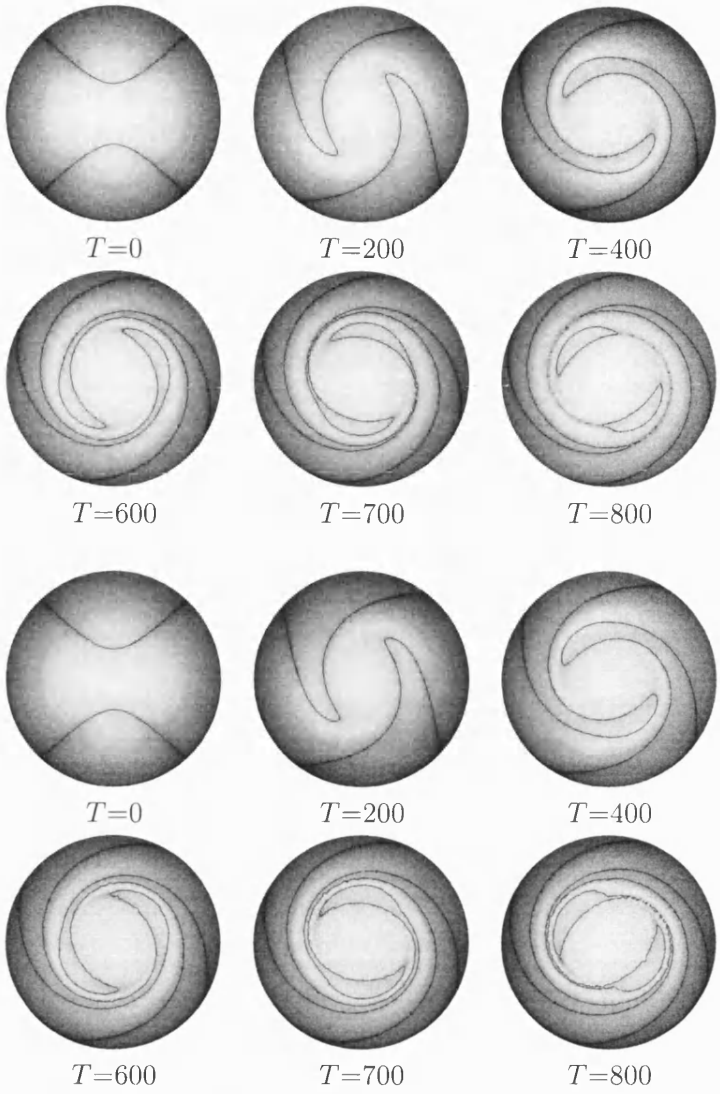

Figure 7.20: Gray scale plots of $\log|\omega|$ during the relaxation of a perturbed Lamb-Oseen vortex: m=2, δ=0.2, top two rows Re=10^4, bottom two rows Re=10^5.

at T=800 in Figure 7.20, one can notice that the satellites are larger for higher Re: as a result the tripole is expected to last longer.

The contour plots of the vorticity for δ=0.2 are displayed in Figure 7.21 for Re=5×10^2 and Figure 7.22 for Re=10^4 and 10^5. The Reynolds number does not change the angular velocity of the vortex structure as this is observed to rotate at the same speed in all cases. As explained in §7.4.1, this is due to $\omega_{\max}(0)$ being constant. However, the effect of Re on the vorticity decay is clearly visible. At Re=5×10^2 the viscous dissipation is important so the whole structure decays quickly; the negative sides dis-

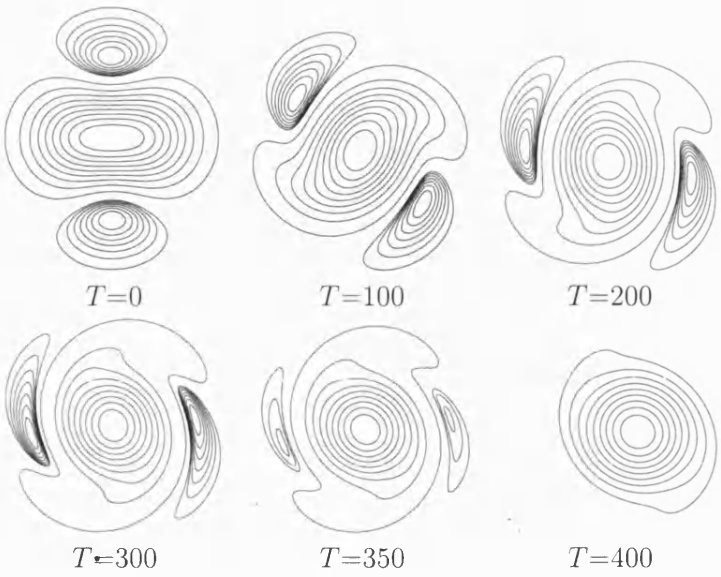

Figure 7.21: Evolution of a perturbed Lamb vortex: m=2, δ=0.2, Re=5×10^2.

appear completely before T=400 and, in contrast to the higher Reynolds numbers, in this case the core vortex does not develop filaments from its elliptical sides because the decay rate is faster than the stretching rate. On the other hand, at Re=10^5 viscosity is weak so the decay rate is slow, which gives plenty of time for the central vortex to form thin filaments that encircle the satellites. The vorticity in this case erodes with time, leaving small patches.

It can be observed in the last two frames of Figure 7.21 that small patches of vorticity start to build up on the grid periphery. When the viscosity is large, viscous spreading transports the vorticity towards the grid boundary where it cannot dissipate further, thus numerical errors develop. In order to overcome this instability, the grid can be expanded allowing extra domain for the dissipation. However, for large Re the decay is slow thus it takes longer for the vorticity to reach the outer boundary. This is why no numerical error is visible in Figure 7.22.

To illustrate how the Reynolds number affects the evolution of the tripolar structure, the quantity $|\omega_{\min}/\omega_{\max}|$ was plotted versus the initial disturbance magnitude δ for various Re at T=600 in Figure 7.23. This time corresponds to nearly four turn-over times, $T \approx 4\tau$, which is enough for the flow to complete its reorganisation phase [96]. Each marker in the plot indicates one simulation. The ratio $|\omega_{\min}/\omega_{\max}|$ determines the magnitude of the satellites with respect to the core intensity indicating the axisymmetrisation state of the tripole. Once the negative vorticity has completely disappeared the ratio becomes zero. The visualization of the vorticity indicates that the tripole exists as long as $|\omega_{\min}/\omega_{\max}| \geq 10^{-2}$, otherwise the negative vorticity is mixed in the core vortex that relaxes into a monopole. The sharp jump in the curve at Re=10^3 clearly displays the separation between two states, the monopole and the tripole, at the dif-

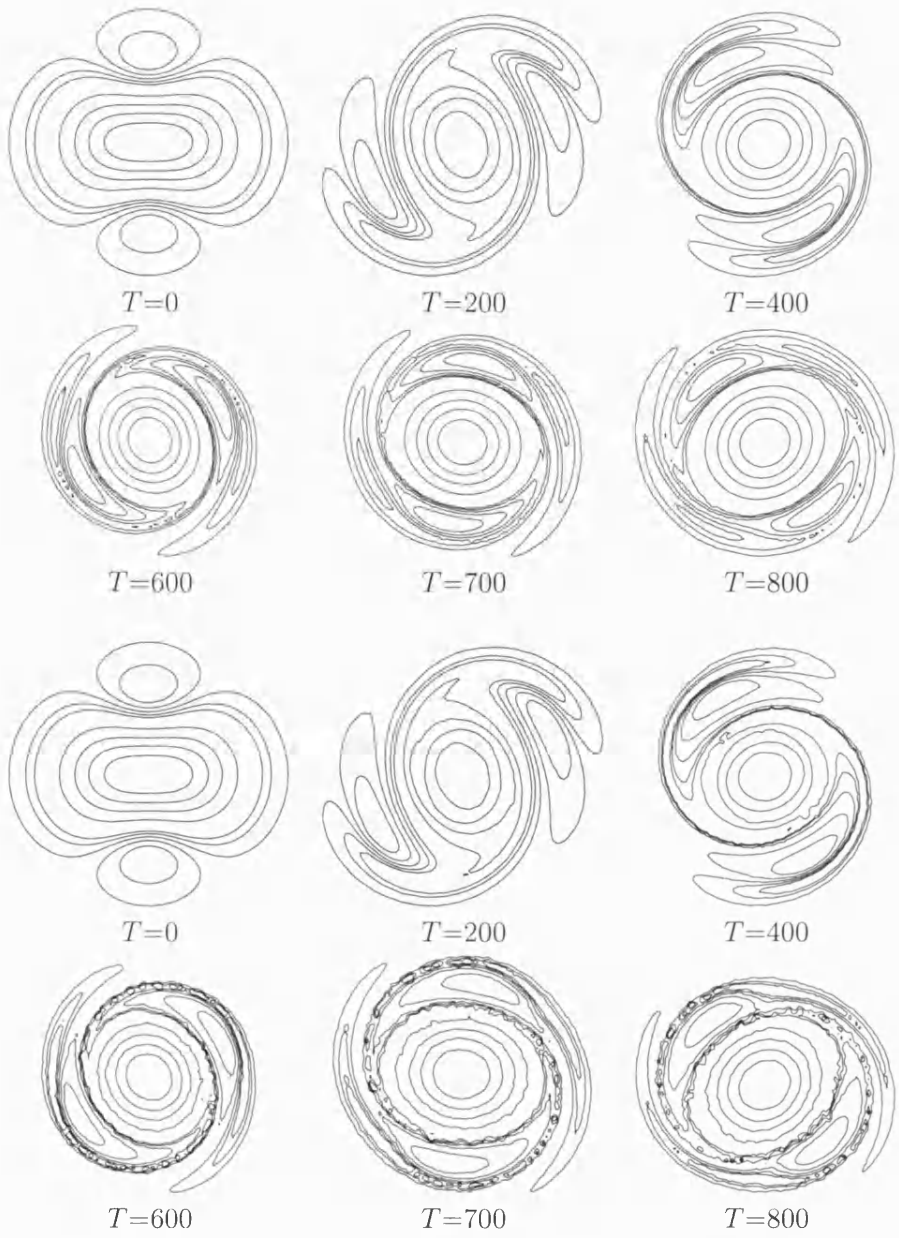

Figure 7.22: Vorticity evolution of a perturbed monopole: m=2, δ=0.2, top two rows Re=10^4, bottom tow rows Re=10^5.

ferent values of δ, whereas at higher Re the curves are still smooth indicating that the mixing of the negative vorticity is not yet completed. Figure 7.23 agrees qualitatively with a similar plot showing the same quantities presented by Barba and Leonard [96], Figure 7.24, but shows slower decay than their results.

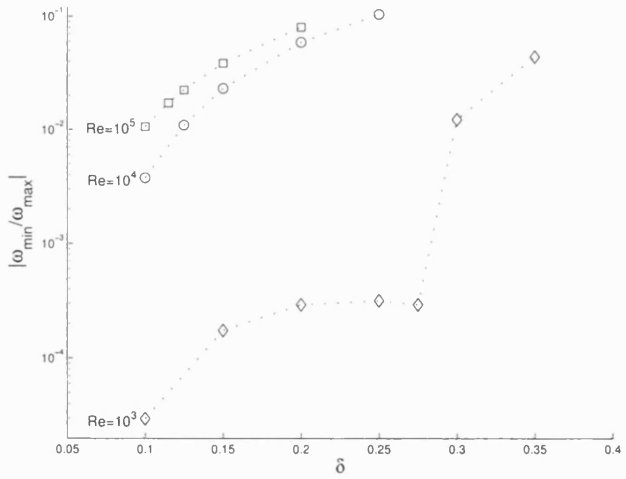

Figure 7.23: $|\omega_{\min}/\omega_{\max}|$ in tripoles versus initial perturbation amplitude δ at T=600; $\diamond$ Re=10^3; $\circ$ Re=10^4; $\square$ Re=10^5.

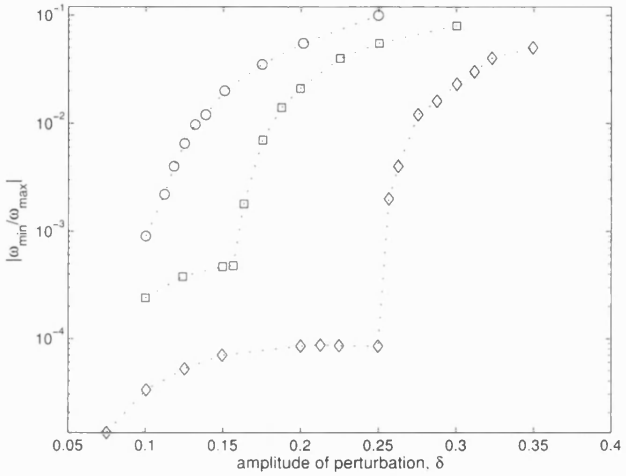

Figure 7.24: Ratio of minimum to maximum vorticity versus initial δ for 37 simulations at T=600. $\diamond$ Re=10^3; $\square$ Re=3×10^3; $\circ$ Re=10^4. Data reproduced from Reference [96] with permission.

The effect of the Reynolds number on the mixing and decay of the satellites with time at various initial δ is shown in Figures 7.25—7.27 for respectively Re=10^3, 10^4 and 10^5. In the first two figures the drastic drop observed in the value of $|\omega_{\min}/\omega_{\max}|$ at a given δ signals the fast disappearance of the side blobs and the axisymmetrisation of the perturbed vortex back to its base state. However, at larger perturbation amplitudes, the slow decrease in the value of $|\omega_{\min}/\omega_{\max}|$ coincides with the enclosing of the negative vorticity and the emergence of the quasi-steady tripole. Once it is formed, the tripole relaxes slowly towards axisymmetry, so the sharp drop does not occur until

the satellites completely vanish. An example of this is visualized in Figure 7.28 for δ=0.15 and Re=10^4. In Figure 7.26 at this perturbation a small decay in the value of $|\omega_{\min}/\omega_{\max}|$ can be seen between T=800 and T=1000, which corresponds to the diminution of the satellites between these two times, frames 2 and 3 in Figure 7.28. On the other hand, between T=1000 and T=1200 the satellites die out leading to a quick decline in the ratio $|\omega_{\min}/\omega_{\max}|$. The speed of mixing of the negative vorticity into the core vortex and the critical perturbation amplitude for the formation of the tripole depend on the viscosity as the axisymmetrisation of the perturbed vortex accelerates and δ_{critical} increases once Re decreases, which is expected due to the increase of viscous diffusion. At Re=10^5 the viscous effects are weak so the decay happens on a slow time scale due to mixing, thus no sudden drop is observed, even at the very small amplitude δ=0.1.

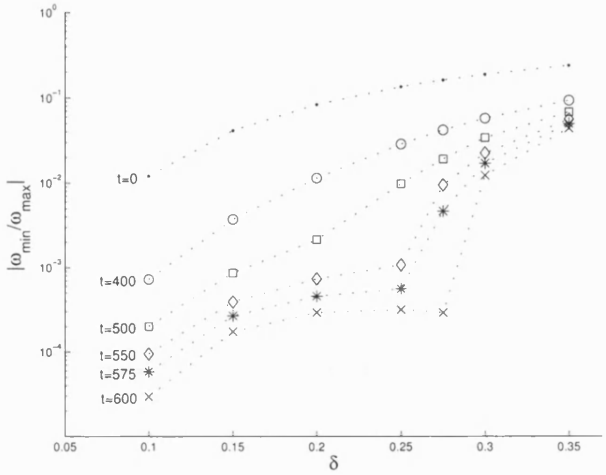

Figure 7.25: Decay of a tripole, $|\omega_{\min}/\omega_{\max}|$, versus initial δ at various times: Re=10^3.

7.4.3 The decay of the tripolar structure

Rossi et al. [94] studied the decay of the perturbed Lamb-Oseen vortex at three different Reynolds numbers, 10^3, 5×10^3 and 10^4, but for only one δ=0.25, and observed that after an initial reorganisation period the structure in all three cases relaxed in a similar manner on a t/Re scale. Thus they concluded that the tripole relaxes slowly on a viscous timescale. However, Barba et al. [37] disagreed with this conclusion since their results for the same perturbation amplitude showed that the decay rate increased with the Reynolds number. They explained this difference by the increased numerical dissipation in Rossi's method and the greater accuracy of their method. Indeed, Rossi et al. acknowledged their inability to capture the shear-diffusion mixing in the tripole, which they blamed partly on the numerical errors in their simulation.

In a later paper, Barba and Leonard [96] addressed the question of shear-diffusion in the relaxation of the tripole and found that only at small perturbation strengths does

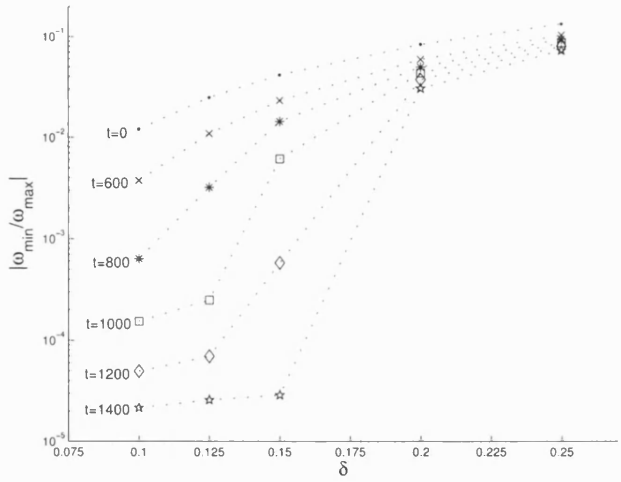

Figure 7.26: Decay of a tripole, $|\omega_{\min}/\omega_{\max}|$, versus initial δ at various times: $\mathrm{Re}{=}10^4$.

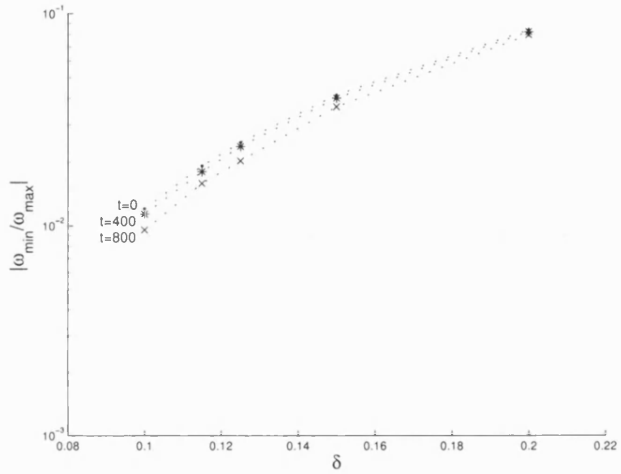

Figure 7.27: Decay of a tripole, $|\omega_{\min}/\omega_{\max}|$, versus initial δ at various times: $\mathrm{Re}{=}10^5$.

the decay of the structure scale well on a shear-diffusion time scale ($t/\mathrm{Re}^{1/3}$). They justified this by the fact that at small δ nonlinear effects are not important, thus shear-diffusion, which is a linear mechanism, is predominant.

In order to contribute to the understanding of the decay process of the tripole, it is further studied for various Re and δ. To compare the current simulation outputs with those of [94] and [37], $|\omega_{\min}/\omega_{\max}|$ is plotted against the viscous time scale, t/Re, for three different perturbation amplitudes, 0.15, 0.2 and 0.25, at three Reynolds numbers, 500, 10^3 and 10^4, in Figure 7.29. The results obtained prove that the relaxation rate increases with the Reynolds number on the Re^{-1} scale, supporting the findings of Barba et al. [37] that the tripole does not decay on a viscous time scale as suggested

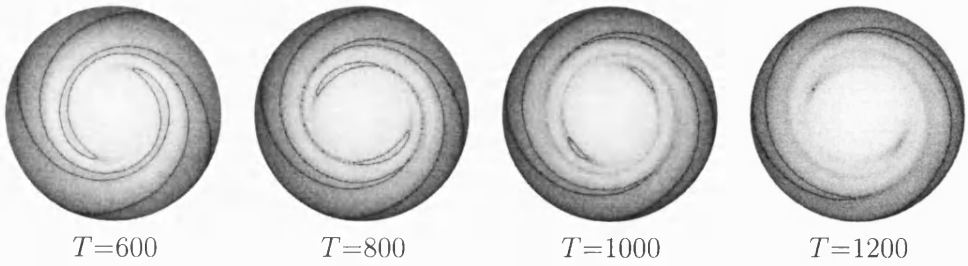

Figure 7.28: Gray scale plots of $\log|\omega|$ during late stage decay of the tripole: $\mathrm{Re}=10^4$, $\delta=0.15$.

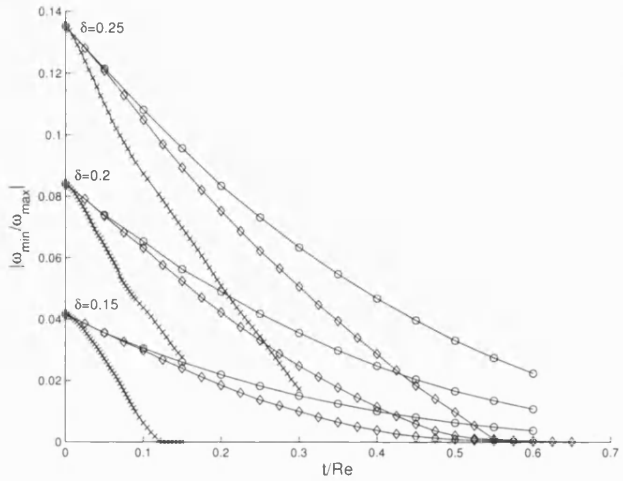

Figure 7.29: Decay of the tripolar structure versus viscous time scale for different values of δ and Re. $\circ$: $\mathrm{Re}=500$, $\diamond$: $\mathrm{Re}=10^3$ and $+$: $\mathrm{Re}=10^4$.

by Rossi et al. [94].

To study the decay of the tripole on the shear-diffusion time scale, $|\omega_{\min}/\omega_{\max}|$ is plotted against $t/\mathrm{Re}^{-1/3}$ for different Reynolds numbers and perturbation amplitudes. Figure 7.30 presents the current results and those of Barba and Leonard for $|\omega_{\min}/\omega_{\max}|$ versus $t/\mathrm{Re}^{-1/3}$ for $\delta=0.1$ at various Reynolds numbers. It is observed that for this specific amplitude, $\delta=0.1$, the tripole decays on the shear-diffusion time scale, in agreement with the conclusion of [96]. As mentioned previously, in the current simulation the decay rate of the tripole is lower than that reported in [96]. This is manifested in Figure 7.30 by the retardation in the decay for $\mathrm{Re}=10^4$. Considering different perturbation amplitudes, the relaxation curves start to move apart when increasing δ and Re, Figure 7.31, again in agreement with the results of Barba and Leonard. However, at low Reynolds numbers the structure seems to decay on $t/\mathrm{Re}^{-1/3}$. Even when the perturbation amplitude is increased to $\delta=0.3$, which is considered a high distortion strength, the decay of the tripole for $\mathrm{Re}=500$ and $\mathrm{Re}=10^3$ still scales well on the shear-diffusion time scale, as seen in Figure 7.32. This is an interesting fea-

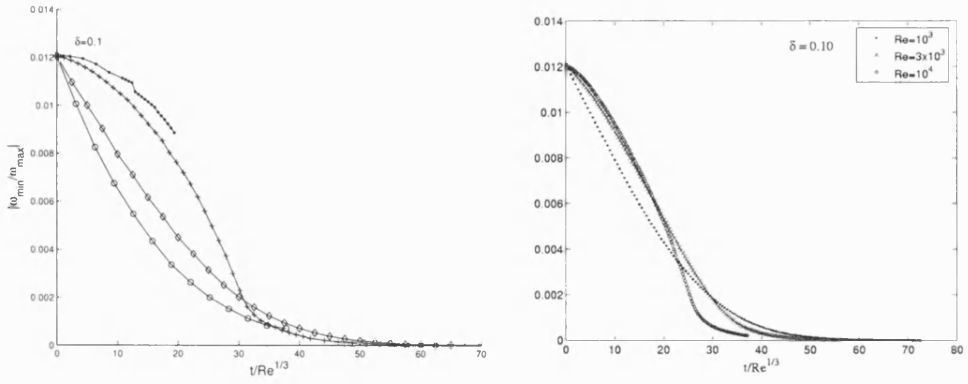

Figure 7.30: Decay of the tripolar structure on the shear-diffusion time scale. Left hand side: current results; ○: Re=500; ◇: Re=10^3; +: Re=10^4; •: Re=10^5. Right hand side: Barba and Leonard's results [96], reproduced with permission.

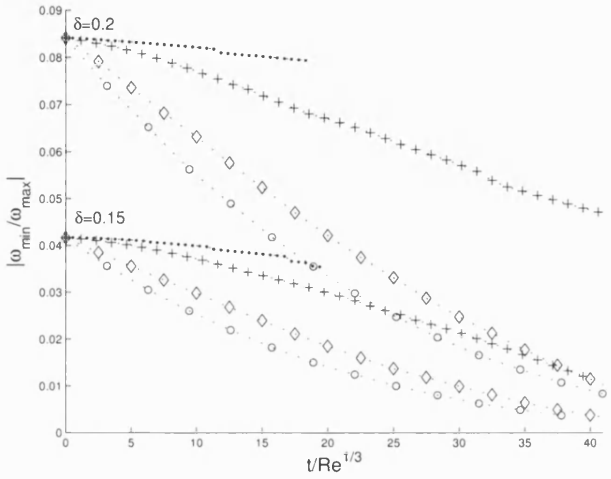

Figure 7.31: Decay of the tripole on the shear-diffusion time scale; ○: Re=500; ◇: Re=10^3; +: Re=10^4; •: Re=10^5.

ture which contradicts the finding of Barba and Leonard and their explanation about negligible nonlinear effects only at low δ. Instead this fact can be attributed to the strength of the satellites. At large Re the negative vorticity decays slowly. Thus when the inclusions are formed by the closure of the streamlines they are strong enough to counteract the shear-diffusion mechanism, so that the decay rate does not scale well on $t/\mathrm{Re}^{-1/3}$. At low Reynolds numbers, however, even for strong δ, the satellites are weak due to viscosity and cannot oppose shear-diffusion, so the mixing between them and the core happens more rapidly.

To better examine the different stages during the tripole decay, $|\omega_{\min}/\omega_{\max}|$ is plotted versus time t on logarithmic scales for various Reynolds numbers and perturbation

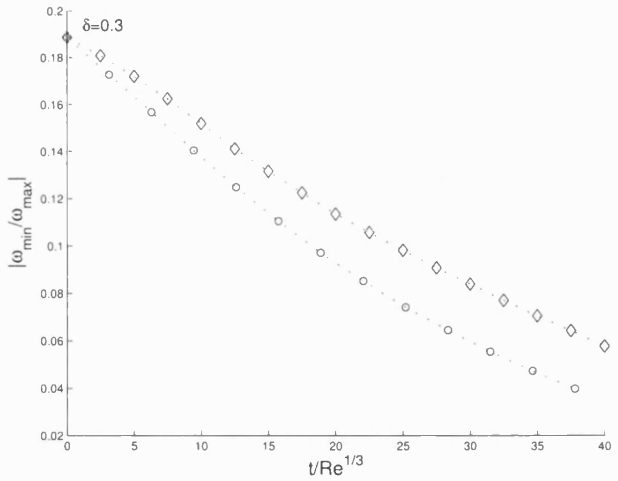

Figure 7.32: Decay of the tripole at low Reynolds numbers and δ=0.3 on the shear-diffusion time scale; ○: Re=500; ◇: Re=10^3.

amplitudes in Figure 7.33. It can be seen that the relaxation happens in two parts, first a slow reorganisation period followed by a fast decrease of the ratio. The time for the readjustment depends on the viscosity, as it increases with Re due to the slow viscous decay. On the other hand, for a given Reynolds number the rearrangement takes longer for larger δ due to the increase in amplitude of the side vortices. Examining Figure 7.33 one can conclude that for all Reynolds numbers and perturbation strengths the negative satellites will vanish as $t \to \infty$, leaving a Gaussian monopole as the asymptotic state of any tripole.

7.4.4 Unstable tripoles

Tripoles emerging from shielded monopoles have previously been observed to experience the growth of instabilities that break the structure into two dipoles traveling in opposite directions. In contrast, tripoles arising from unshielded vortices distorted by small perturbations were considered to be stable and their robustness was demonstrated by Barba and Leonard [96].

The case of large δ has not been addressed before in the literature, so a simulation was performed with δ=1, $|\omega_{\min}(0)/\omega_{\max}(0)|$=0.606, in order to assess the effect of such a large perturbation amplitude on the development of the base vortex. Initially, the magnitude of the negative satellites was strong enough to squeeze the centre vortex and cause its separation into two cores as seen in the first frame of Figure 7.34. At the start of the evolution, while the structure rotates counterclockwise, in the same direction as the base, the centre stretches and each part of it pairs with one satellite and moves away from the other half, in a behaviour similar to the formation of dipoles from unstable shielded monopoles or unstable tripoles as found numerically [69, 75] and experimentally [83, 84, 88, 91]. The side blobs rotate clockwise and draw vorticity

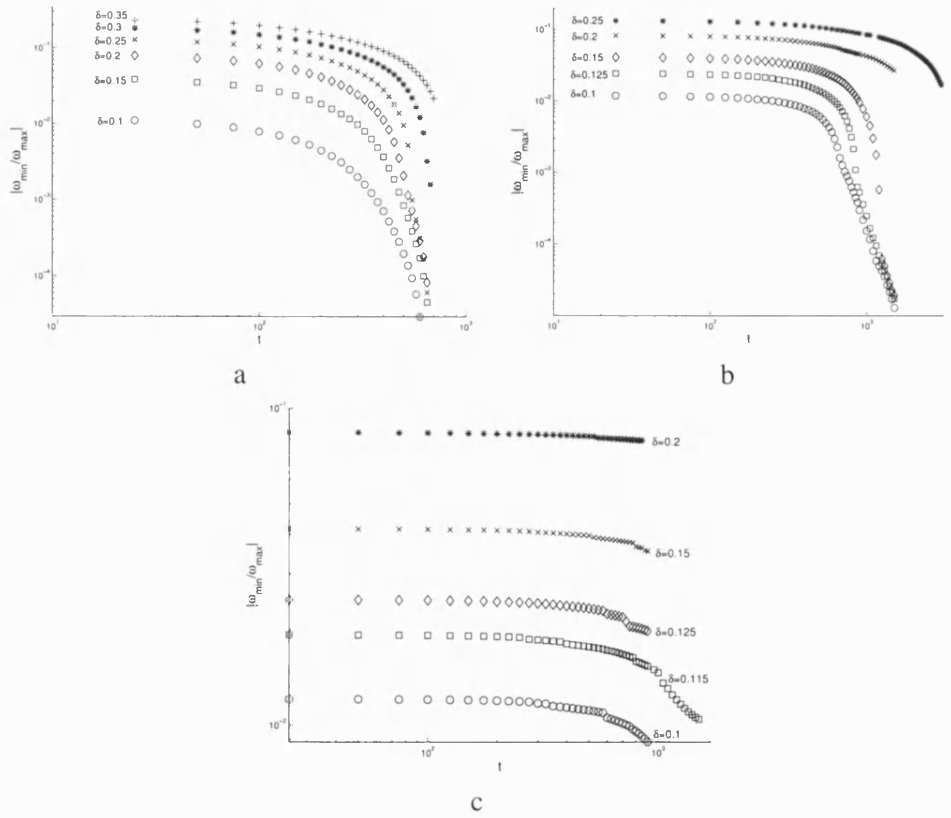

Figure 7.33: Decay stages of the tripolar structure for various Reynolds numbers and perturbation amplitudes on logarithmic scales. a: $\mathrm{Re}=10^3$; b: $\mathrm{Re}=10^4$; c: $\mathrm{Re}=10^5$

filaments from the tips of the base while the positive vortices rotate counterclockwise acquiring a circular shape. At $T\simeq 200$ two pairs of dipoles connected by a vortex strip can be clearly distinguished, and the structure loses its angular momentum as seen in the following frames. After their formation, the opposite sign vortices in each dipole encircle the remaining vorticity and the weak filaments diminish quickly due to viscous effects, so by $T=400$ the two dipoles are completely separate.

Another simulation was run for a longer time with the same perturbation amplitude, $\delta=1$, but for a higher Reynolds number, $\mathrm{Re}=10^5$. The early stage development of the unstable vortex in this case, up to $T=400$, is similar to the previous one with $\mathrm{Re}=10^4$, but the decay rate is slower due to the difference in viscosity. Owing to the presence of the circular outer boundary of the domain, where a streamfunction boundary condition was applied to represent a solid wall, once the dipoles emerge they can not keep moving radially outwards. Adding to this the fact that the dipolar structures are asymmetric as the positive vortices are stronger than the negative ones, $|\omega_{\min}(400)/\omega_{\max}(400)|=0.6053$, they make a looping excursion anticlockwise with the positive vortices moving faster than their negative counterparts. Then, the anticyclonic

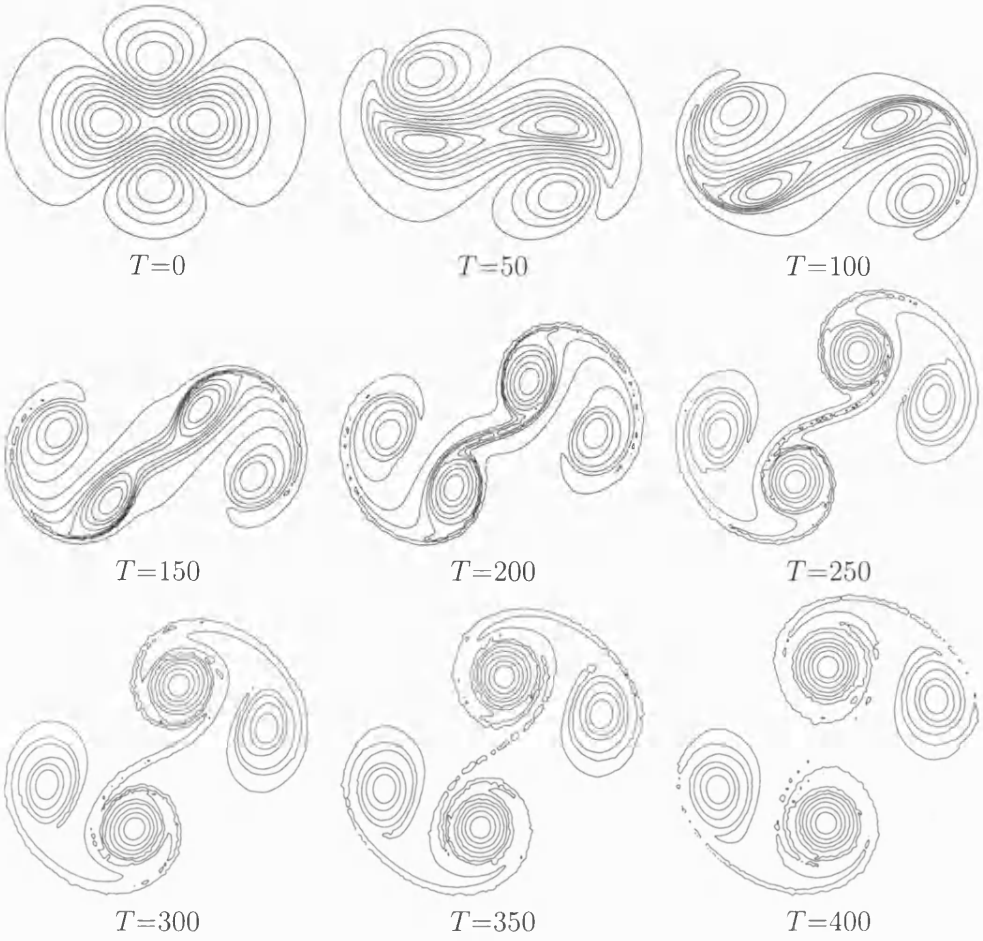

Figure 7.34: A strongly perturbed vortex separating into two pairs of dipoles: m=2, Re=10^4, δ=1.

patches move back to the centre of the domain where they collide and get squeezed between the two negative blobs.

Very similar behaviour was observed by Kloosterziel and van Heijst [84] while investigating experimentally the development of an anticyclonic barotropic vortex. They conducted their experiment in a circular water tank where they found that the unstable monopole grew a wavenumber-2 instability that led to the formation of two dipoles. The newly formed structures, which were also asymmetric, first moved radially until they hit the tank wall, then the two positive vortices looped back to the centre. Unfortunately, the authors did not show the later stages of the evolution process when the cyclonic vortices meet at the centre. However, in the current study, the simulation is carried on until T=2300, which allows observation of the results of this encounter.

The complete evolution process of the unstable tripole is displayed in Figure 7.35. After moving to the centre of the domain, the positive vortices approach each other,

collide and get squeezed by the two negative satellites. This triggers the merging of the central blobs into one core while the two negative patches align themselves on each side of it forming a tripolar structure that rotates anticlockwise as a solid body around the axis of the central vortex. As observed at T=1100, the collision of the positive blobs leads to an elongated, elliptically shaped vortex that while rotating develops vortex filaments from its tips, which are subsequently embedded by the cyclonic satellites. After a reorganisation period during which the vorticity wake dissipates due to viscous diffusion, the tripole becomes well defined with a strong core and two weaker satellites.

Tripolar formation from the collision of two dipoles was previously numerically discussed by Larichev and Reznik [72] and Orlandi and van Heijst [86]. The formation processes described in both papers were similar to the present results in terms of the collision and merging of the positive vortices, the formation of vortex filaments and the alignment of the negative patches to form two satellites around the core.

7.5 Emergence of high-order multipoles from perturbed unshielded Lamb-Oseen vortices

In this stage of the study, the Lamb-Oseen vortex is perturbed by 6-pole and 8-pole distortion. The aim of the investigation is to examine the effect of the perturbation amplitude on the evolution of the base vortex, so the Reynolds number is kept constant. The results of the various simulations are presented in the following subsections.

7.5.1 The triangular vortex

The triangular vortex, or the triangle, is a rare object of 2-D vortex flow that has been observed to emerge mainly from unstable shielded monopoles. The formation of triangles from perturbed unshielded Gaussian vortices had not been examined until a recent brief letter by Barba [104]. To investigate the possibility of a distorted unshielded monopole developing into a quasi-steady triangle, the evolution of a six-pole non-axisymmetric perturbation, m=3 in Equation 7.3, of different strengths superimposed on a Lamb-Oseen base vortex was simulated. The initial vorticity distribution of the flow is a positive triangular centre squeezed by three negative satellites, as shown for example in Figure 7.36.

The evolution of the perturbed monopole for a given Reynolds number depends on the distortion amplitude. The current simulations reveal that a distorted Lamb-Oseen vortex relaxes to either a monopolar attractor or a triangular vortex, suggesting that, similarly to the tripolar case, a threshold δ_{critical} separating both end states exists. A small amplitude generates weak satellites that mix with the base vortex, which then relaxes to axisymmetry, whereas a large δ produces strong negative enclosures that are conserved during the flow evolution leading to the emergence of a quasi-steady triangular structure. It is also found that the triangle once formed does not decay merely due

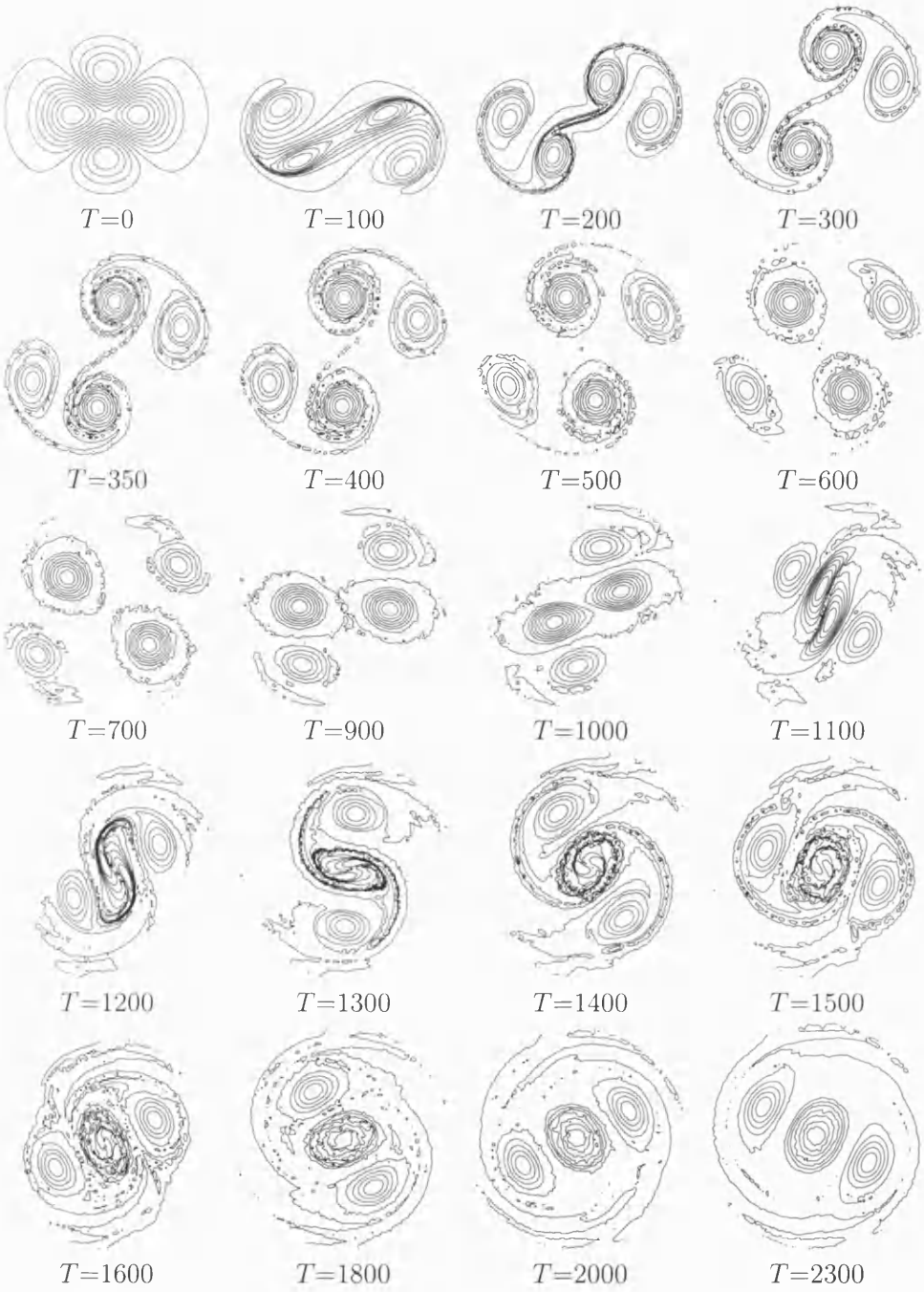

Figure 7.35: Contour plots of ω showing the development process of an unstable tripole Re=10^5, δ=1.

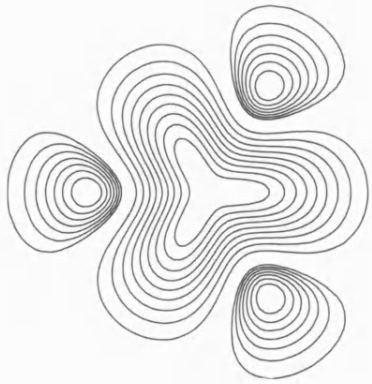

Figure 7.36: Gaussian monopole perturbed by a hexapolar distortion: m=3, δ=0.25.

to viscous diffusion while maintaining its shape, but evolves through satellite merger into a tripole, a process observed previously for triangles that emerge from shielded monopoles [84, 86, 100, 101] but reported here for the first time for triangular structures emerging from perturbed unshielded Lamb-Oseen vortices.

Contour plots of the vorticity ω during the evolution of a triangular vortex with initially weak perturbation amplitude, δ=0.25, at Re=10^4 are presented in Figure 7.37. During the flow development, the structure rotates anticlockwise as a solid body

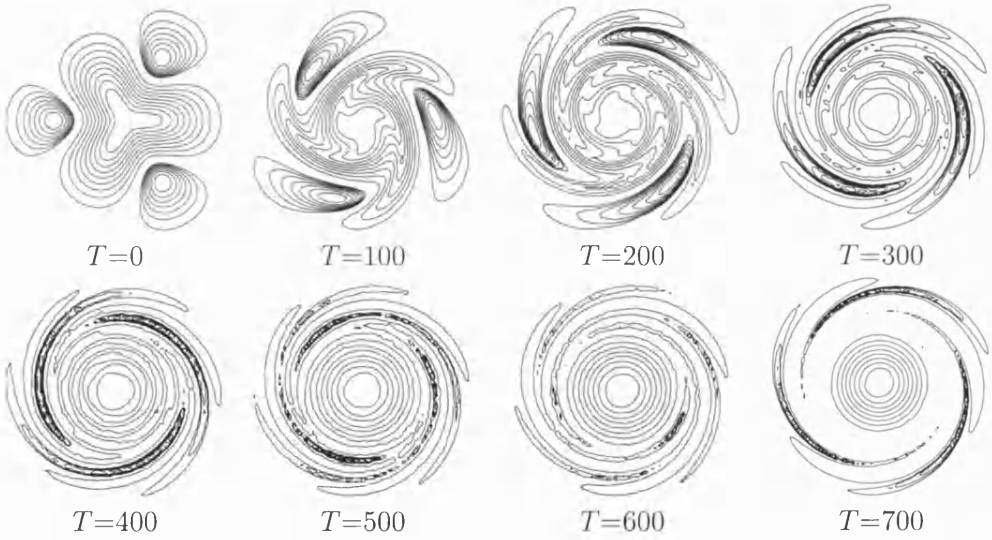

Figure 7.37: Evolution of a distorted unshielded Lamb-Oseen vortex by a weak hexapolar perturbation: δ=0.25, Re=10^4.

around the axis of the central vortex. The core readjusts itself into a circular form, developing filaments from its tips, which embed the stretching satellites. Then, the negative vorticity diminishes due to viscosity leaving the base vortex to relax back to

its original state. The change in the flow topology during the process is better visualized through the gray scale $\log|\omega|$, Figure 7.38. The images show clearly how the

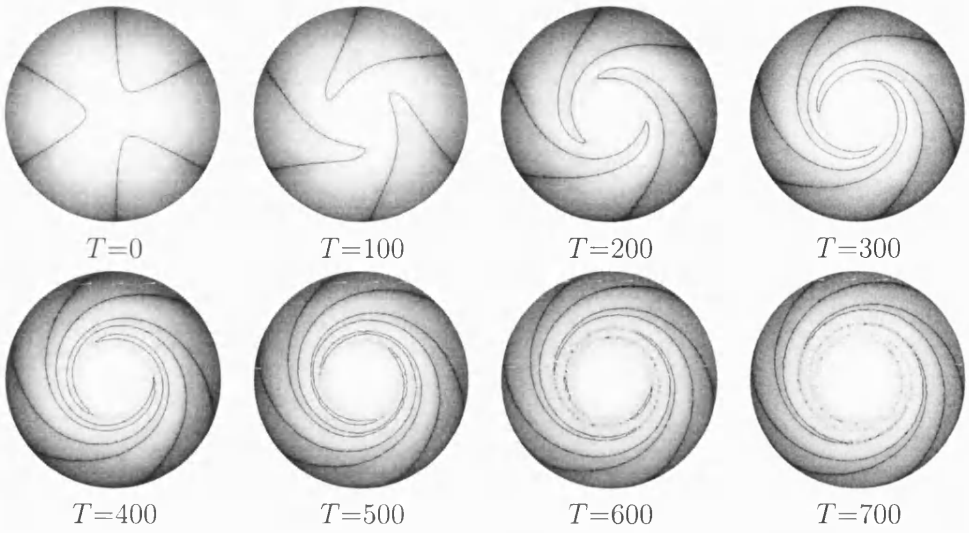

Figure 7.38: Gray scale plots of $\log|\omega|$ and the zero contour levels during the evolution of a distorted unshielded Lamb-Oseen vortex by a weak m=3 perturbation: δ=0.25, Re=10^4.

negative sides mix with the core as they wind up around it, and the zero contour lines fold flat onto themselves then decay while the flow relaxes towards axisymmetry.

Increasing the distortion amplitude affects the evolution process remarkably. In contrast to the situation outlined in Figure 7.38, when δ is increased the side vortices become stronger and the boundaries separating positive and negative vorticity regions lie closer to the core. Subsequently, as they wrap up around the base vortex, they do not mix with it but the zero contour lines enclose areas of negative vorticity, creating three isolated satellites around the centre, which characterises a triangle vortex, as shown in Figure 7.39 for δ=0.45 at Re=10^4. As a result of the shear exerted by the newly formed blobs, the core is squashed into a triangular form with one satellite on each side of it. The remaining weak negative filaments decay due to viscous effects. After the transient adjustment phase, the structure revolves around its central axis while keeping its shape for a short period, then one satellite is observed to lengthen and move closer towards another one.

In order to better visualize this mechanism, the flow development, is portrayed in terms of the contour levels of vorticity in Figure 7.40. It is interesting to note that in the first frame at T=0 the compression force of the three side vortices on the central vortex is strong enough to separate it into three inner cores that stay distinct in the early phase of the evolution before merging into one core at a later time. Contrary to the small perturbation case, Figure 7.37, here the base vortex is seen to develop weak filaments that decay and vanish quickly before having enough time to enclose the negative vorticity. Meanwhile, the satellites first stretch into thin strips, then rearrange

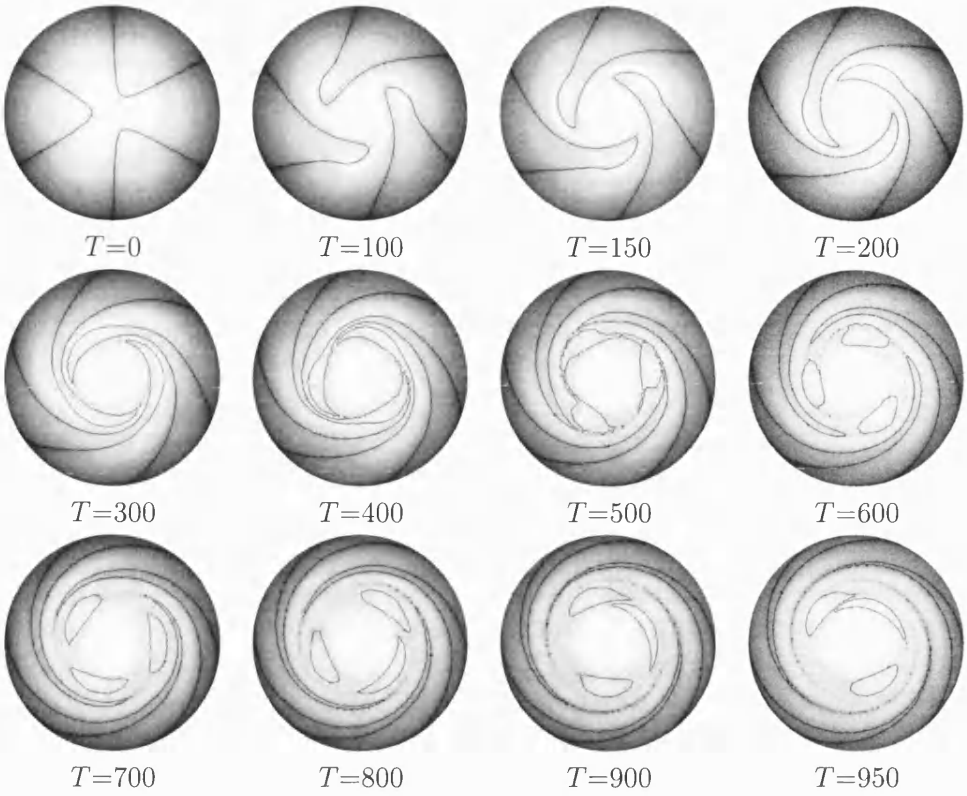

Figure 7.39: Gray scale plots of $\log|\omega|$ superposed with the zero contour levels of the vorticity during the evolution of the triangular vortex: δ=0.45, Re=10^4.

themselves into three elliptical patches around the centre, which coincides with the pinching of the zero contour lines noticed in Figure 7.39. The central vortex is then reshaped into a triangle due to the shear force of the satellites after having assumed a near-circular form in the early stages of the evolution. Later on as the side vortices decay, their shear effect on the centre diminishes, allowing the base vortex to reacquire an annular figure during its revolution. This mechanism affects one of the satellites by dragging it and wrapping it around the centre, thus moving it closer to another satellite, which explains the observation in the last frames of Figure 7.39.

Carnevale and Kloosterziel [99] and Beckers and van Heijst [100] studied the stability of the triangle and concluded that it is easier for the structure to break down into a tripole if its satellites have unequal strength. In order to check the validity of this conclusion in the current case, the magnitudes of the negative sides were studied directly after the emergence of the triangle at T=500. It was found that the top left satellite in frame T=500 of Figure 7.40 was weaker than those on the bottom left and right of the centre. The magnitude of the two strong sides is ω=-0.02 while for the third one it is ω=-0.018. Following the flow development after the emergence of the triangular structure, one can clearly see that the weak satellite is the vortex that stretches around

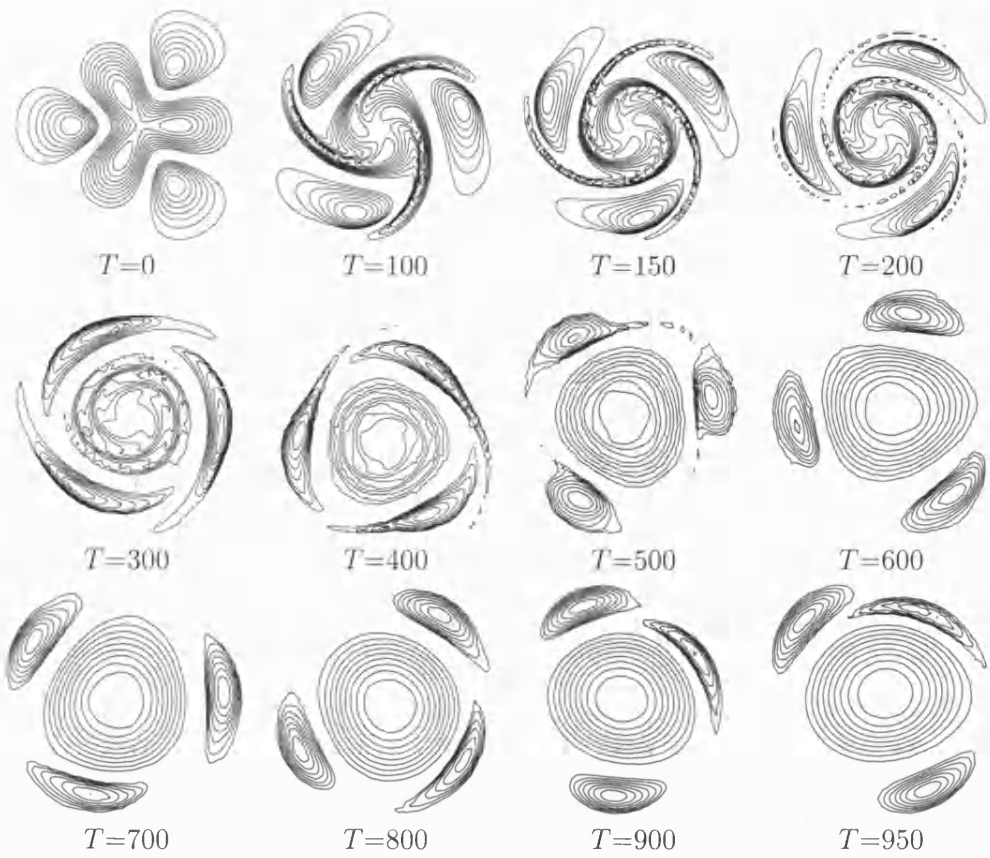

Figure 7.40: Contour levels of the vorticity ω showing the evolution of the triangular vortex: δ=0.45, Re=10^4.

the core, leading to the breakdown of the triangle. This result confirms the conclusion of [99, 100].

To observe what happens next after the two satellites approach each other, another simulation was run for a longer time with δ=0.65 at Re=10^4. The results are displayed in gray scale contour levels of the logarithm of vorticity in Figure 7.41. The early stage development of the flow is similar to the previous case, δ=0.45, where the highlighted zero level lines wind up around the base vortex and enfold three satellites around it. But as observed previously in the tripole study, increasing the amplitude of the perturbation accelerates the enclosure process. Moreover, in the current simulation the satellites are seen to rearrange themselves in small patches as they rotate clockwise around their axes and cyclonically around the core, and develop weak trailing filaments that decay in a short time. Increasing the perturbation amplitude affects the stability of the structure as it conserves its shape from its emergence at T =400 until T=1000 where one of the satellites becomes unstable. Studying the magnitude of the satellites, it is found that while the triangle is stable, the satellites are of equal, T=400

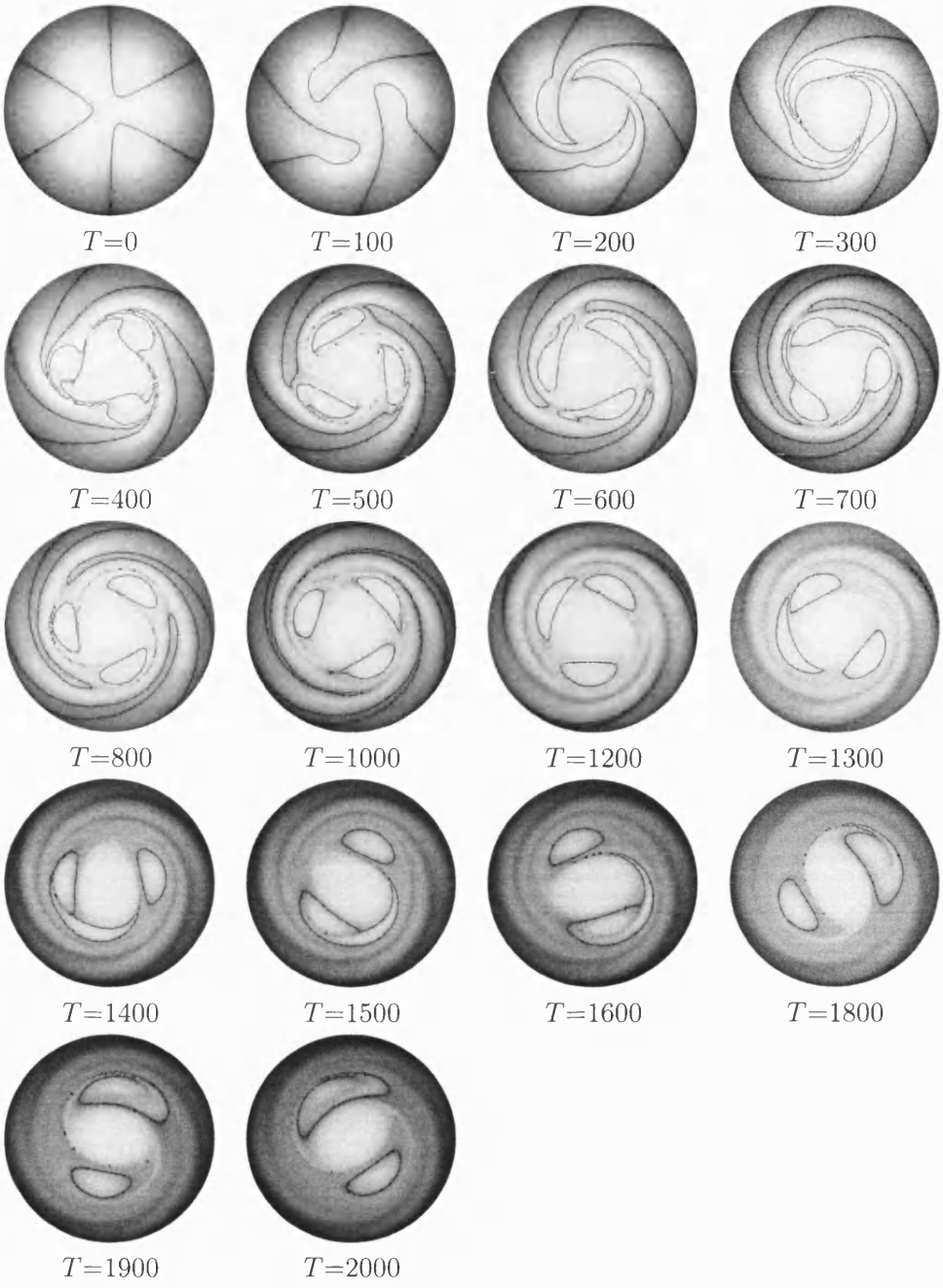

Figure 7.41: Gray scale plots of $\log|\omega|$ and the zero contour levels during the evolution of the triangular vortex: δ=0.65, Re=10^4.

and T=600, or nearly equal strength, T=800. However, at T=1000 the difference in magnitudes becomes significant, which might have helped trigger the instability ob-

served in this time frame as discussed earlier. In the later stage of the evolution, the core vortex loses its triangular form and becomes egg-shaped, forcing one of its satellites to stretch and approach another one. Then the two vortices collide and merge forming one inclusion, thus transforming the triangle into a tripole, as observed in the last six frames of Figure 7.41. The newly emerged structure is asymmetric as the resultant satellite is bigger than its associate, and is expected to relax into axisymmetry due to viscous effects as discussed in §7.4.

The late stages of the flow development are shown in Figure 7.42 in terms of the contour plots of the vorticity ω. It is clearly discerned that the axisymmetrisation of the structure starts from the inner centre of the base vortex, as for example at T=800 where it is already circular though the circumferential shape of the core is still a triangle. As the sides decay, the centre elongates into an ellipse and one satellite stretches into a filament before colliding and merging with another satellite. Then the resulting vortex is seen to rearrange itself into an elliptical patch by developing a weak trailing filament similar to the reorganisation phase of the three satellites noted earlier on.

An initial quadrupolar perturbation, m=2, of $O(1)$ broke the base vortex into two dipoles as discussed in §7.4.4. To investigate the effect of a hexapolar perturbation, m=3, of the same order on a monopole, a disturbance ω' of amplitude δ=1 is added to a relaxing Lamb-Oseen vortex at Re=10^4. The complete evolution process of this situation is presented in Figure 7.43. Initially, as the structure rotates cyclonically, the shear force of the perturbation amplitude divides the core into three parts, each pulled clockwise by one satellite as depicted at T=50. However, the magnitudes of the negative sides are not strong enough to completely detach the base positive vorticity, which is observed to quickly readjust into a triangular blob at T=75. The remaining vorticity filaments already drawn by the satellites decay and disconnect from the centre, and the structure evolves into a triangular vortex as seen at T=200. This observation emphasizes the fact that the relaxation of a monopole perturbed by hexapolar distortion into a triangle accelerates as δ increases. It is interesting to note at this time that even though the vorticity has regrouped into one centre, the initial three cores have not mixed together yet, as they can be clearly distinguished in the central vortex. Then, the negative patches squeeze the newly formed triangle forcing the three different cores to approach each other and merge in one triangular centre, which originally has an opposite orientation to the main vortex as seen at T=500. Once the side vortices compress the base they extract some vorticity from it: as a result filaments develop from its tip and wrap around the satellites. After this transient period the quasi-steady triangle is robust and lives for many turn-over times decaying slowly before two satellites collide and merge, turning the structure into a tripole that will relax towards axisymmetry.

The results of the current simulations conclude that increasing δ affects the stability of the triangle and significantly extends its lifespan. This is due to the fact that a stronger initial perturbation leads to larger magnitude negative inclusions, and so their shear effects on the core, which force the base into a triangular shape, last longer. Once these effects diminish, the centre assumes an elliptical form and the structure relaxes towards a tripole. Since the triangle has proven to be stable and to live for many turnover times, it can be considered a member of the coherent structure family beside

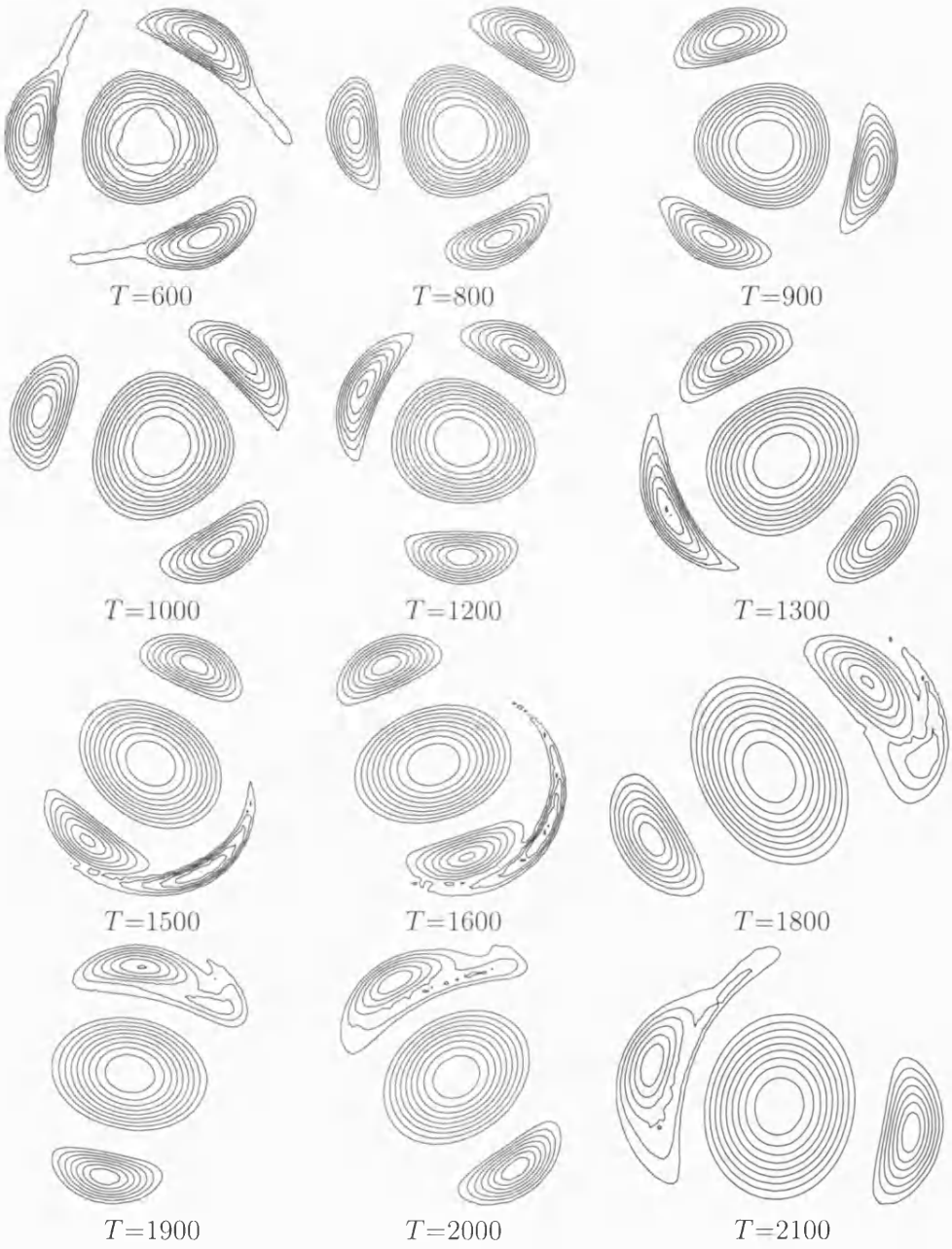

Figure 7.42: Contour plots of vorticity showing the late stages of the triangular vortex evolution: δ=0.65, Re=10^4.

the monopole, dipole and tripole. However, it is the weakest member of this family as it has been shown that for all perturbation amplitudes it will break down into a tripole during its decay towards axisymmetry. Changing the Reynolds number is believed to

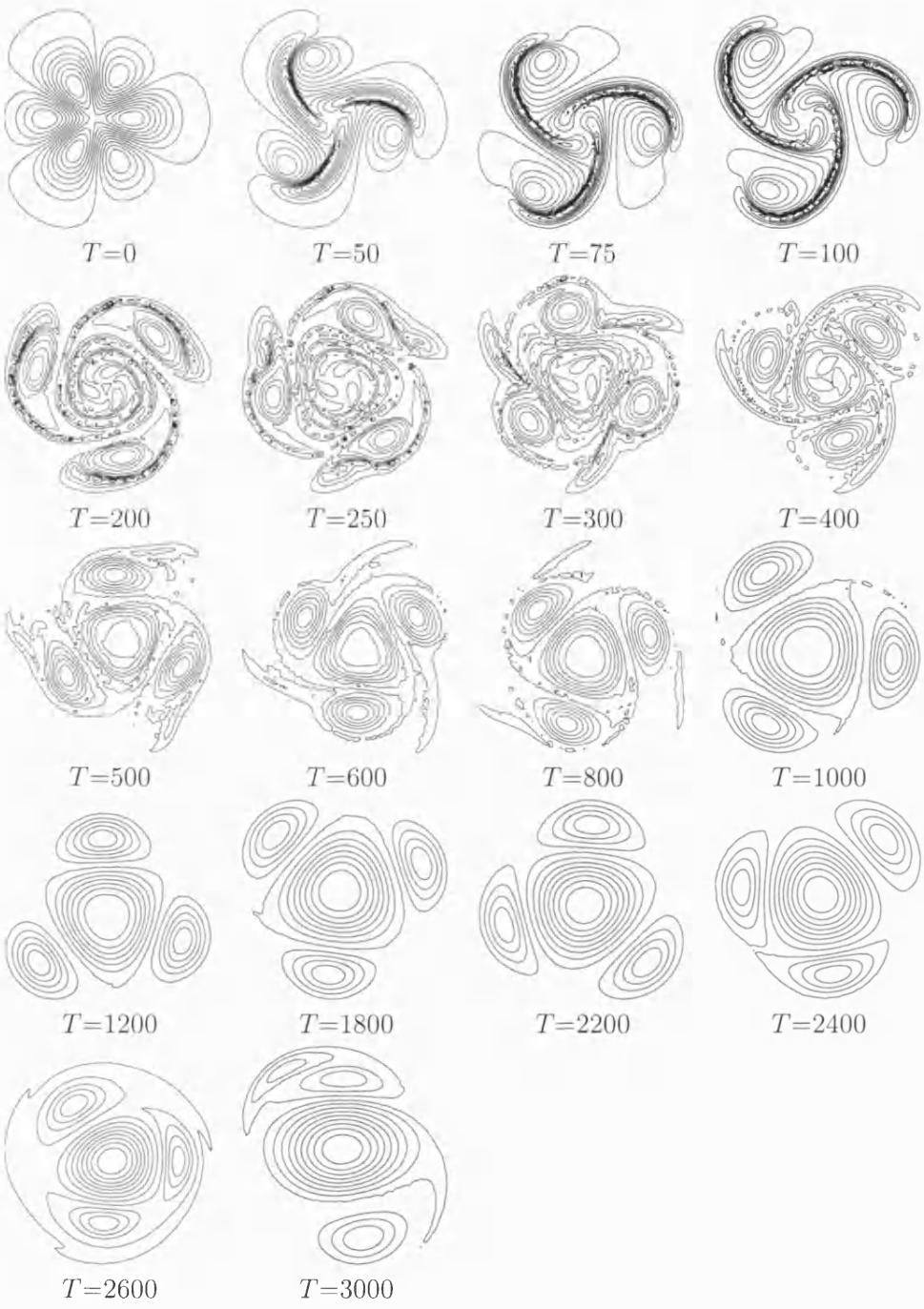

Figure 7.43: Contour plots of vorticity showing the evolution of a Lamb-Oseen vortex superposed by an $O(1)$ six-pole perturbation: δ=1, Re=10^4.

have the same effect on the formation of the triangle as on the formation of the tripole studied in §7.4.2. Decreasing Re will increase the viscosity, thus a higher δ will be required for the perturbed monopole to evolve into a triangular structure.

7.5.2 An unstable triangle

Triangular vortices emerging from the growth and saturation of instabilities in strongly unstable shielded monopoles have been observed, in some cases, after the merging of the satellites to break up into two dipoles [99, 101]. However, in the current study the Lamb-Oseen vortex became unstable and developed three dipoles when perturbed by a very strong distortion, δ=3. This process is shown in Figure 7.44 for Re=10^4. Initially, the ratio of minimum to maximum vorticity is $|\omega_{\min}(0)/\omega_{\max}(0)|$=0.8461, so the negative sides are still weaker than the base vortex. However, their shear stress divides the centre into three parts that are attracted and pulled clockwise by the satellites while the whole structure rotates anticlockwise. In contrast to the unstable tripole, Figure 7.34, in the current case the negative blobs are not able to completely break the centre into three separate vortices as some vorticity is seen to reassemble in the middle and form an axisymmetric monopole. Meanwhile, the detached positive vorticity overcomes the encircling force of the negative sides, since its amplitude is still stronger than theirs $|\omega_{\max}(75)/\omega_{\min}(75)|$=1.1819, and rearranges itself into three cyclonic vortices. This creates three dipoles that disengage from the core vortex and travel in different radial directions. An interesting feature stands out in the last frames of Figure 7.44, where it is clearly recognized that the newly formed dipoles have ceased to rotate, unlike the central monopole. This is a physical result since dipoles have zero angular momentum.

The results obtained in this simulation are similar to previous experimental and numerical observations [97, 98], where a triangular-like structure created in two-layer rotating fluid became unstable and broke into a main central vortex and three dipoles travelling away from each other. However, it is the first time such a process has been reported for a triangle emerging from an unshielded perturbed Lamb-Oseen vortex.

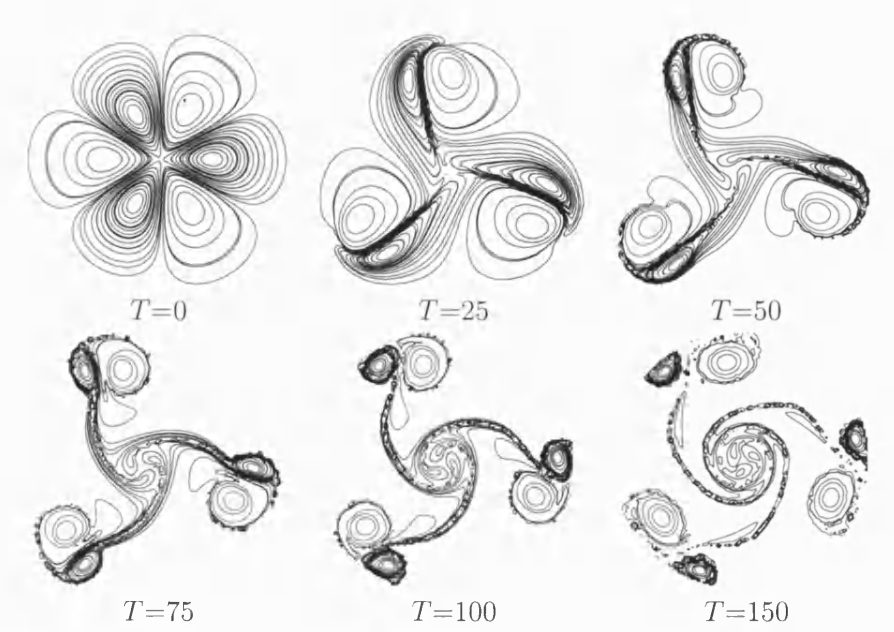

Figure 7.44: Contour plots of vorticity during the evolution of an unstable triangular vortex: δ=3, Re=10^4.

7.5.3 The square vortex

The emergence of the quasi-steady triangular structure from a perturbed unshielded monopole, as reported in §7.5.1, motivated the investigation of the effect of an 8-pole distortion, m=4, superimposed on a Lamb-Oseen vortex. The initial vorticity field is a positive centre compressed by four negative blobs, as shown in Figure 7.45.

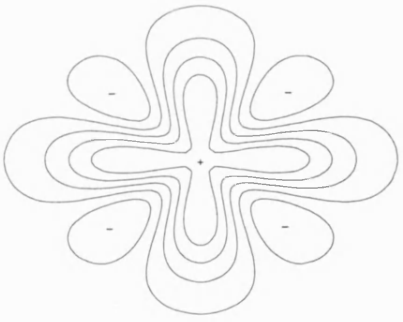

Figure 7.45: Initial vorticity field for a Lamb-Oseen vortex perturbed by an 8-pole distortion: m=4, δ=0.5, Re=10^4.

Barba [104] mentioned very briefly that m=4 perturbations with amplitudes higher than δ=0.6 generate unstable square vortices that reorganise into tripoles through vortex merging. Moreover, shielded monopoles subjected to mode-4 instabilities were

observed to form unstable square structures that broke down to tripoles after a short time through satellite merging [99, 101]. In the current study, simulations were run for different δ at a constant Reynolds number, $\mathrm{Re}=10^4$, in order to explore the effect of the amplitude on the development and behaviour of the perturbed monopole.

Since the evolution of a Lamb-Oseen vortex distorted by an octopolar perturbation with $\delta<0.6$ has not been reported in the literature so far, simulations were run for $\delta=0.2$ and 0.5. In the first case, which is presented in Figure 7.46 in terms of the gray scale plots of $\log|\omega|$, the four weak negative sides are observed to evolve around the centre and stretch into thin filaments that degenerate quickly due to viscous effects, leaving an axisymmetric vortex. Thus, as observed in the quadrupolar and hexapolar perturbation studies, for small 8-pole distortion amplitudes the monopole is the attractor for the relaxing perturbed Lamb-Oseen vortex.

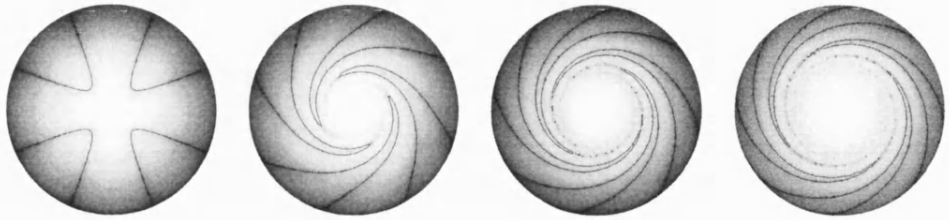

Figure 7.46: Gray scale plots of $\log|\omega|$ and the zero level contour lines showing the relaxation of a perturbed Lamb-Oseen vortex towards axisymmetry: $m=4$, $\delta=0.2$, $\mathrm{Re}=10^4$.

However, for $\delta=0.5$, a different evolution mechanism is observed. Since the magnitude of the negative vorticity is stronger than in the previous case but the viscosity is kept constant, the side vortices decay more slowly and last longer as they wrap up around the core. As a result, the four zero level contour lines that separate the opposite sign vorticity regions meet each other and encircle the positive centre with a negative ring, which splits later on into two different cells. After the formation of these enclosures, an asymmetric tripolar structure is seen to arise through the rearrangement of the negative patches into elliptical blobs around the base and the decay of the remaining vorticity filaments. The flow development is displayed through the gray scale plots of $\log|\omega|$ in Figure 7.47. The emergence of the tripolar vortex from the perturbed Gaussian monopole is also presented in terms of the contour plots of ω in Figure 7.48. As seen at $T=550$, the negative vorticity is already regrouped in two stretching filaments on each side of the centre, which during the flow development process readjust in elliptical patches that characterise the tripole. Once formed, the structure rotates as a solid body around its main axis. This result shows that the tripole is also an attractor for a relaxing Lamb-Oseen vortex distorted by an 8-pole perturbation, and there should exist a threshold amplitude δ that separates the axisymmetric and the tripolar states.

When the perturbation amplitude is increased to $\delta=0.75$, an unstable square vortex emerges and breaks shortly after its formation into a tripole, in agreement with Barba's

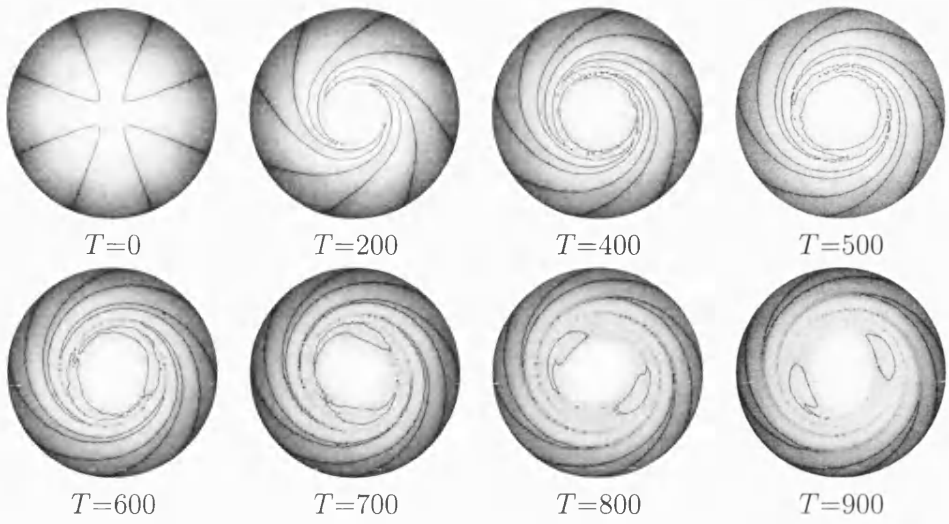

Figure 7.47: Emergence of a tripole from a perturbed Lamb-Oseen vortex: m=4, δ=0.5, Re=10^4.

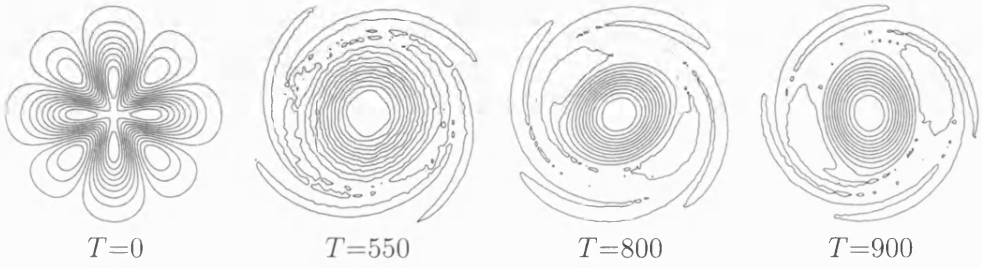

Figure 7.48: Contour plots of vorticity showing the emergence of a tripole from a perturbed Lamb-Oseen vortex: m=4, δ=0.5, Re=10^4.

finding [104]. The flow development process is shown through the sequence of the gray scale plots in Figure 7.49. During the rotation of the structure as a solid body, the negative patches stretch around the base and rearrange themselves in four satellites when the zero level contour lines pinch, compressing the core into a square shape as observed at T=400. The magnitudes of the satellites are studied directly after the emergence of the structure where it is found that the two vortices on the left and right of the core are of equal strength and 8.3% stronger than the other two situated on top of and below the centre, which are also of equal strength. Thus, it is expected that the square will become unstable, in accordance with previous results [99, 100]. This is observed to occur at T=500 where each strong satellite pulls a weaker one, then collides and merges with it. Meanwhile the centre evolves into an ellipse, and the structure transforms into a tripole. The newly formed sides undergo an adjustment phase as the vortex relaxes towards axisymmetry. The satellite merging process and the emergence of the tripole are also presented through the contour plots of vorticity

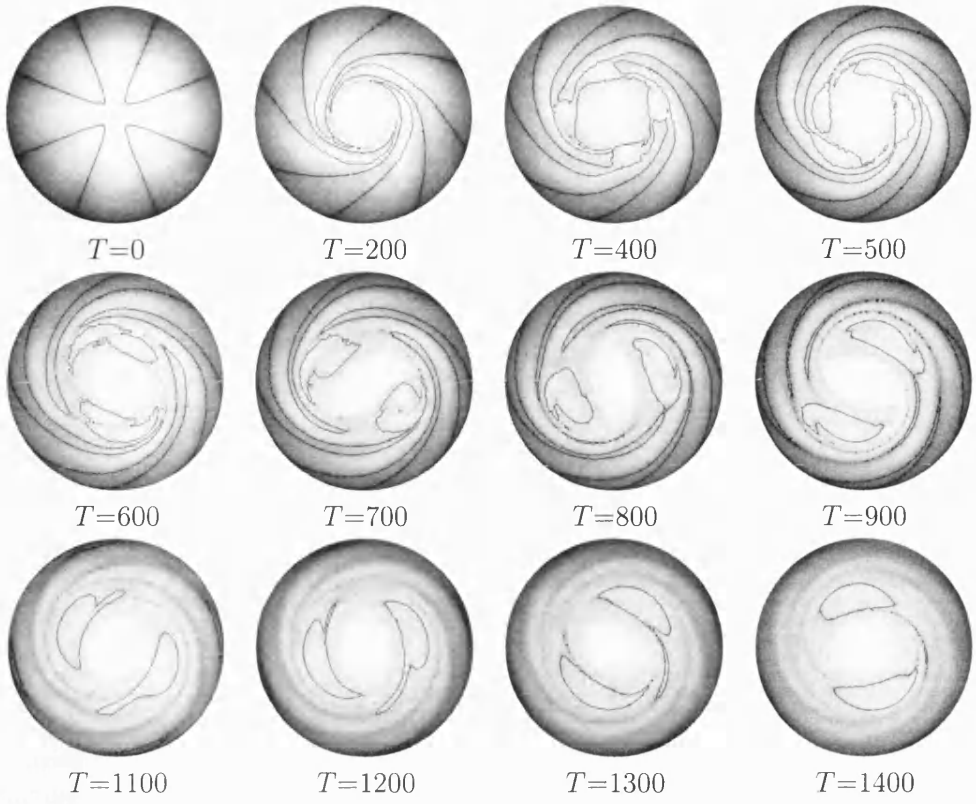

Figure 7.49: The evolution of a Gaussian monopole perturbed by an m=4 distortion amplitude with δ=0.75 at Re=10^4 into an unstable square vortex that transforms into a tripole.

in Figure 7.50.

In another simulation with δ=1 and Re=10^4, the perturbed Lamb-Oseen vortex relaxes more quickly into a square, as can be ascertained from comparing Figure 7.50 and Figure 7.51. The latter figure shows the development of the perturbed monopole in the current case. In the former situation, δ=0.75, the square vortex appears at around T=400, while in the current one it is visible at T=300. Initially, the negative patches pull positive vorticity from the centre, generating four filaments that entrap the sides between them and the core, as seen at T=200. But as the filaments decay, the negative vorticity reorganises itself in four satellites, one at each side of the base, which consequently takes a square form as seen in the fourth frame of Figure 7.51. This arrangement defines the new structure. Even though the satellites in this case are strong, $|\omega_{\min}(300)/\omega_{\max}(300)|$=0.6708, their shear forces are not capable of holding the core in a square shape for long, thus it evolves into an ellipse. This fact might be attributed to the difference in the satellite strengths.

Once formed, the negative vortices do not have equal magnitudes, as it is found that those on the bottom left and top right corners are respectively stronger than the other

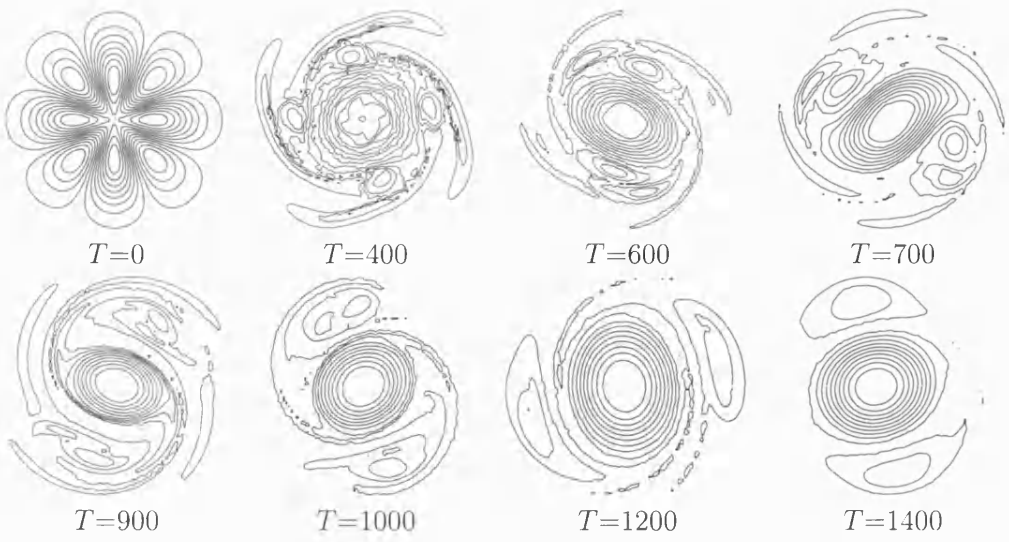

Figure 7.50: Contour plots of ω showing the transformation of an unstable square vortex into a tripole: m=4, δ=0.75, Re=10^4.

two blobs below and on top of the core. This is of importance in the flow development, since the merging of the satellites does not happen randomly but, as observed in the following frames, the weak sides are pulled by the strong ones, and each strong-weak pair merges into one vortex. This process affects the core, because as the weak vortices move towards the strong ones, they free two edges of the central vortex from their shear effects. Thus as the structure revolves, the unrestricted sides lose their right angles and curve, changing the geometry of the centre. This process leads to the transformation of the square into a tripole. From the current results, it can be concluded that the asymmetric strength of the satellites affects the stability of the square structure.

In order to investigate the effect of increasing the perturbation amplitude on the stability of the emerged square structure, a simulation is run for δ=1.5 while the Reynolds number is kept constant, Re=10^4. The behaviour of the perturbed monopole is presented in Figure 7.52. The current simulation provides more evidence that increasing δ accelerates the formation of the square vortex, as it emerges here at T=200. Initially, the negative blobs pull some vorticity from the core towards them, and since they are strong, the magnitudes of the positive filaments drawn are large. Thus they do not decay quickly as observed in the previous simulations, but reorganise into patches, creating four dipolar-like vortices surrounding the square centre as seen at T=300. However, the negative blobs do not pair with the newly formed vortices and move away from the centre as one might expect, but keep rotating with the base while the secondary positive vortices revolve in their fixed positions as four independent monopoles. Due to the splitting of the positive vorticity, the core is weakened and its magnitude becomes equal to that of its satellites, $|\omega_{\min}(300)/\omega_{\max}(300)|$=0.9966, which increases the effect of the shear forces and leads to the suppression of the centre between its four

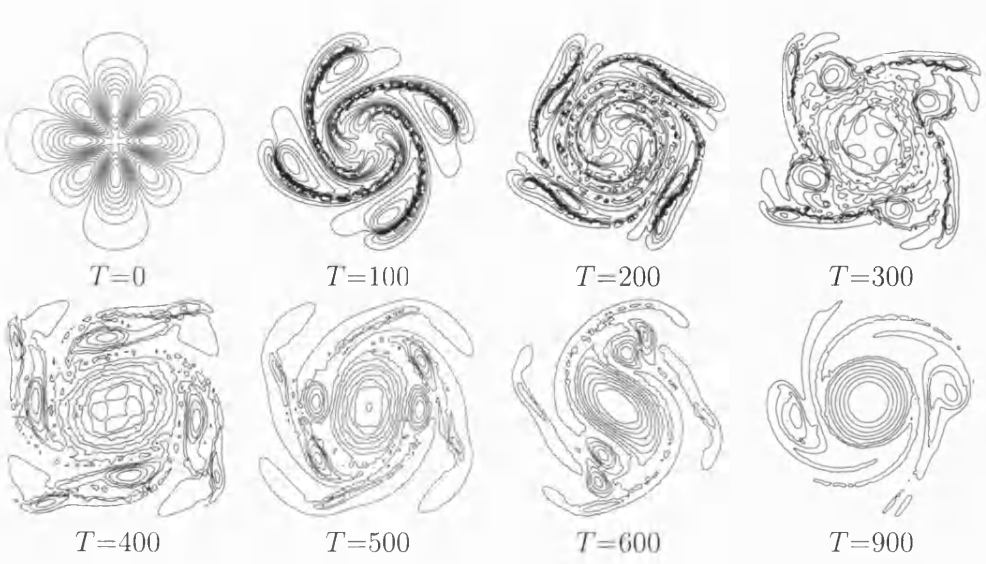

Figure 7.51: Contour plots of ω showing the evolution of a Gaussian monopole perturbed by an m=4 distortion with δ=1 at Re=10^4 into an unstable square vortex then a tripole.

sides. Then the negative blobs approach one another, triggering the transformation of the core into an ellipse and the square vortex into a tripole. During the process, the strong sides squeeze the centre into an elongated ellipse, and draw vorticity filaments from it that wrap around the two new satellites. Meanwhile, the secondary positive vortices hold their positions until they are attracted either by the core or its filaments, and merge with them, as clearly seen in the last four frames of Figure 7.52. In the next stage of the development, the filaments are expected to decay and the structure to relax into a tripole and then a monopole.

So, in contrast to the triangle studied in §7.5.1, increasing the initial strength of the satellites by increasing δ does not affect the stability of the square vortex. This structure is very unstable, and, as shown through this set of simulations, will relax into a tripole shortly after its formation. As a result, it can not be accepted as a member of the family of coherent structures.

7.5.4 The break up of the square vortex

Square vortices emerging from shielded monopoles studied by Carnevale and Kloosterziel [99] and from three-contour Rankine vortices investigated by Morel and Carton [101] were found after their evolution into tripoles to break up into two dipoles that move away from each other. This mechanism has not been investigated for unshielded Gaussian monopoles perturbed by an m=4 distortion. In a previous study, §7.4.4, it was concluded that a tripolar structure breaks up when its negative blobs are strong enough to tear the core into two vortices. So in order to increase the magnitude of the satellites in the tripole that emerges from the unstable square, the initial pertur-

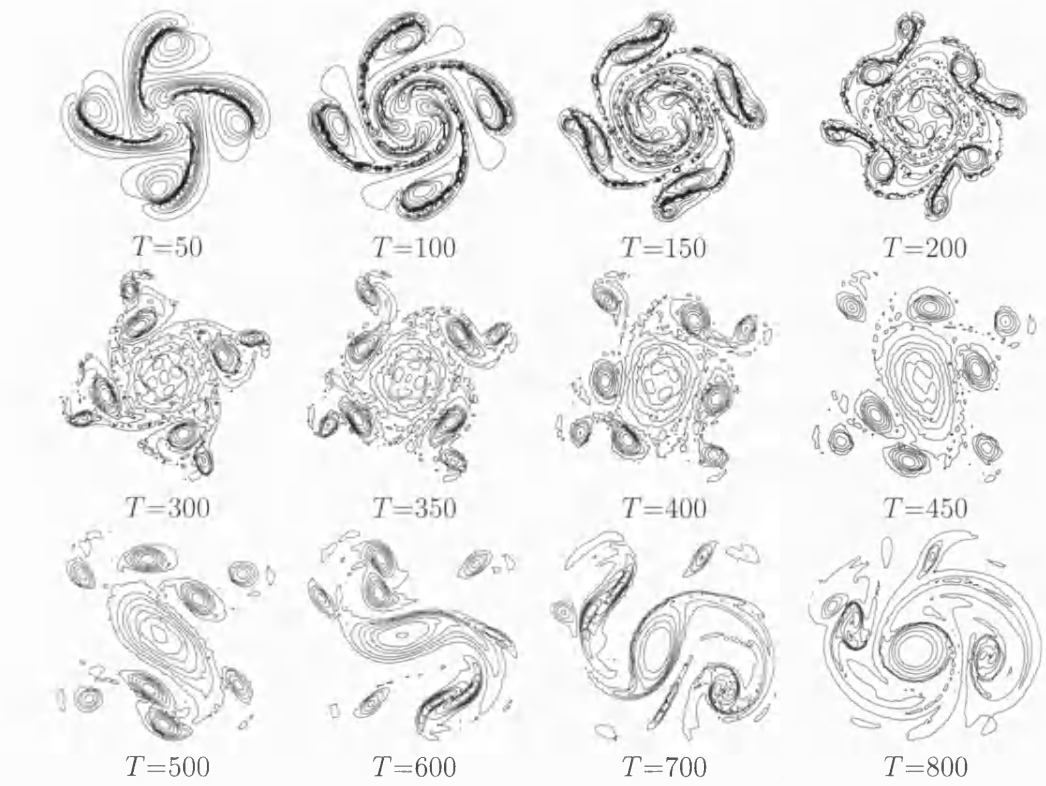

Figure 7.52: Contour plots of the vorticity during the evolution of a Gaussian monopole distorted initially by a strong m=4 perturbation: δ=1.5, Re=10^4.

bation amplitude was increased to δ=2. The results of this study are presented in terms of contour plots of ω in Figure 7.53. The early stage development of the flow is similar to the previous simulation, δ=1.5, shown in Figure 7.52. The negative sides draw filaments of positive vorticity from the centre, which readjust themselves into four positive monopoles. Then the core takes an elliptical shape and the pairs of satellites at each side of it approach, collide and merge into one vortex. The newly formed negative blobs are stronger than the main vortex, $|\omega_{\min}(600)/\omega_{\max}(600)|$=1.2671, so they compress it and tear it into two halves as observed between T=600 and T=700, forming two dipoles that travel in opposite directions. During this process, the secondary positive vortices are either drawn by the core, and merge with it, or by its sides so they wrap around them and decay. The current simulation is carried out on a circular mesh with a streamfunction boundary condition in order to represent a solid wall. Thus, after the break up of the tripole, the radial movement of the dipoles is restricted by the outer boundary of the domain. So instead of continuing to move away from each other, the dipoles loop back anticlockwise to the centre where the positive vortices meet again, a similar behaviour to that studied in §7.4.4. As a result, the late stage development of this flow is expected to be similar to the situation shown in Figure 7.35, where the positive vortices merge and form one centre between the two negative patches, emerging

as a new tripolar structure.

In order to observe the difference in evolution of the unstable square vortex depending on the initial perturbation strength, $|\omega_{\min}/\omega_{\max}|$ was plotted for three different cases, δ=1, 1.5, 2, in Figure 7.54. In all three situations, the ratio increases in the early part of the simulation, which might be due to the weakening of the core by the drawing in of positive vorticity by the sides, as seen in the second frames of Figures 7.51—7.53. Then for the two weaker perturbations, δ=1 and δ=1.5, the ratio decays or levels off then decays, which coincides with the rearrangement of the core and the transformation of the structure into a tripole. However, for the larger amplitude, δ=2, the negative sides become much stronger than the core, so when they merge the magnitude of the newly formed satellites is nearly 27% larger than that of the core, which triggers the breaking of the structure into two dipoles. It is interesting to note that between t=550 and t=675, which is the period where the core is stretched and torn in two, the ratio decreases very slowly, then accelerates once the dipoles emerge.

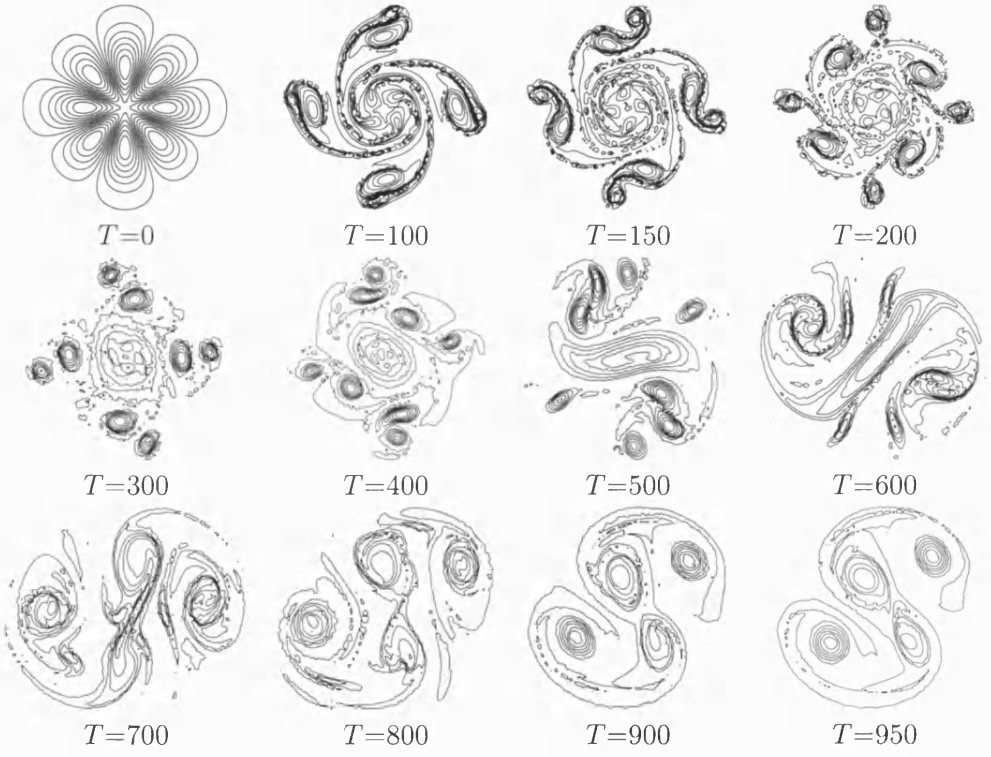

Figure 7.53: Contour plots of ω showing the break up of a Gaussian monopole perturbed by an m=4 distortion amplitude with δ=2 at Re=10^4 into a pair of dipoles.

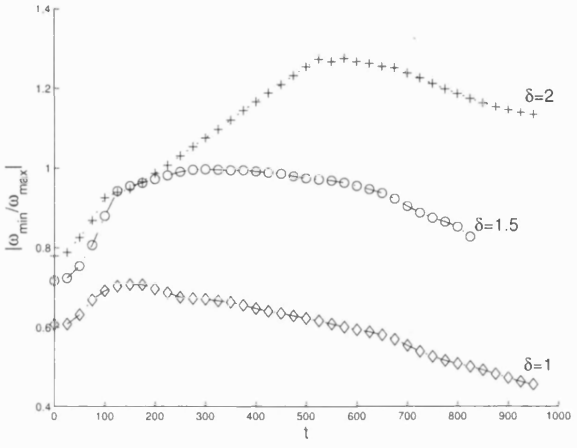

Figure 7.54: The change of the ratio of minimum to maximum vorticity, $|\omega_{\min}/\omega_{\max}|$, in an unstable square vortex with time, t, for three different perturbation strengths; Re=10^4, $\diamond$:δ=1, $\circ$:δ=1.5 and $+$: δ=2.

Chapter 8

Conclusions

> *and though with great difficulty I have got hither, yet now I do not repent me of all the trouble I have been at to arrive where I am. My sword I give to him that shall succeed me in my pilgrimage, and my courage and skill to him that can get it. My marks and scars I carry with me, to be a witness for me that I have fought His battles who will now be my rewarder.*
>
> *The Pilgrim's Progress*, John Bunyan, 1684

Lagrangian vortex methods are powerful tools for the study of unsteady incompressible fluids. They discretise the flow field into regions of vorticity that are tracked in a Lagrangian reference frame. They are simple and easy to implement, but have serious limitations in terms of computational time and modelling of viscous diffusion. Several schemes have been introduced in order to overcome these limitations, and the field is still maturing.

In this thesis, a novel technique for the computation of velocities in two-dimensional Lagrangian vortex methods has been introduced, validated and assessed. The method enjoys several advantages over classical Lagrangian vortex methods, especially its ability to reduce computational time and compute viscous effects. The approach is based on the direct solution of the partial differential equation for streamfunction on computational points. The vorticity field is represented by highly irregular meshes, where the nodes are connected by a Delaunay triangulation. At the beginning of this project, a ready code based on the GNU Triangulated Surface Library was used to code the triangulation. Later on, the initial mesh generator was modified by the author in order to introduce solid bodies in the computational domain. After generating an unstructured mesh without a body in it, the vertices are freed from their triangulation in order to allow addition of new nodes to the grid. Then the points forming the circumference of the body are added to the domain and all the nodes lying inside a close geometry are deleted because they are not part of the computational domain anymore. As for the addition of new points, deletion of nodes from the grid is possible only when the vertices are not connected. Once all the nodes inside the body are removed, the remaining points are re-triangulated and the mesh is updated. This algorithm was

tested and proven to be robust to be used in future studies to produces meshes around any desired geometry.

After generating the mesh, the streamfunction and its derivatives are approximated by a second order Taylor series at each node, and a least-squares error is defined. To achieve this approximation, a certain number of neighbours must be chosen for the node. The selection of neighbours is done through an original approach that guarantees a good point distribution around the vertex, while being simple and time efficient. The idea is to build a web of points around the main nodes, first by identifying the vertices directly connected to it by an edge, then by adding the points connected to these nodes. Every time a new node is added to the list of potential neighbours, the vertices connected to it by an edge are identified and added to the web. In order to minimize the computational time, a cut off distance is set around the main node, after which no more points are added. This distance is chosen based on the mesh quality. When simulating flows around solid boundaries, an extra check is performed before adding new nodes to the list of neighbours, since physically two particles in the flow field separated by solid body will not affect each other. In this case, before adding the new point, a line is drawn between it and the main node. If this line intersects the solid geometry, then the two nodes are separated by the body, thus they cannot be neighbours. Otherwise, the point is added to the list. Once the web is built, the points are sorted by distance from the main vertex and the n closest are chosen as neighbours for the Taylor series expansion. This technique was adopted because it uses any point in the flow flied, as long as it is close enough to the main node, even if it is not link to it by an edge. To get a smooth approximation of the streamfunction and its derivatives, this technique is better than using points directly connected to a node but geometrically far away from it.

Once all the neighbours are chosen and the equations are assembled, a sparse, symmetric system is obtained, which is solved by the BiConjugate Gradient Stabilized (Bi-CGSTAB) iterative method. Once the streamfunction and its derivatives are found, the motion of the nodes is computed using a low storage Runge-Kutta scheme. Viscous effects are accounted for by solving the Laplacian in the vorticity transport equation. The second-order derivatives of the vorticity are found by solving a least-squares fit about each node. Finally, to overcome the loss of accuracy due to Lagrangian distortion, the computational domain is periodically retriangulated every few time steps.

As with any newly developed scientific software, the current code was validated through different tests. Its implementation was checked via the Method of Manufactured Solutions, which proved that the numerical solution converged with the refinement of the grid, and generated outputs that matched the theoretical values, confirming the validity of the code. Then comparison tests between theoretical and computed values for two fundamental problems in fluid dynamics, potential flow over a circular cylinder and an ellipse, were performed. In the cylinder case, the maximum error between the computed and theoretical velocities was 0.65%, an extra proof on the accuracy of the numerical method. For the ellipse problem, various simulations are run for different aspect ratios. It was observed that the maximum error between the computed and theoretical velocities increases with the thickness of the body from 1% to

6.8%, while the maximum error between the theoretical and computed streamfunctions stays nearly constant at around 3.5% for all aspect ratios investigated. These findings assert the accuracy of the developed model.

Moreover, the performance of the code was assessed for viscous flows by simulating the development of an isolated Lamb-Oseen vortex, wing tip vortices with and without the presence of the ground and the evolution of a four-vortex wake system. In the first case, the evolution and decay of the isolated Lamb-Oseen vortex matched well the theoretical values, and the error between the maximum computed vorticity and maximum theoretical one decreased with the refinement of the grid. In all other problems, the simulation results were in good agreement with results of previous studies on the subjects. The performed tests proved the robustness and reliability of the numerical method presented in this thesis.

The computational scheme has been used to predict the evolution of perturbed Lamb-Oseen vortices. Different distortions were applied with various amplitudes at different Reynolds number. In the case of a quadrupolar perturbation, the base vortex decayed either to an axisymmetric monopole or to a quasi-steady rotating tripole. The simulations showed that for every Reynolds number there exists a critical amplitude that separates both states, and when Re increases the threshold value decreases. These results agree well with previous studies on the subject. The tripole is a coherent structure as it was found, once formed, to be stable and to decay due to viscosity. An initially large quadrupolar perturbation broke the Lamb-Oseen vortex into two cores, which formed two dipoles travelling in opposite directions. But since the outer boundary of the computational domain was modelled as a solid wall, the dipoles could not keep moving radially outwards, so they travelled back to the centre of the domain where the positive vortices met and merged, forming anew a tripolar structure.

Perturbing the Lamb-Oseen vortex by a hexapolar distortion can lead to the evolution of a triangular vortex if the perturbation amplitude is higher than the threshold value. Otherwise, the vortex decays back to its original axisymmetric state. Unlike the tripole, the triangle does not retain its shape and decays merely due to viscous effects, but experiences vortex merging that turns it into a tripole. This fact might explain why a tripole has not been observed yet in real life. A stability study showed that this process is triggered by the unequal strengths of the satellites. Increasing the perturbation amplitude was found to affect the stability of the structure and to delay vortex merging. Therefore, the triangle was considered a coherent structure since it can be stable and live for many turnover times before breaking down, if its satellites are strong enough. However, it is the weakest member of this family. When a large hexapolar perturbation amplitude was applied to the Lamb-Oseen vortex, an unstable triangle formed, which broke into three dipoles travelling radially outwards and a central core relaxing to axisymmetry.

In a third case, the Lamb-Oseen vortex was perturbed by an 8-pole distortion, and observed to evolve into three different states, depending on the perturbation amplitude. For very small distortions, the vortex assumed axisymmetry. For moderate perturbations less than the threshold value, the initial structure decayed to a tripole. Finally, for perturbations higher than the threshold value, an unstable square vortex formed, which

was short lived and evolved into a tripole through vortex merging. A perturbation amplitude that leads to a stable square could not be found, as a result, the vortex was not considered a coherent structure. Similar to the triangle, it was found that the vortex merging mechanism in the square is triggered by the unequal strengths of its satellites. If after merging, the resultant vortices are stronger than the core, they break it in half, forming two dipoles that travel in opposite directions.

The evolution of Lamb-Oseen vortices when perturbed by different distortions is summarised in Figure 8.1.

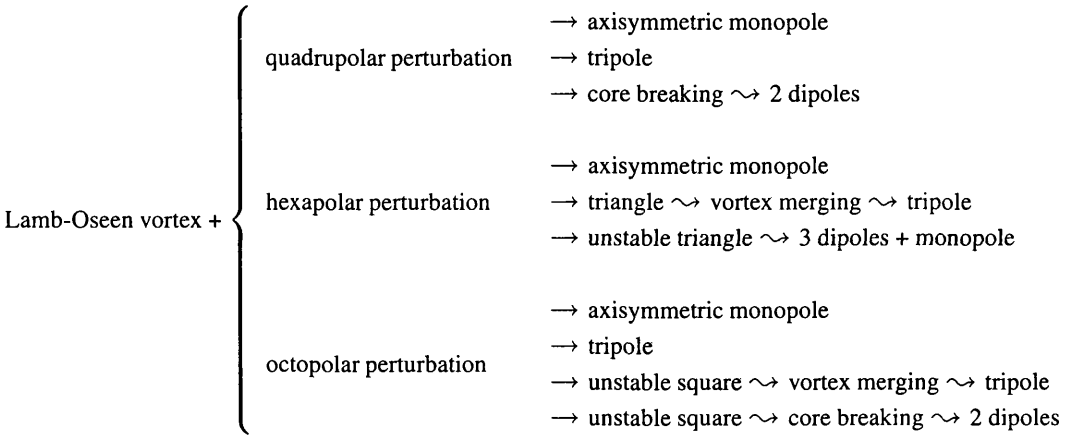

Figure 8.1: Summary of the evolution of Lamb-Oseen vortices under different perturbations.

Further projects can be undertaken following in the footsteps of the work presented in this thesis. First of all, an interesting development of the numerical method would be its extension to three-dimensions. To achieve this task, the vector potential has to be solved for instead of the streamfunction. Once extended to 3-D, the model can be widely used by the scientific community to study various aspect of real life flows. Second, the dependence of the results on the triangulation is a field that needs further investigations in order to find the optimum criteria for the initial discretisation and remeshing of the domain. As explained in §7.1, a new algorithm that controls the time step Δt can be introduced to the current model in order to stabilise the simulation by not allowing an edge length to become smaller than the characteristic length scale.

Moreover, the numerical method has several applications. Beside simulating plane flows, it can be used for the study of axisymmetric flows. In such case, the approximation of the streamfunction by the truncated Taylor series remain unchanged, but the Poisson equation (5.3) becomes Equation (2.17). This requires changing the differential operator for the streamfunction from $\mathrm{D}_i = [0\ 0\ 0\ 1\ 0\ 1]$, Equation (5.5c), to $\mathrm{D}_i = [-1/r\ 0\ 0\ 1\ 0\ 1]$. Moreover, when applying a velocity boundary condition Equations (2.6a) and (2.6b) have to be considered instead of Equations (2.5a) and (2.5b). Once the system of equations is solved, the viscous diffusion is computed and

the nodes are moved as explained in §5.6 and §5.5.

The current code can also be applied to simulate viscous flows around bodies and investigate the wake development. In such problems, viscous diffusion from solid boundaries has to be taken into account. In classical vortex methods extra numerical algorithms are added to perform these calculations. Usually, the panel method is used, where a vortex sheet is first generated on the body surface, then a numerical scheme is used to transform the viscous diffusion into the flow. However, in the current method the viscous diffusion from solid boundaries is computed directly as explained in §5.6 without a need for further schemes.

Another area worth investigating, would be the development of wing tip vortices in presence of ground with a boundary layer. In the current study, the ground was considered to have slip conditions. However, to simulate a real life problem, a no slip boundary condition has to be introduced, which will lead to the development of secondary vortices once the tail vortices hit the ground and bounce upward. Understanding the evolution of vorticity in this case is of special interest, especially for air traffic control and airports operators.

On the subject of vortex instability, the effect of Reynolds number on the formation and evolution of triangular and square vortices could be investigated. Moreover, the behaviour of Lamb-Oseen vortices when subjected to high-order perturbations, such as 10-pole or 12-pole, might be an interesting subject to study. Understanding the development and evolution of high order vortices might be a step towards a better understanding of atmospheric and oceanic flows.

Epilogue

Almustafa, the chosen and the beloved, who was a dawn onto his own day, had waited twelve years in the city of Orphalese for his ship that was to return and bear him back to the isle of his birth. And in the twelfth year, on the seventh day of Ielool, the month of reaping, he climbed the hill without the city walls and looked seaward; and he beheld the ship coming with the mist. Then the gates of his heart were flung open, and his joy flew far over the sea. And he closed his eyes and prayed in the silences of his soul. But he descended the hill, a sadness came upon him, and he thought in his heart:

How shall I go in peace and without sorrow? Nay, not without a wound in the spirit shall I leave this city.

Long were the days of pain I have spent within its walls, and long were the nights of aloneness; and who can depart from his pain and his aloneness without regret?

Too many fragments of the spirit have I scattered in these streets, and too many are the children of my longing that walk naked among these hills, and I cannot withdraw from them without a burden and an ache.

It is not a garment I cast off this day, but a skin that I tear with my own hands.

Nor is it a thought I leave behind me, but a heart made sweet with hunger and with thirst.

Yet I cannot tarry longer.

The sea that calls all things unto her calls me, and I must embark. For to stay, though the hours burn in the night, is to freeze and crystallize and be bound in a mould.

Fain would I take with me all that is here. But how shall I? A voice cannot carry the tongue and the lips that give it wings. Alone must it seek the ether. And alone and without his nest shall the eagle fly across the sun.

Now when he reached the foot of the hill, he turned again towards the sea, and he saw his ship approaching the harbour, and upon her prow the mariners, the men of his own land. And his soul cried out to them, and he said:

Sons of my ancient mother, you riders of the tides, How often have you sailed in my dreams. And now you come in my awakening, which is my deeper dream. Ready am I to go, and my eagerness with sails full set awaits the wind. Only another breath will I breathe in this still air, only another loving look cast backward, Then I shall stand among you, a seafarer among seafarers. And you, vast sea, sleepless mother, who alone are peace and freedom to the river and the stream, only another winding will this stream make, only another murmur in this glade, and then shall I come to you, a boundless drop to a boundless ocean.

These things he said in words. But much in his heart remained unsaid. For he himself could not speak his deeper secret.

The Prophet, Khalil Gibran, 1923

References

[1] T. L. Heath, editor. *The Works of Archimedes*. Dover Publications, Inc., New York, USA, 2002.

[2] F. Zöllner and N. Johannes, editors. *Leonardo da Vinci: The Complete Paintings and Drawings*. Taschen, Cologne, Germany, 2003.

[3] M. Bywater. Decoding da Vinci. *New Statesman*, 18 September 2006.

[4] L. D. Landau and E. M. Lifshitz. *Fluid Mechanics*. Butterworth-Heinemann, Oxford, UK, 2nd edition, 1987. Translated from the Russian by J. B. Sykes and W. H. Reid.

[5] Clay Mathematics Institute. Millennium problems. http://www.claymath.org/millennium/, last access on 4 April 2007.

[6] H. Helmholtz. On integrals of the hydrodynamical equations which express vortex motion. *Philosophical Magazine*, 33(4):485–512, 1867. Translated by P. G. Tait.

[7] L. Kelvin. On vortex motion. *Transactions of the Royal Society of Edinburgh*, 25:217–260, 1868.

[8] L. Prandtl. Über flüssigkeitbewegung bei sehr kleiner Reibung. In *Proceedings of the Fourth Mathematics Congress*, pages 484–491, Heidelberg, 1904. English translation in *Early developments of modern aerodynamics*, J. A. D. Ackroyd, B. P. Axcell and A. I. Ruban, Butterworth-Heinemann, 2002, pages 77.

[9] J. D. Anderson. Ludwig Prandtl's boundary layer. *Physics Today*, 58(12):42–48, 2005.

[10] L. Prandtl. Turbulent flow. Technical Report TM–435, NACA, 1927. Originally delivered to the 2nd International Congress for Applied Mechanics. Zurich, 1926.

[11] J. C. McWilliams. The emergence of isolated coherent vortices in turbulent flow. *Journal of Fluid Mechanics*, 146:21–43, 1984.

[12] V. Venkatakrishnan. A perspective on unstructured grid flow solvers. Technical Report 95-3, NASA Langley Research Center, 1995.

[13] K. Morgan and J. Peraire. Unstructured grid finite element methods for fluid mechanics. *Inst. Phys. Rev.*, 61(6):569–638, 1998.

[14] G. Russo and J. A. Strain. Fast triangulated vortex methods for the 2D Euler equations. *Journal of Computational Physics*, 111:291–323, 1994.

[15] S. A. Huyer and J. A. Grant. Solution of two-dimensional vorticity equation on a Lagrangian mesh. *AIAA Journal*, 38(5):774–783, 2000.

[16] J. S. Marshall, J. R. Grant, A. A. Gossler, and S. A. Huyer. Vorticity transport on a Lagrangian tetrahedral mesh. *Journal of Computational Physics*, 161:85–113, 2000.

[17] M. Carley. A triangulated vortex method for the axisymmetric Euler equations. *Journal of Computational Physics*, 180:616–641, 2002.

[18] D. J. Tritton. *Physical fluid dynamics*. Oxford University Press, Oxford, UK, 2nd edition, 1988.

[19] P. G. Saffman. *Vortex dynamics*. Cambridge University Press, 1992.

[20] J. D. Anderson. *Fundamentals of aerodynamics*. McGraw-Hill, New York, 3rd edition, 2001.

[21] N. Rott. Note on the history of the Reynolds number. *Annual Review of Fluid Mechanics*, 22:1–11, 1990.

[22] V. N. Vatsa, M. D. Saxetrik, and E. B. Parlette. Development of a flexible and efficient multigrid-based multi-block flow solver. In *AIAA Conference*. AIAA paper 93-0677, 1993.

[23] W. K. Anderson. Grid generation and flow solution method for Euler equations on unstructured grids. Technical Memorandum 4295, NASA Langley Research Center, 1992.

[24] W. K. Anderson and D. L. Bonhaus. An implicit upwind algorithm for computing turbulent flows on unstructured grids. *Computers and Fluids*, 23(1):1–21, 1994.

[25] W. K. Anderson and D. L. Bonhaus. Aerodynamic design on unstructured grids for turbulent flows. Technical Memorandum 112867, NASA Langley Research Center, 1997.

[26] B. Delaunay. Sur la sphère vide. *Bulletin de l'Académie des Sciences de l'USSR*, 7:793–800, 1934.

[27] L. F. Richardson. *Weather Prediction by Numerical Process*. Cambridge University Press, 1922.

[28] L. Rosenhead. The formation of vortices from a surface of discontinuity. *Proceedings of the Royal Society of London. A.*, 134:170–192, 1932.

[29] A. Leonard. Vortex methods for flow simulation. *Journal of Computational Physics*, 37:289–335, 1980.

[30] A. Leonard. Computing three-dimensional incompressible flows with vortex elements. *Annual Review of Fluid Mechanics*, 17:523–559, 1985.

[31] T. Sarpkaya. Computational methods with vortices — the 1988 Freeman scholar lecture. *ASME Journal of Fluids Engineering*, 111:5–52, 1989.

[32] G. H. Cottet and P. D. Koumoutsakos. *Vortex methods: Theory and Practice*. Cambridge University Press, 2000.

[33] M. J. Stock. Summary of vortex methods literature. http://mstock.personal.engin.umich.edu/research/vortex_methods_literature.pdf, May 2006.

[34] R. W. Barber and A. Fonty. Comparison of vortex-element and finite-volume simulations of low Reynolds number flow over a confined backward-facing step. In *CFD2003*, Vancouver, May 2003.

[35] A. J. Chorin. Numerical study of slightly viscous flow. *Journal of Fluid Mechanics*, 57(4):785–796, 1973.

[36] M. Perlman. On the accuracy of vortex methods. *Journal of Computational Physics*, 59:200–223, 1985.

[37] L. A. Barba, A. Leonard, and C. B. Allen. Advances in viscous vortex methods — meshless spatial adaption based on radial basis function interpolation. *International Journal for Numerical Methods in Fluids*, 47:387–421, 2005.

[38] O. H. Hald and V. M. Del Prete. Convergence of vortex methods for Euler's equations. *Mathematics of Computation*, 32:791–809, 1978.

[39] M. L. Ould-Salihi, G. H. Cottet, and M. El Hamraoui. Blending finite-difference and vortex methods for incompressible flow computations. *SIAM Journal on Scientific Computing*, 22:1655–1674, 2000.

[40] H. Chen and J. S. Marshall. A Lagrangian vorticity method for two-phase particulate flows with two-way phase coupling. *Journal of Computational Physics*, 148:169–198, 1999.

[41] J. S. Marshall and J. R. Grant. A Lagrangian vorticity collocation method for viscous, axisymmetric flows with and without swirl. *Journal of Computational Physics*, 138:302–330, 1997.

[42] K. Kuwahara and H. Takami. Numerical studies of two-dimensional vortex motion by a system of points. *Journal of the Physical Society of Japan*, 34:247–253, 1973.

[43] P. Degond and S. Mas-Gallic. The weighted particle method for convection-diffusion equations. Part 1. the case of an isotropic viscosity. *Mathematics of Computation*, 53:485–507, 1989.

[44] D. Fishelov. A new vortex scheme for viscous flow. *Journal of Computational Physics*, 86:211–224, 1990.

[45] P. Degond and F. J. Mustieles. A deterministic approximation of diffusion equations using particles. *SIAM Journal on Scientific and Statistical Computing*, 11:293–310, 1990.

[46] S. Shankar. *A new mesh-free vortex method.* PhD thesis, The Florida A&M University and The Florida State University, College of Engineering, Florida, USA, August 1996.

[47] S. Shankar and L. van Dommelen. A new diffusion procedure for vortex methods. *Journal of Computational Physics*, 127:88–109, 1996.

[48] L. Greengard and V. Rokhlin. A fast algorithm for particle simulation. *Journal of Computational Physics*, 73:325–348, 1987.

[49] J. Carrier, L. Greengard, and V. Rokhlin. A fast adaptive multipole algorithm for particle simulations. *SIAM Journal on Scientific and Statistical Computing*, 9(4):669–686, 1988.

[50] J. H. Strickland and D. E. Amos. Fast solver for systems of axisymmetric ring vortices. *AIAA Journal*, 30(3):737–748, 1992.

[51] J. Goodman. Convergence of the random vortex method. *Communications in Pure and Applied Mathematics*, 40:189–220, 1987.

[52] A. J. Chorin. Vortex models and boundary layer instability. *SIAM Journal on Scientific and Statistical Computing*, 1:1–21, 1980.

[53] C. Greengard. The core spreading vortex method approximates the wrong equation. *Journal of Computational Physics*, 61:345–348, 1985.

[54] L. F. Rossi. Resurrecting core spreading methods: A new scheme that is both deterministic and convergent. *SIAM Journal on Scientific Computing*, 17(2):370–397, 1996.

[55] P. D. Koumoutsakos and A. Leonard. High resolution simulations of the flow around an impulsively started cylinder using vortex methods. *Journal of Fluid Mechanics*, 296:1–38, 1995.

[56] Y. Ogami and T. Akamatsu. Viscous flow simulation using the discrete vortex model– the diffusion velocity model. *Computers and Fluids*, 19:433–441, 1991.

[57] Y. Ogami and A. Y. Cheer. Simulations of unsteady compressible fluid motion by an interactive cored particle method. *SIAM Journal on Applied Mathematics*, 55:1204–1226, 1995.

[58] N. R. Clarke and O. R. Tutty. Construction and validation of a discrete vortex method for the two-dimensional incompressible Navier-Stokes equations. *Computers and Fluids*, 23:751–783, 1994.

[59] T. Liszka and J. Orkisz. The finite difference method at arbitrary irregular grids and its application in applied mechanics. *Computers and Structures*, 11:83–95, 1980.

[60] G. Russo. A deterministic vortex method for the Navier-Stokes equations. *Journal of Computational Physics*, 108:84–94, 1993.

[61] J. C. McWilliams. Oceans, atmospheres, planets and stars. http://www.psc.edu/science/McWilliams/McWilliams.html, accessed on 21 May 2006.

[62] Y. Couder and C. Basdevant. Experimental and numerical study of vortex couples in two-dimensional flows. *Journal of Fluid Mechanics*, 173:225–251, 1986.

[63] BBC Weather Centre. The Gulf Stream. http://www.bbc.co.uk/climate/impact/gulf_stream.shtml, accessed on 2 February 2007.

[64] P. S. Marcus. Jupiter's Great Red Spot and other vortices. *Annual Review of Astronomy and Astrophysics*, 31:523–573, 1993.

[65] T. Phillips. Jupiter's new Red Spot. http://science.nasa.gov/headlines/y2006/02mar_redjr.htm, accessed on 3 March 2006.

[66] J. Toomre and N. H. Brummell. Solar convection zone dynamics and rotation. In J. T. Hoeksema, V. Domingo, B. Fleck, and B. Battrick, editors, *ESA SP-376: Helioseismology*, Paris, 1995. European Space Agency.

[67] J. Vranjes. Tripolar vortex in plasma flow. *Planetary and Space Science*, 47:1531–1535, 1999.

[68] Hubblesite. Jupiter's New Red Spot – HST ACS/WFC: April 16, 2006. http://hubblesite.org/newscenter/archive/releases/2006/19/image/c/, accessed on 9 September 2006.

[69] L. M. Polvani and X. J. Carton. The tripole: A new coherent vortex structure of incompressible two-dimensional flows. *Geophysical and Astrophysical Fluid Dynamics*, 51:87–102, 1990.

[70] O. U. Velasco Fuentes. Evolution of a Lamb quadrupolar vortex. *Fluid Dynamics Research*, 26:13–33, 2000.

[71] M. V. Melander, J. C. McWilliams, and N. J. Zabusky. Axisymmetrization and vorticity-gradient intensification of an isolated two-dimensional vortex through filamentation. *Journal of Fluid Mechanics*, 178:137–159, 1987.

[72] V. D. Larichev and G. M. Reznik. On collisions between two-dimensional solitary Rossby waves. *Oceanology*, 23:545–552, 1983.

[73] C. G. Rossby. Relation between variations in the intensity of the zonal circulation of the atmosphere and the displacements of the semi-permanent centers of actions. *Journal of Marine Research*, 2:38–55, 1939.

[74] C. E. Leith. Minimum enstrophy vortices. *Physics of Fluids*, 27(6):1388–1395, 1984.

[75] G. R. Flierl. On the instability of geostrophic vortices. *Journal of Fluid Mechanics*, 197:349–388, 1988.

[76] Delft University of Technology. Current velocities of the Gulf Stream. http://rads.tudelft.nl/gulfstream/, accessed on 8 February 2007.

[77] R. Benzi, S. Patarnello, and P. Santangelo. On the statistical properties of two-dimensional decaying turbulence. *Europhysics Letters*, 3:811–818, 1987.

[78] B. Legras, P. Santangelo, and R. Benzi. High-resolution numerical experiments for forced two-dimensional turbulence. *Europhysics Letters*, 5(1):37–42, 1988.

[79] G. J. F. van Heijst and R. C. Kloosterziel. Tripolar vortices in a rotating fluid. *Nature*, 338:569–571, 1989.

[80] R. D. Pingree and B. Le Cann. Anticyclonic eddy in the Southern Bay of Biscay. *Journal of Geophysical Research*, 97:14353–14367, 1992.

[81] Fluid Dynamics Laboratory of Eindhoven University of Technology. A tripolar vortex in the ocean. http://www.fluid.tue.nl/WDY/vort/intro/seatrip.html, last access on 7 December 2006.

[82] X. J. Carton, G. R. Flierl, and L. M. Polvani. The generation of tripoles from unstable axisymmetric isolated vortex structures. *Europhysics Letters*, 9:339–344, 1989.

[83] G. J. F. van Heijst, R. C. Kloosterziel, and C. W. M. Williams. Laboratory experiments on the tripolar vortex in a rotating fluid. *Journal of Fluid Mechanics*, 225:301–331, 1991.

[84] R. C. Kloosterziel and G. J. F. van Heijst. An experimental study of unstable barotropic vortices in a rotating fluid. *Journal of Fluid Mechanics*, 223:1–24, 1991.

[85] P. Orlandi and G. F. Carnevale. Evolution of isolated vortices in a rotating fluid of finite depth. *Journal of Fluid Mechanics*, 381:239–269, 1999.

[86] P. Orlandi and G. J. F. van Heijst. Numerical simulation of tripolar vortices in 2D flow. *Fluid Dynamics Research*, 9:179–206, 1992.

[87] J. R. Holton. *An introduction to dynamic meteorology*. Academic Press Limited, London, UK, 3rd edition, 1992.

[88] X. J. Carton and B. Legras. The life-cycle of tripoles in two-dimensional incompressible flows. *Journal of Fluid Mechanics*, 267:53–82, 1994.

[89] X. J. Carton. On the merger of shielded vortices. *Europhysics Letters*, 18(8):697–703, 1992.

[90] J. B. Flor, W. S. S. Govers, G. J. F. van Heijst, and R. van Sluis. Formation of a tripolar vortex in a stratified fluid. *Applied Scientific Research*, 51:405–409, 1993.

[91] J. B. Flor and G. J. F. van Heijst. Stable and unstable monopolar vortices in a stratified fluid. *Journal of Fluid Mechanics*, 311:257–287, 1996.

[92] J. S. Hesthaven, J. P. Lynov, J. J. Rasmussen, and G. G. Sutyrin. Generation of tripolar vortical structures on the beta plane. *Physics of Fluids*, 5(7):1674–1678, 1993.

[93] O. U. Velasco Fuentes, G. J. F. van Heijst, and N. P. M. van Lipzig. Unsteady behaviour of a topography-modulated tripole. *Journal of Fluid Mechanics*, 307:11–41, 1996.

[94] L. F. Rossi, J. F. Lingevitch, and A. J. Bernoff. Quasi-steady monopole and tripole attractors for relaxing vortices. *Physics of Fluids*, 9(8):2329–2338, 1997.

[95] S. Le Dizès. Non-axisymmetric vortices in two-dimensional flows. *Journal of Fluid Mechanics*, 406:175–198, 2000.

[96] L. A. Barba and A. Leonard. Emergence and evolution of tripole vortices from net-circulation initial conditions. *Physics of Fluids*, 19(017101):1–16, 2007.

[97] R. W. Griffiths and P. F. Linden. The stability of vortices in a rotating, stratified fluid. *Journal of Fluid Mechanics*, 105:283–316, 1981.

[98] R. Verzicco, F. Lalli, and E. Campana. Dynamics of baroclinic vortices in a rotating, stratified fluid: A numerical study. *Physics of Fluids*, 9(2):419–432, 1997.

[99] G. F. Carnevale and R. C. Kloosterziel. Emergence and evolution of triangular vortices. *Journal of Fluid Mechanics*, 259:305–331, 1994.

[100] M. Beckers and G. J. F. van Heijst. The observation of a triangular vortex in a rotating fluid. *Fluid Dynamics Research*, 22:265–279, 1998.

[101] Y. G. Morel and X. J. Carton. Multipolar vortices in two-dimensional incompressible flows. *Journal of Fluid Mechanics*, 267:23–51, 1994.

[102] Fluid Dynamics Laboratory of Eindhoven University of Technology. Vortex instabilities in a stratified fluid. http://www.fluid.tue.nl/WDY/vort/instab/strat/strat.html, last access 7 September 2006.

[103] S. J. Lin. Contour dynamics of tornado-like vortices. *Journal of the Atmospheric Sciences*, 49(18):1745–1756, 1992.

[104] L. A. Barba. Nonshielded multipolar vortices at high Reynolds number. *Physical Review E*, 73(6):065303(R), 2006.

[105] J. H. Strickland. Gridless compressible flow: a white paper. Technical Report SAND2001-0527, Sandia National Laboratories, February 2001.

[106] R. Barrett, M. Berry, T. F. Chan, J. Demmel, J. Donato, J. Dongarra, V. Eijkhout, R. Pozo, C. Romine, and H. Van der Vost. *Templates for the solution of linear systems: Building blocks for iterative methods*. SIAM, Philadelphia, PA, 1994.

[107] S. Popinet. GTS: GNU Triangulated Surface Library. http://gts.sourceforge.net/, accessed between 2003-2007.

[108] R. S. Baty and W. P. Wolfe. Least-squares solutions of a general numerical method for arbitrary irregular grids. *International Journal for Numerical Methods in Engineering*, 40:1701–1717, 1997.

[109] P. S. Jensen. Finite difference techniques for variable grids. *Computers and Structures*, 2:17–29, 1972.

[110] N. Perrone and R. Kao. A general finite difference method for arbitrary meshes. *Computers and Structures*, 5:45–58, 1975.

[111] J. H. Williamson. Low-storage Runge-Kutta schemes. *Journal of Computational Physics*, 35:48–56, 1980.

[112] P. J. Roache. Code verification by the method of manufactured solutions. *ASME Journal of Fluids Engineering*, 124(1):4–10, March 2002.

[113] G. Polya. *How to solve it: A new aspect of mathematical method.* Princeton University Press, Princeton, NJ, 1957.

[114] L. Milne-Thomson. *Theoretical hydrodynamics.* Macmillan, London, 5th edition, 1968.

[115] M. J. Lighthill. *Higher approximations in aerodynamic theory.* Princeton University Press, Princeton, New Jersey, 1960.

[116] J. Wang and D. D. Joseph. Potential flow of a second-order fluid over a sphere or an ellipse. *Journal of Fluid Mechanics*, 511:201–215, 2004.

[117] H. Lamb. *Hydrodynamics.* Cambridge University Press, 6th edition, 1932.

[118] L. Turk, D. Coors, and D. Jacob. Behaviour of wake vortices near the ground over a large range of Reynolds numbers. *Aerospace Science and Technology*, 2:71–81, 1999.

[119] S. J. Barker and S. C. crow. The motion of two-dimensional vortex pairs in a ground effect. *Journal of Fluid Mechanics*, 82:659–671, 1977.

[120] W. J. Devenport, J. S. Zsoldos, and C. M. Vogel. The structure and development of a counter-rotating wing-tip pair. *Journal of Fluid Mechanics*, 332:71–104, 1997.

[121] P. R. Spalart. Airplane trailing vortices. *Annual Review of Fluid Mechanics*, 30:107–138, 1998.

[122] D. Fabre and J. Jacquin. Stability of a four-vortex aircraft wake model. *Physics of Fluids*, 12(10):2483–2443, 2000.

[123] S. C. Rennich and S. K. Lele. A method for accelerating the destruction of aircraft wake vortices. *Journal of Aircraft*, 36(2):398–404, 1999.

[124] D. Fabre, L. Jacquin, and A. Loof. Optimal perturbations in a four-vortex aircraft wake in counter-rotating configuration. *Journal of Fluid Mechanics*, 451:319–328, 2002.

[125] R. L. Bristol, J. M. Ortega, P. S. Marcus, and Ö. Savas. On cooperative instabilities of parallel vortex pairs. *Journal of Fluid Mechanics*, 517:331–358, 2004.

[126] Hydraulic institute University of Genoa. Gallery. http://www.diam.unige.it/ irro/gallery.html, last access on 15 February 2007.

[127] J. C. Hardin and F. Y. Wang. Sound generation by aircraft wake vortices. Technical Report NASA/CR-2003-212674, NASA, Langley Research Center, Hampton, Virginia, 2003.

[128] T. S. Lundgren. Strained spiral vortex model for turbulent fine structure. *Physics of Fluids*, 25:2193–2203, 1982.

[129] L. F. Rossi. Merging computational elements in vortex simulations. *SIAM Journal on Scientific Computing*, 18(4):1014–1027, 1997.